

**Metal Abundances of the Absorber-Systems
toward HS1700+6416**

2. Juni 1997
Diplomarbeit

Angefertigt von Ulrich Sperhake

im Fachbereich Physik der Universität Hamburg
unter der Anleitung von Prof. Dr. Reimers
an der Hamburger Sternwarte Bergedorf

Abstract

New UV spectra of the bright ($V = 16.1$), high redshift ($z_{em} = 2.72$) quasar HS1700+6416 with improved $S/N = 10.20$ covering most of the range between 1150 Å and 2330 Å are presented. In the light of recently published, high resolution optical data they are analysed with particular regard to neon and sulphur abundances as well as absorption systems at lower redshifts.

The data suggest the existence of a new metal line system at $z \approx 0.09$. Absorption systems at $z = 2.37995, 2.7125$ and 2.7444 identified in optical data are investigated in UV spectra reaching down to 1150 Å for the first time.

Observed column densities for a wide variety of ions provide useful constraints for cloud models with two regions of different hydrogen density calculated for 6 absorption systems at $z \leq 2.168$ in order to derive metal abundances for oxygen, carbon, nitrogen, silicon, sulphur, neon and magnesium. The cloud models are assumed to be photoionized by metagalactic radiation fields computed by Haardt & Madau (1996) for different redshifts. Discrepancies between predicted and measured column densities for high ionization species (O VI, Ne VII, Ne VIII) observed at higher redshift can be overcome by the application of a harder ionizing field. High column densities of O II and C II observed for the absorber at $z = 0.722$ require a softer radiation field with an increased edge at the Lyman limit. These modifications, though, lead to only slightly different heavy element abundances.

In the face of a high metallicity of the absorber complex at $z = 2.315$ derived from optical data by Tripp et al. (1997), their model has been checked for consistency with results from the new UV data and is found to produce insufficient amounts of higher ionization species.

Contents

1	Introduction	2
2	Observations	3
2.1	Observational Parameters	3
2.2	Data Preparation	4
2.3	Combination with older GHRM Data	6
3	Continuum Definition	6
4	Line Identification	8
4.1	Interstellar Absorption Lines	9
4.2	Extragalactic Absorption Systems	10
5	Column Densities	20
5.1	Error Sources	21
5.2	Analysis Techniques	22
5.3	Results	24
6	Ionization Models	25
6.1	Results for individual Absorber Systems	26
6.1.1	$z = 2.168$	26
6.1.2	$z = 1.8451$	30
6.1.3	$z = 1.1574$	31
6.1.4	$z = 0.8643$	33
6.1.5	$z = 0.722$	35
6.1.6	$z = 0.5524$	36
6.2	Modifications of the Models	38
6.2.1	$z = 1.8451$	38
6.2.2	$z = 0.722$	40
6.3	The Absorber Complex at $z = 2.315$	42
6.4	Results	44
7	Conclusions	46
8	References	48
A	Atomic Parameters	50
B	Line Identifications	54
C	Column Densities	68
D	Calculated Spectrum	72

Metal Abundances of the Absorber-Systems toward HS1700+6416

1 Introduction

With the detection of absorption lines in the spectra of high-redshift quasars a unique opportunity has arisen to study the physical and chemical properties of regions of the universe otherwise not accessible for astrophysical observations. QSO absorption lines thus provide an important gateway to infer observational constraints on galaxy formation and evolution and to probe conditions in the early universe.

Different types of absorbers give rise to these absorption lines. Whereas the majority of Ly α and higher series lines are produced in Ly α clouds until recently believed to be generally metal deficient, metal line systems (hereafter MLS) also reveal absorption caused by heavier elements. Yet, after the detection of metal absorption lines associated with $\approx 75\%$ of the Ly α absorbers of H I column-densities as low as $3 \cdot 10^{14} \text{ cm}^{-2}$ (Songaila and Cowie 1996), the distinction between these absorber types has become somewhat unclear. Due to sufficiently high neutral hydrogen column densities, so called Lyman limit systems (LLS) are optically thick for Lyman continuum photons ($\lambda < 912 \text{ \AA}$ in the absorber restframe) and produce sharp edges in the quasar spectra, sometimes even completely absorbing the quasar flux below $912 \text{ \AA} \cdot (1+z_{\text{LLS}})$.

Since the majority of strong heavy element lines falls into the ultraviolet frequency range, even if originating at redshifts ≈ 2 , the successful implementation of the Hubble Space Telescope (HST) has provided a substantial breakthrough in the studies of QSO absorption lines. Yet, due to the LLS, mentioned above, only a few quasars are known to exhibit detectable flux over a wide range of the UV part of the electromagnetic spectrum. As shown by IUE observations between 1200 \AA and 3200 \AA the bright ($V = 16.1$) high-redshift ($z = 2.72$) quasar HS1700+6416 discovered in the course of the Hamburg Quasar Survey (Reimers et al. 1989), belongs to this class. Reimers et al. (1992) presented an extraordinary spectrum, taken by the HST Faint Object Spectrograph (FOS), which reveals the existence of 7 LLS. Following further investigation of the FOS data and complementary optical data, Vogel & Reimers (1995) (hereafter VR 95) reported the discovery of 8 additional MLS and provided constraints on the metal abundances and the photoionizing radiation fields for several of these systems.

Observations obtained with the Goddard High Resolution Spectrograph (GHRS) provided improved signal to noise and resolution in the spectral range between 1100 \AA and 1600 \AA (Köhler, Reimers and Wamsteker 1996, hereafter KRW 96). They detect absorption by Ne III-Ne VII and S III-S V and compute metal abundances for MLS/LLS at $z \approx 1$ and $z \approx 2$, assuming cloud models with two regions of different density ionized by a metagalactic radiation field. Yet their data still suffer from poor signal to noise ($S/N < 8$ for the original and $S/N < 15$ for gauss filtered data) which seriously affects the precision of their results. Therefore new spectra of moderately improved S/N covering most parts of the range between 1150 \AA and 2330 \AA have been taken with the FOS and GHRS onboard the Hubble Space Telescope. In connection with optical data presented by Tripp et al. (1997), Petitjean et al. (1996) and Rodríguez-Pascual et al. (1995) (hereafter TLS 97, PRR 96 and R-P 95 respectively), these new spectra are analysed in order to derive more accurate metal abundances with particular regard to Neon and Sulphur, and to gain further information about the ionizing radiation field and physical properties of the absorbing clouds.

2 Observations

2.1 Observational Parameters

The observations were carried out with the Faint Object Spectrograph and the Goddard High Resolution Spectrograph onboard the Hubble Space Telescope on May 28th-30th 1996. The FOS data were obtained through the 4.3 aperture ($3.66'' \times 3.71''$), using the BLUE digicon detector in combination with the G190H grating. Following VR 95, the instrumental spectroscopic spread function (SSF) is approximated by a gaussian curve with $\text{FWHM} = 1.44 \text{ \AA}$ corresponding to 185–275 km/s. The GHRS data were taken

Table 1: Observational parameters of FOS and GHRS spectra

	FOS	GHRS
Detector/Grating	Blue G190H	G140L
Exposure Time [s]	24900	35904
Date of Observation	May 28th, 29th 1996	May 29th, 30th 1996
Wavelength Range	1570..2330 \AA	1150..1450 \AA
Dispersion $\text{\AA}/\text{Pixel}$	0.367	0.15
Resolution FWHM [\AA]	1.44	0.77
S/N	10..20	≤ 13

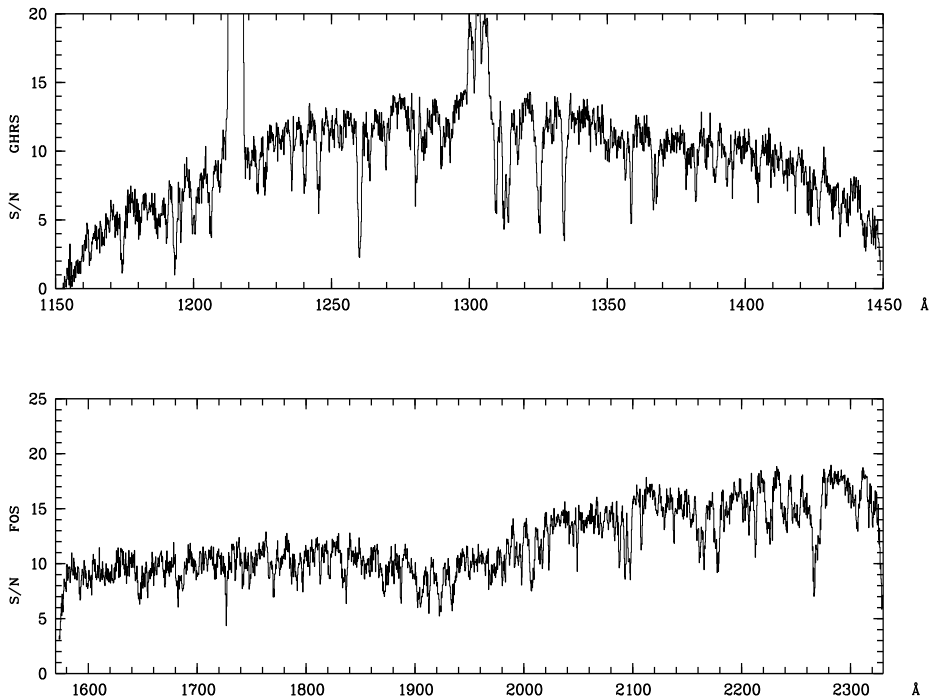


Figure 1: Signal to noise of the HST data

through the Large Science Aperture (LSA) with a square opening of $1.74'' \times 1.74''$. The SSF is represented by a gaussian of $\text{FWHM} = 0.77 \text{ \AA}$ (cf., Leitherer & Kinney 1994) corresponding to 159–201 km/s. The observational parameters are summarized in detail in Table 1. Due to the wavelength dependency of the sensitivity of both the G190H and the G140L grating, the signal to noise varies considerably over the observed range (see Figure 1).

2.2 Data Preparation

The spectra were supplied in the form of wavelength-, flux- and 1σ error-arrays. But whereas the FOS spectrum contained an integrated flux and propagated error-array, the GHRs data consisted of 120 individual exposures taken over 32 slightly different wavelength grids. Neglecting wavelength ranges contaminated by geocoronal Ly α and O I emission, which originate in the earth’s atmosphere, the average flux of the individual exposures has been calculated. In the context of discrepancies of $\geq 30 \%$ in the continuum level between older IUE/FOS and GHRs data of HS1700 reported by KRW 96, it is worth noticing that this average flux varied between $0.46 \cdot 10^{-15}$ and $2.04 \cdot 10^{-15} \text{ erg}/(\text{s} \cdot \text{cm}^2 \cdot \text{\AA})$, excluding one exposure with negative mean flux, during which the target was lost. Yet no systematic evolution of the mean flux in the course of the observation time can be detected (see Figure 2). Reexamination of the GHRs data of KRW 96 revealed a similar behaviour. The most plausible explanation seems to be the varying position of the target with respect to the center of the aperture. Since similar problems might arise for the FOS data, the observed discrepancies of the total flux can be explained without assuming intrinsic variation of the quasar luminosity itself.

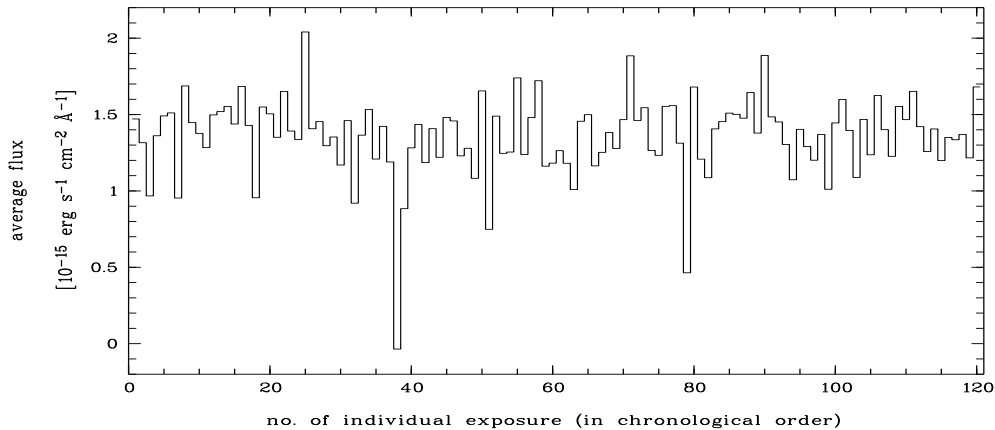


Figure 2: Average flux of the individual exposures

To carry out the GHRs data coaddition, the individual spectra had to be corrected for a potential offset in wavelength and rebinned to a common wavelength grid. The offset correction was performed by computing the correlation integral

$$I[a] = \int f(\lambda)g(\lambda - a)d\lambda$$

where g represents the individual spectrum in question and f is some reference, arbitrarily chosen to be the first one (absolute wavelength calibration is carried out later; see §4.1). $I[a]$ closely resembles the convolution $f * g[a] = \int f(\lambda)g(a - \lambda)dx$ and is therefore computed in Fourier space :

$$\begin{aligned}
I &= f(x) * g(-x) \\
\Rightarrow \mathcal{F}[I] &= \mathcal{F}[f(x) * g(-x)] \\
\Rightarrow \mathcal{F}[I] &= \mathcal{F}[f(x)] \cdot \mathcal{F}[g(-x)] \\
\Rightarrow \mathcal{F}[I] &= \mathcal{F}[f(x)] \cdot \bar{\mathcal{F}}[g(x)] \\
\Rightarrow I &= \mathcal{F}^{-1}[\mathcal{F}[f] \cdot \bar{\mathcal{F}}[g]]
\end{aligned}$$

where $\mathcal{F}[f]$ is the Fourier transform of the function f , $\mathcal{F}^{-1}[f]$ the inverse Fourier transform and \bar{x} denotes the complex conjugate of x . The third conclusion is only valid if g is a real function, which of course is always satisfied in the case of electromagnetic spectra. The value a , at which I reaches its maximum, is the best approximation to the offset of g with respect to f .

In order to smooth the data as little as possible, the rebinning was done by spline interpolating the original spectra. The determination of appropriate weighting factors for the combination of individual spectra is based on the assumption, that the flux values measured at one particular wavelength obey poisson statistics with similar expectation values. This requirement is not strictly satisfied because of possible misplacement of the target with respect to the aperture (see above). But, since, according to the HST Data Handbook, the initial error in the data is assumed to be Poisson limited, it still provides an easy way to obtain estimates for the weighting factors. Applying the Maximum-Likelihood-Method, the general argument starts with N measured values x_i of a quantity obeying a probability distribution $P(x; m)$ characterized by an unknown parameter m . The aim is to find the best estimate of m , i.e. the m that maximizes the probability

$$L(m) = P(x_1; m) \cdot P(x_2; m) \cdot \dots \cdot P(x_n; m) = \prod_{i=1}^n P(x_i; m)$$

Adopting poisson statistics, we have

$$\begin{aligned}
P(x; m) &= \frac{m^x \cdot e^{-m}}{x!} \\
L(m) &= \prod_{i=1}^n \frac{m^{x_i} \cdot e^{-m}}{x_i!}
\end{aligned}$$

Of course $L(m)$ reaches its maximum at the same m as $l(m)$ defined as

$$\begin{aligned}
l(m) &= \ln L(m) \\
&= \sum_{i=1}^n \ln \frac{m^{x_i} \cdot e^{-m}}{x_i!} \\
&= \sum_{i=1}^n (x_i \ln m - m) + const
\end{aligned}$$

m is given by the equation

$$\frac{dl}{dm} = 0$$

$$\begin{aligned} \Rightarrow \sum_{i=1}^n \left(\frac{x_i}{m} - 1 \right) &= 0 \\ \Rightarrow \sum_{i=1}^n \frac{x_i}{m} &= n \\ \Rightarrow m &= \sum_{i=1}^n \frac{x_i}{n} \end{aligned}$$

In other words, the best estimate of the expectation value m is the unweighted mean of the individual count rates. Therefore, applying no weighting factors at all was preferred to the usual method of weighting $\propto 1/\sigma^2$ which would spuriously favour pixels with low count rates.

2.3 Combination with older GHRS Data

In order to improve the signal-to-noise of the GHRS data, a combined spectrum consisting of all new individual exposures and those of KRW 96 has been calculated. This combined spectrum, though, provides only a small increase in S/N by 0.5...2, as compared with the new spectrum (see Figures 1 and 3).

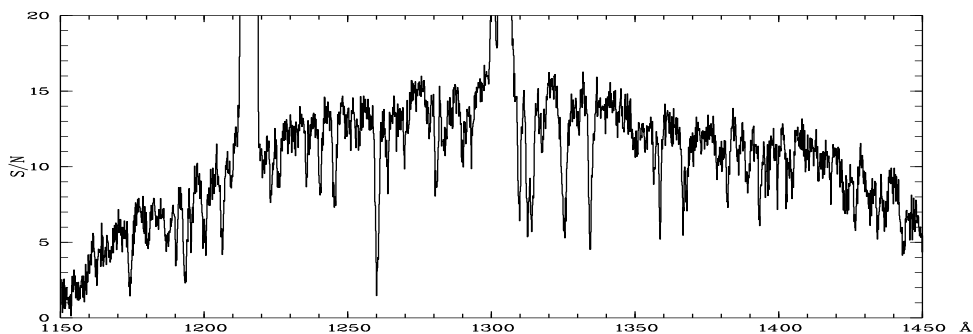


Figure 3: Signal-to-noise of combined GHRS spectrum obtained from new individual exposures and those of KRW 96

In the face of possible introduction of further errors by the combination with older data, resulting from uncertainties in the wavelength calibration, and the minute quality improvement, only the new spectrum has been used throughout this work.

3 Continuum Definition

The calculation of a reliable continuum is severely affected by the combination of high line density and low resolution of the data. Complex blends smeared by the instrumental SSF might reduce the flux over widespread regions, so that possibly no true continuum is visible at all over considerable ranges of the spectrum. Yet, once a continuum is defined, it can be checked for consistency after the process of line identification.

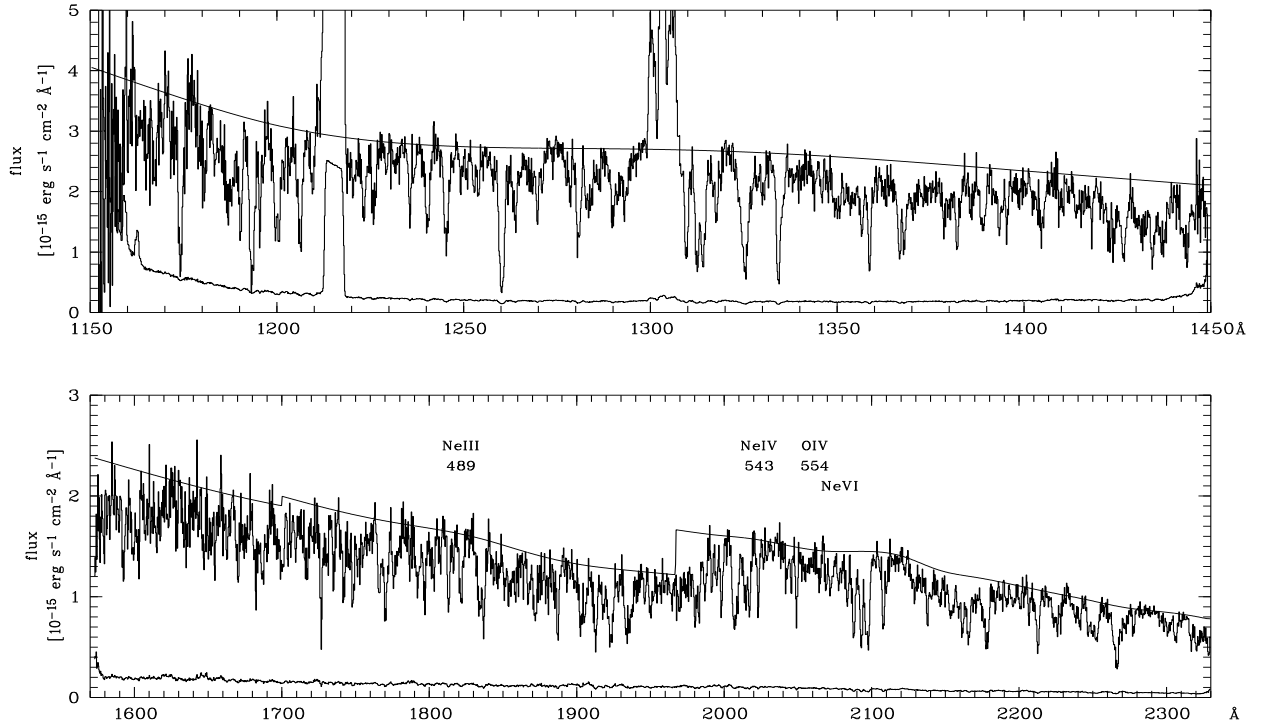


Figure 4: Reddening corrected fluxes and calculated continuum of the HST data with emission lines

The continuum definition was performed in several steps. The median filtered spectrum was divided into equally sized intervals. In each of them the maximum was determined and its wavelength and flux value were stored in a table. A preliminary continuum was calculated by a smoothed spline interpolation of this set of points. Now each flux value deviating by more than 1.5σ from the corresponding continuum flux was replaced by the latter one. Finally the whole procedure was repeated, allowing for interactive addition or removal of points from the table before the final interpolation was carried out.

Since the FOS spectrum was already known to contain two Lyman edges at $z = 0.864$ and $z = 1.157$ (VR 95), continua were independently calculated for the three spectral ranges separated by $\lambda = 1699.8 \text{ \AA}$ and $\lambda = 1967.0 \text{ \AA}$. As it turned out, only the absorber at $z = 1.157$ is confirmed as a LLS. The edge corresponding to $z = 0.864$, if present at all, hints at a neutral hydrogen column density of only $\approx 10^{16} \text{ cm}^{-2}$. The results are shown in Figure 4, which displays the flux, the 1σ error and the continuum. The flux has been corrected for interstellar reddening (Seaton 1979) with $E(B-V)=0.05$, which corresponds to a column density $N(\text{H I}) = 2.9 \cdot 10^{20} \text{ cm}^{-2}$ resulting from the analysis of ROSAT/PSPC data of HS1700 (Reimers et al. 1995), and the error has been appropriately propagated. Possible emission lines of Ne III-Ne VI and O IV are revealed. In particular at the expected position of Ne v 568 a considerably prominent emission feature can be seen. Unfortunately the corresponding lines of Ne v at 357 \AA and 480 \AA fall into regions of absorption and cannot be detected. It should be kept in mind though, that absorption features at these positions might be contaminated by overlaying emission from these lines.

After the line identification, regions apparently free of absorption were checked for ex-

Table 2: Wavelength regions apparently free of absorption

λ [Å]	identified Lines	Redshift z
1176..1179 Å	none	
1272..1277 Å	He I 537	1.371
	He I 515	1.4735
1319..1322 Å	none	
1406..1409 Å	none	
1624..1628 Å	N III 684	1.371
	N III 685	1.371
	S VI 944	0.722
1692..1695 Å	C II 594	1.8451
	N III 684	1.4735
	Si IV 1393	0.214
1824..1830 Å	Ne VIII 770	1.371
1890..1896 Å	N IV 765	1.4735
	N II 529	2.579
2030..2040 Å	Ne V 568	2.579
	S VI 944	1.1574
	S IV 748	1.725
2112..2120 Å	S IV 744	1.8451
2218..2222 Å	none	
2230..2234 Å	Si II 1190	0.8643
	Ne VIII 780	1.8451
2280..2294 Å	none	
2311..2315 Å	none	

pectedly strong lines. Table 2 contains wavelength ranges over which the normalized flux equals approximately unity. As can be seen in the synthesized spectrum (Appendix D), all of them contain either only presumably weak lines or no line identification at all (see §4.2 for details about the individual absorption systems).

4 Line Identification

Because of the low resolution of the data, the shape of the lines is dominated by the gaussian shape of the instrumental profile. As a first step, the spectrum was searched for absorption lines of equivalent widths exceeding a 3.5σ limit. In order to derive equivalent widths, the features were fitted by gaussian profiles, using the Levenberg-Marquart algorithm (Press et al. 1986). To account for the numerous blends, in many cases the sum of several gaussians (each providing three degrees of freedom : amplitude, FWHM, position) had to be inserted into one single fitting process. But still most of the individual gauss curves are associated with numerous identifications.

Following Schneider et al. (1993), the strongly wavelength dependent 1σ detection limit has been calculated as

$$\bar{\sigma}(EW)_i = D_i \left(\sum_{j=j_1}^{j=j_2} P_j^2 \bar{E}_{i+j-J_0-1}^2 \right)^{1/2} / \sum_{j=j_1}^{j=j_2} P_j^2$$

where D_i is the number of angstroms represented by each wavelength bin, P_j the array of the instrumental SSF consisting of $(2J_0 + 1)$ elements and \bar{E}_i the interpolated 1σ error of the i 'th pixel. j usually runs from 1 to $(2J_0 + 1)$ unless the pixel in question is located close to the edge of the spectrum or the SSF array contains more elements than the spectrum (see Schneider et al. 1993 for details about this formula). In regions of absorption the error had to be interpolated in order to avoid underestimation of the detection limit due to the reduced flux error.

Table 24 in Appendix B contains all absorption features detected above the 3.5σ limit together with the line identifications. Line parameters used for the identification, are listed in Table 23 in Appendix A.

4.1 Interstellar Absorption Lines

Several strong interstellar absorption lines are identified in the GHRS data. The absolute wavelength calibration has been carried out by assuming that they are located at $z = 0$. 21 cm H I observations, though, indicate that this assumption is not strictly correct. For example, Lockman & Savage (1995) trace H I emission in a velocity range of -146 to +46 km/s in the direction of H1821+643. Metal absorption lines associated with this hydrogen gas would be blueshifted by ≈ 50 km/s. On the other hand, interstellar lines still provide the best reference for absolute wavelength calibration of the GHRS data. Largely based on the lines of Si II at 1190 Å and 1260 Å, S II at 1250 Å and 1253 Å and C II at 1334 Å, the GHRS spectrum has been shifted by 0.4 Å towards longer wavelengths. These lines appear to be either blended with presumably much weaker lines or not to be blended at all. Furthermore this correction fits well with the expected position of the N I triplet. Table 3 shows all identified interstellar absorption lines together with $\Delta\lambda = \lambda_0 - \lambda_{\text{obs}}$ (after the correction). Several lines fall into obvious blends that cannot in all cases be completely accounted for. Si III 1206 is located slightly redward of the center of a strong absorption feature. Shifting the spectrum further towards longer wavelengths in order to remove this discrepancy, however, cannot be reconciled with the positions of the reference lines mentioned above. Since this feature is broader than the instrumental SSF, it is likely to be a blend, though the only other identification (Ne VI 558 at $z = 1.1574$) cannot satisfactorily fill the gap. Proper motions of the interstellar absorber clouds might provide an explanation. Maybe the line does even consist of multiple, unresolved components.

Absorption lines of H I and O I at 1215 Å and 1302 Å respectively fall into regions of geocoronal emission and cannot be detected.

Unfortunately the FOS spectrum contains only one strong interstellar absorption line, Al II 1670, but it is obviously blended. Al III 1854 is located in a broad blend, but at the expected position of Al III 1862 no feature is detected. Therefore the wavelength calibration can only be carried out in terms of consistency with the redshifts of the absorber systems derived from the GHRS data and other observations of HS1700. As a result, no wavelength correction seemed to be necessary.

Table 3: Interstellar absorption lines

Ion	λ_0 [Å]	λ_{obs} [Å]	$\Delta\lambda$ [Å]
Si II	1190.42	1190.31	0.11
Si II ^b	1193.29	1193.33	-0.04
N I ^a	1199.97	1200.16	-0.19
Si III	1206.50	1206.18	0.32
S II	1250.58	1250.83	-0.25
S II	1253.81	1253.95	-0.14
S II ^b	1259.52	1260.22	-0.70
Si II ^b	1260.42	1260.22	0.20
C II	1334.53	1334.25	0.28
C II*	1335.71	1335.64	0.07
Si IV ^b	1393.76	1393.51	0.25
Si IV ^b	1402.77	1402.42	0.35
Al II ^b	1670.79	1670.01	0.78

^a : actually a triplet of lines at 1199.55 , 1200.22 and 1200.71 Å

^b : obvious blend

4.2 Extragalactic Absorption Systems

The wavelength of a particular absorption line depends on two quantities, the rest frame wavelength and the redshift z . Yet, the ratio of different lines originating at the same redshift is independent of z . Therefore, the spectra were plotted over logarithmized wavelength and searched for series of lines showing the characteristic wavelength ratios of the Lyman series, i.e. the characteristic difference in position in the logarithmic plot. On this basis five absorption systems were discovered apart from the one at $z = 1.1574$ easily detected from its Lyman edge. Applying the same method to metal line multiplets is prohibited by the high line density. Therefore, redshifts of the other systems have been taken from other observations (VR 95, R-P 95, PRR 96, TLS 97) and checked for consistency with the present spectra. Furthermore, the data suggest the existence of one new MLS at $z \approx 0.09$.

Comments on the individual Absorption Systems

a) $z = 0.09$

The broad absorption feature located at 1325 Å is identified by KRW 96 with numerous neon lines and C III 386 at $z = 2.433$. These lines are, however, not likely to account for such high optical depth and the presence of Ly α absorption is probable. The C IV doublet fits very well into features at the corresponding positions, whereas Si III falls into the edge of a complex blend. At the expected positions of Si II 1260 weak absorption is detected and the N V doublet is located in a complex blend. Unfortunately, C II 1334 and the Si IV doublet are outside the observed range but reexamination of the old GHRs data of KRW 96 yielded an absorption line about 0.5 Å shortward of Si IV 1393. This discrepancy is

still compatible with the inadequate precision of the redshift derived for this system. No information can be inferred for Si IV 1402, and C II 1334 might be present in the edge of a blend. Considering the poor evidence for this MLS, its existence might be called into doubt, but Reimers et al. (1989) detected a galaxy at 11" (i.e. ≈ 30 kpc; $H_0 = 50 \text{ km s}^{-1}\text{Mpc}^{-1}$) from HS1700 with $z \approx 0.086$. Given the uncertainties of both redshift estimates, the MLS might well be associated with this galaxy.

b) $z = 0.214$

This system has been identified by KRW 96 who detect Lyman series lines up to Ly δ , but its designation as a MLS was not certain. The new data cover only the positions of Ly β and Ly γ , which apparently are both blended. A distinct absorption line without further identification is revealed at the expected position of O VI 1031. Absorption is also visible for C II 1036 and the C IV doublet, and O VI 1037, C II 1334, C III 977, N III 989 are all located in complex blends. No clear feature is detected for the Si IV doublet, and all intrinsically strong lines of Si II and Si III fall either into the noisy region of the GHRS data or in the gap between 1450 Å and 1570 Å. As reported by KRW 96 this system might be a member of the cluster Abell 2246 located 2' NW of HS1700 (Reimers et al. 1995), the brightest member of which has $z \approx 0.25$ (Hagen, priv. comm.).

c) $z = 0.5524$

Ly α and Ly β are clearly identified in the FOS spectrum. In particular Ly α fits very well into a single feature corresponding to no other potentially strong line and thus allows relatively accurate determination of the redshift. Series lines shortward Ly ϵ are covered by the GHRS data but fall into complex blends. Apart from O II 834, which is not detected above the 3.5σ limit, all oxygen and carbon lines, that is O II 832+833, O III 832, O IV 787, the O VI doublet and C II 903+1036+1334 fall into obvious blends. N IV 765 fits relatively well into the usual blend with the S II triplet, whereas no information can be inferred for N V 1238 which is blended with numerous other lines, and no distinct absorption is visible for N V 1242. At the expected position of S V 786 a broad feature is detected, but it might be contaminated by geocoronal Ly α emission. N II 915, Si II 1190+1193, Si III 1206 and the Si IV doublet are all located in complex blends. Only Si II 1260 coincides well with a weak feature.

d) $z = 0.722$

The Lyman series is detected at least down to Ly ϵ . Examining the GHRS data presented by KRW 96, no clear Lyman edge is seen at 1570 Å, but the flux might be reduced by ≈ 10 %. In any case, $\tau_{LL} < 1$ is found for the optical depth at the Lyman limit. In the optical data the Mg II doublet is unambiguously identified by TLS 97, who find $z = 0.72219$, and

PRR 96. In the new UV data O IV 787, O III 702 and O VI 1037 coincide with possibly unblended absorption lines. Strong, but blended absorption is found for O II 832-834, O III 832, O VI 1031, C III 977, N II 915 and N III 684+685+763. In spite of the usual blend with S II 763-765, N IV 765 is clearly detected. C II 1036+1334, N III 989, N V 1238+1242, S VI 944 and Si II 1193 fall into regions of weak, if any, absorption. S III 677+698, S IV 744+748, S V 786, S VI 933 and Si II 1190+1260 are all located in blends. Although Ne VIII 770 is found in the edge of the strong feature at 1325 Å and Ne VIII 780 fits considerably well into a feature otherwise not identified, the existence of lines of such highly ionized species is still uncertain. Excellent agreement is found for Si III 1206 at 2077 Å.

e) $z = 0.8643$

At the expected position of Mg II 2796 the optical data reveal a distinct absorption line (PRR 96, TLS 97), but according to TLS 97 the intrinsically weaker Mg II 2803 is only detected at 2.3σ and yields a slightly different z . They suggest that the stronger component could be part of a blend. No Fe II 2596+2600 absorption is found in the optical data (PRR 96). VR 95 report the discovery of a Lyman edge at 1700 Å but this range is only just covered by their data. In the present FOS data, a weak edge can be marginally seen (see the continuum definition above) corresponding to a logarithmized column density (in cm^{-2}) of $\log N \approx 16.0$ in contrast to 16.35 derived by VR 95.

Very strong absorption is found for all oxygen lines : O III 702, O V 629 and the O VI doublet. In the cases of O III and O V the features are significantly broader than the instrumental SSF (see Table 24 of Appendix B), but no other satisfying identifications are found. The existence of multiple components might provide an explanation. A similar behaviour is shown by C III 977, but possibly the O IV doublet at 554 Å of the absorber at $z = 2.29$ provides complementary absorption. On the other hand, the presence of metals in that absorber is far from certain (see below). N IV 765 is detected as constituent of a strong blend at ≈ 1425 Å, which may also contain the S II triplet. Weak absorption is detected at the positions of N V 1238 and N II 915, whereas N V 1242 and N II 644 fall into blends. C II 687+903 and N III 684+685+989 are all parts of complex blends. Strong, but blended absorption is also found for S III 677 and S IV 657+744+748. S VI 933 might be present in the edge of a blend at 1740 Å, but the intrinsically weaker S VI 944 is only detected at 2.6σ and lies close to He I 512 of $z = 2.439$. No information as to the presence of high ionization species like Ne VIII can be obtained for this system, since the only line, Ne VIII 770, is located within a complex blend. No feature is seen at the expected position of Si II 1190. Unfortunately, the stronger components Si II 1193+1260 are either blended or outside the spectral range.

f) $z = 1.1574$

The identification of this system as a LLS is based on the Lyman edge clearly visible at ≈ 1970 Å. Strong, though in several cases blended absorption is detected for Lyman lines from Ly β down to Ly7, the rest being lost in the edge or (Ly α) outside range. Perfect

coincidence found for Ly δ and Ly ϵ provides a reliable value for z . Whereas the Mg II doublet is unambiguously detected by TLS 97 and PRR 96, the latter authors do not find Fe II 2374+2382 but do not exclude the presence of Fe II 2586+2600. R-P 95 also report possible detection of Mg I 1828+2026. In the new UV data considerably strong, though blended absorption is found for O II 832-834, O III 833, O IV 553+608+787 and the O VI doublet. In contrast O IV 554, O V 629 and S IV 657 are well detected as individual features. The C II doublet at 903 Å, N III 763, N IV 765 and S II 763+765 are all situated in blends. Constraints for the C II column density are derived from the non detection of C II 687 in the GHRS spectrum of KRW 96. Only weak absorption is detected for S II 764 and N III 989, but C III 977 coincides perfectly with a strong feature at 2108 Å. Like N II 915, which is located in the Lyman edge, S V 786 and S VI 933 are obviously blended, but no feature can be seen at the expected position of S VI 944. Whereas Ne IV 541+543, Ne V 568 and Ne VI 558 are blended, Ne IV 542 coincides very well with a weak feature just below the 3.5σ detection limit. Hardly any information can be inferred from Ne VIII 770+780, since both are blended with presumably stronger lines. Similar problems arise for He I 584, which falls into the strong absorption feature dominated by the interstellar Si II 1260 line.

g) $z = 1.371$

Lyman series lines from Ly γ to Ly7 are clearly detected in the FOS spectrum. Ly γ and Ly6 appear not to be blended and provide the redshift. No metal lines are detected in the optical data and VR 95 consider this system an uncertain MLS candidate, but KRW 96 detect metal absorption in their GHRS spectrum. The new data cannot clearly resolve the uncertainties, as most heavy element lines either fall into blends or reveal only weak absorption below the detection limit. Although He I 584 fits relatively well into a feature at 1385 Å, missing absorption at the expected position of He I 537 raises doubts about this identification. No reliable information can be obtained for O II since the triplet around 833 Å together with O III 832 falls into the Lyman edge of $z = 1.1574$, and the triplet at 539 Å, in addition to being intrinsically weak, is located in a blend. Weak absorption allowing for different identifications is detected for O III 507+702 and O IV 787. The other O IV lines, the doublet at 554 Å and O IV 608, are located in complex blends. On the other hand KRW 96 found perfect coincidence for O V 629 with a single strong feature at 1490 Å. No lines are visible for N III 684+685+763. N II 915, the C II 903 doublet and the S II 765 triplet reveal only weak absorption, and N II 533, C II 687, N IV 765 may be present as parts of blends. C III 977 fits very well into a feature, but presumably it is at least partially accounted for by S III 698 of $z = 2.315$. S III 677+698, and the S VI doublet are all located in moderately complex blends, whereas no significant line is detected for S V 786. The Ne IV 543 triplet, Ne VI 558 and Ne VIII 780 are obviously blended, but no feature is detected for the intrinsically stronger Ne VIII 770. Ne V 568 corresponds well with a weak feature at 1348 Å otherwise identified with O II 391+392 of $z = 2.433$.

h) $z = 1.4735$

This absorber is identified by VR 95 who detect Ly α , Ly β and Ly γ . The new data cover only series lines below and including Ly ϵ , which, if detected at all, are blended. Doubts about the presence of metals are raised by the non-detection of heavy element absorption in the optical data. No convincing evidence has been found in the UV spectra either (see VR 95 and KRW 96). The doubts are confirmed by the examination of the new data, since O II 832+833, O III 507+702+832, O IV 787, C II 903 and N IV 765 are associated with weak, if any, features clearly below the detection limit. Only the O IV doublet 553+554 falls into a complex blend otherwise not completely accounted for. Hardly any information can be inferred from N III 684+685 and C II 687, since they are located in a blend associated with numerous other identifications. He I 537 fits relatively well into a weak feature at 1328 Å. Unfortunately the stronger component He I 584 is shifted to the noisy edge of the GHRS data and not detected above the 3.5σ limit.

i) $z = 1.725$

With $\log N = 17.05$ this system exhibits the largest neutral hydrogen column density of all absorbers towards HS1700 (VR 95). On the other hand TLS 97, PRR 96 and R-P 95 do not detect Mg II, Fe II or Al III. The strong line at 4551.6 Å suggested by PRR 96 to be a possible Al II line at $z = 1.7242$ is more likely to be associated with Ly α at $z = 2.744$. In this context, it is worth mentioning that R-P 95 report the detection of a system at $z = 2.7444$ with possible C IV absorption (see below). In the new data moderately strong but blended absorption is detected for O III 507+702+832, O IV 787 and O V 629. The O II 430 triplet fits well into a feature at 1172 Å, but the signal to noise is almost as low as 5 in this region of the GHRS spectrum. Furthermore, O II 834 is not detected above the 3.5σ threshold, the weaker components of this triplet being lost in blends. Little information can be inferred from C II 687, N III 684+685, S II 764+765, S III 677+698 and S IV 657, which are located in blends. Weak absorption is found for N II 644, C II 594, S II 763, S IV 744+748 and N III 763. The Ne III 488+489 doublet and Ne V 480 are located in strong blends, and the correspondingly high column densities derived for them may be called into doubt. Ne VII 465 and Ne VIII 780 may be present in broad but relatively weak blends and Ne VIII 770 is located in the outer wing of a strong line at 2098 Å.

j) $z = 1.8451$

VR 95 discovered this LLS on the basis of a Lyman edge at ≈ 2600 Å corresponding to $\log N_{\text{HI}} = 16.75$. From the position of the Lyman series lines they determined a redshift of 1.8465, but reexamination of their spectra revealed that all these lines are located in blends and therefore still compatible with the z derived by R-P 95 and TLS 97 from the optical data. The latter authors find the Mg II and the C IV doublet at $z = 1.84506$ and R-P 95 also detect the Si IV doublet yielding $z = 1.8451$. Reexamining the FOS data presented by VR 95, some metal lines covered by their spectra also appear to fit better with $z = 1.8451$

(for example O IV 787 and C III 977). Consequently, the new data have been analysed using this redshift. The O II 430 triplet as well as O III 507+702, O IV 608 and O V 629 are all located in blends. If the redshifts involved are correct, O III 702 is separated from Ly7 of $z = 1.1574$ by only 0.03 \AA , i.e. $\approx 2 \text{ km/s}$ in the absorber restframes. Therefore, they do even overlap before being convolved with the instrumental SSF and leave open a wide range of column densities. On the other hand, uncertainties in the redshift values combined with potential proper motions of the clouds still allow for possibly adequate separation of these lines (see §6.1.2). O IV 553+554 fall into the edge of the FOS data, where the continuum definition may be uncertain. O IV 787 is clearly detected as part of a blend at 2240 \AA . No absorption is seen at the expected positions of C II 594 and S IV 744, whereas C II 687, S IV 657+748, N II 644 the N III 685 doublet, N IV 765, the S II triplet, S III 698 and S V 786 are all located in obvious blends. S III 677 coincides very well with a feature at 1926 \AA , but contributions from N V 1242 and O IV 608 of $z = 0.5524$ and $z = 2.168$ respectively cannot be excluded. The Ne III 489 doublet, Ne V 480+568 and Ne VI 558 are all situated in blends. Weak absorption is found at the expected position of Ne VI 433, but Ne VII 465 fits relatively well into the edge of the strong feature centered at 1325 \AA . Good agreement is found for Ne VIII 770 with a single line at 2192 \AA , but doubts about this identification are raised by the non detection of the intrinsically weaker Ne VIII 780. He I 584 lies 0.3 \AA shortward of a distinct feature otherwise only identified with Ne VIII 770 of $z=1.1574$. Unfortunately, all other strong He I lines fall into the gap between the FOS and GHRS data.

k) $z = 2.168$

VR 95 unambiguously detect the Lyman edge and series lines down to Ly13. In the optical data TLS 97 find the C IV doublet at $z = 2.16797$. In addition, R-P 95 detect Si III 1206 and the Si IV doublet, but PRR 96 report non-detection of Fe II 2586+2600 and Al II 1670. The new data reveal a clear feature at the position of He I 584, but contributions from other lines are not excluded. The higher He I series lines provide no more accurate information, since they are all blended. The O II 430 triplet coincides well with a feature at 1363 \AA otherwise not identified. On the contrary, no lines are found for the intrinsically weaker triplet O II 392, whereas weak absorption can be seen for the triplet O II 539. Good agreement is found for O III 507, but numerous other, though presumably weaker identifications are also found. No further information can be inferred from O III 374+702 which, like O IV 553+608, are obviously blended. Perfect coincidence is found for O V 629, and O IV 554 is clearly detected as part of a blend at 1756 \AA . Whereas C II 687, C III 386, S III 677+698 and S IV 657 fall into moderately strong, but blended features, only weak absorption is detected at the expected positions of N III 684+685+763 and C II 594. N II 533+644 coincide well with features at 1690 \AA and 2042 \AA , but the former one is also associated with C IV 1550 of $z = 0.09$. Ne IV 543 and 541 might be present as weak 2.5σ features, the other component of this triplet being lost in a blend. Lines are also detected for Ne V 568 and Ne VI 401, but in both cases one other identification is found. Ne V 558 lies in a complex blend and provides no additional information.

l) $z = 2.189$

Although this system is clearly identified from the Lyman series lines by VR 95, it does not show heavy element absorption in the optical data (PRR 96). Doubts concerning its metal content are not removed by the new data. Weak absorption is found for the O II 392 triplet, whereas the other O II triplets at 430 and 539 Å as well as O III 507+702, O IV 553+554 and O V 629 are all located in complex blends. O IV 608 falls 0.3 Å shortward of a feature, which is otherwise only identified with Ne IV 542 of $z = 2.579$. C II 687 fits well into a line at 2191 Å, but the intrinsically weaker C II 594 is not detected. Perfect wavelength coincidence is found for C III 386, which is in good agreement with the detection of C III 977 reported by VR 95. No information is obtained from N III 374, which falls into a strong blend at 1193 Å, but no absorption is seen at the position of N III 685. Neither He I 584 nor He I 537 are detected above the 3.5σ threshold.

m) $z = 2.29$

Just like in the case of the system at $z = 2.189$, the metal content of this absorber is far from certain. VR 95 detect Ly α , Ly γ and higher series lines, but no C IV is found in the optical data (PRR 96). In the new UV data the O II triplets at 392 Å, 430 Å, 539 Å respectively and O III 507 are all located in complex blends. O IV 553+554 might complement a blend presumably dominated by C III 977 of $z = 0.8643$, but the intrinsically weaker O IV 608 as well as O III 702 are not detected above the 3.5σ limit. O V 629, though, fits very well into a feature at 2072 Å, which cannot be adequately accounted for by other identifications. Weak absorption is seen at the expected positions of C II 594+687 and N III 374, whereas C III 386 and N III 684+685 are seriously affected by blending. Hardly any information can be obtained for He I, since all lines down to He I 512 fall into complex blends.

n) $z = 2.308$

VR 95 identified this system on the basis of Ly α , Ly γ , Ly δ , Ly ϵ and Ly7. R-P 95 report the discovery of two components visible through several C I lines and detect the C IV doublet. They do not, however, find absorption by Si IV. According to TLS 97 closer investigation of the C IV doublet casts some doubt on its identification (see their paper for details). The new data reveal hardly any absorption for the O II triplets at 392 Å and 539 Å and O III 507, whereas the O II 430 triplet, O III 702, O IV 554+608 are located in complex blends. O V 629 might well be present as part of a blend at 2083 Å. Like C II 687, C III 386 and N II 533+644, the N III 685 doublet falls into an obvious blend, but the intrinsically stronger N III 374 is not detected. S III 677 might be present in the wing of a complex feature, but no line can be seen for the weaker component S III 698. Absorption is seen for S IV 657, Ne III 489, the triplet Ne IV 543, Ne V 357+480+568 and Ne VI 401+558, but in all cases other identifications are found as well. The He I lines down to He I 515 are all associated with regions of blended absorption.

o) $z = 2.315$

This metal rich system, first identified by VR 95 on the basis of a Lyman edge at $\approx 3020 \text{ \AA}$ and the series lines, reveals a complex structure in the optical data. R-P 95 and TLS 97 detect at least three components, the latter authors providing $z = 2.3150$, 2.3155 and 2.3164 respectively. Like PRR 96, TLS 97 identify absorption by the Si IV and C IV doublet and Si II 1526. Additionally, they find Al III 1854 and probably Al II 1670, which are not detected in the lower resolution data of PRR 96. R-P 95 also detect absorption by N V 1238+1242, Si II 1190+1193+1304 and C II 1335 as well as blended features at the positions of Si II 1260 and Si III 1206. Numerous other metal lines are identified in the new UV data. The O II 430 triplet and O III 507+374 are located in complex blends, but O IV 553+554+608 and O V 629 are clearly detected, although contributions from other lines cannot be excluded. O III 702 is located in the outmost edge of the FOS data, but in spite of continuum uncertainties hardly any doubts are cast upon its existence. Little absorption is found for the intrinsically weak O II 539 triplet and N II 644. Whereas C II 594 falls into the Lyman edge of $z = 1.1574$, C II 687 coincides very well with a feature at 2278 \AA otherwise only identified with O IV 608 of the uncertain MLS at $z = 2.7444$ (see below). C III 386, N II 533 and N III 374 lie in complex blends and thus provide little information, but N III 685 coincides well with a line centered at $\approx 2272 \text{ \AA}$. Whereas S III 677 is clearly identified, S III 698 and S IV 657 are probably present as vital constituents of blends at 2317 \AA and 2180 \AA respectively. Ne IV 543 of this system provides one of the best neon identification of the whole spectral range covered by the present data. Although seemingly part of a blend, it is clearly identified at $\approx 1804 \text{ \AA}$, the other two components of this triplet being lost in a complex blend. Ne III 489 falls close to the relatively weak He I 512 of $z = 2.168$, but nevertheless it is likely to substantially contribute to the feature. Ne V 357+480 and Ne VI 558 lie in complex blends, but weak absorption detected at the position of Ne V 568 provides constraints on the Ne V column density. Ne VI 401 fits well into a feature otherwise only identified with the intrinsically weak Ne III 488 of the system at $z = 1.725$. Obvious, though blended absorption is found for the He I lines down to He I 512.

p) $z = 2.37995$

TLS 97 detect this system only in the C IV doublet. Although the new data do not provide unambiguous identification of metal absorption at this redshift, several lines, namely O III 374+507, O IV 553+554+608, O V 629, C II 594+687 and N III 374+685 might well be present in blends. Whereas N III 684 is located in the outmost edge of a blend at 2315 \AA , no information can be derived from C III 386, which coincides with geocoronal O I emission.

q) $z = 2.433+2.439$

Another absorption complex revealing a complicated structure in the optical data (PRR

96, TLS 97). The latter authors detect the C IV doublet at $z = 2.43204, 2.43306, 2.43339, 2.43785, 2.43877$ and 2.44059 respectively (see their paper for details). They also find Si IV 1393 at $z = 2.43339$. In addition to these lines PRR 96 find a 2σ feature at the expected position of Si II 1526 at $z = 2.433$ but no significant absorption for Al II and Al III lines. R-P 95 also detect Si III 1206 and Si IV 1402 at $z = 2.4336$. Since the structure of this absorption complex is not resolved in the UV data, line identification has only been performed at the redshifts $z = 2.433$ and 2.439 . Blended absorption is found for the He I lines of both redshifts down to He I 522. Also for both redshifts the O II 539 triplet falls into blends, whereas the O II 392 triplet coincides well with an absorption line only for $z = 2.433$. O III 507, O IV 553+554 and O V 629 are clearly detected in both cases, whereas both components of O IV 608 as well as O III 374 of 2.433 fall into strong blends. Weaker features otherwise not satisfyingly accounted for are found for O III 374, C III 386 and S IV 657 of $z = 2.439$. N III 374 (2.433) is located in a blend, but N III 374 (2.439) and S IV 657 (2.433) are not detected above the 3.5σ threshold. N II 533 at both redshifts and N II 644 (2.433) are located in complex blends, and N II 644 (2.439) coincides well with a 2.8σ feature at 2217 \AA . Weak absorption is found for both components of Ne IV 542, Ne V 357, the $z = 2.433$ line Ne V 480 and the $z = 2.439$ lines Ne III 488, Ne IV 541. Ne III 489 (2.439), Ne IV 543 (2.439) and Ne VII 465 (2.433) might be present in the wings of more complex features. All other neon lines covered by the present data, that is Ne III 488, Ne IV 541+543, Ne VI 401+558 at $z = 2.433$ and Ne V 480, Ne VI 401+558 at $z = 2.439$ are situated in blends and therefore do not provide very reliable information.

r) $z = 2.579$

VR 95 identified this system on the basis of Ly α , Ly β , C IV, O V and O VI lines. R-P 95 and PRR 96 also find C IV absorption, but give redshifts of $z = 2.5784$ and 2.5783 respectively, whereas TLS 97 detect two components of C IV at $z = 2.57813$ and 2.57884 . The new data provide little information about He I, as all lines down to He I 512 are located in complex blends probably dominated by other lines. The same applies for N II 644, the O II 392 triplet and O IV 608, but hardly any absorption is found at the expected positions of O II 539.0+539.5 and N II 533. O III 507 fits well into a 4.2σ feature at 1816 \AA , and O IV 553+554 coincide with two features clearly present in the vicinity of the Lyman edge of $z = 1.1574$. O V 629, O III 374 and N III 374 might well be present in blends at 2252 \AA and 1337 \AA respectively. Strong, but possibly blended absorption is found for C III 386. Features otherwise not reliably accounted for can be seen at the positions of Ne IV 542+543, whereas Ne IV 541 like Ne III 488+489, Ne V 357+480 and Ne VI 401+558 falls into a blend. Constraints for the Ne V column density are derived from the non-detection of Ne V 568. A weak line just below the 3.5σ limit is found for Ne VII 465, but other identifications are also possible.

s) $z = 2.7125$

This system has been identified in the optical data, although slightly different redshifts

are derived. R-P 95 detect the C IV doublet at $z = 2.7102$, whereas PRR 96 and TLS 97 additionally find N V 1238+1242 and report $z = 2.7126$ and 2.7125 respectively. The new data reveal only weak absorption for the O II 539 and O II 430 triplets, O III 507, O IV 553+554+608 and Ne III 489. The O II 376 doublet, N III 374 and C III 386 are located in blends, and N II 533 lies in the Lyman edge of $z = 1.1574$, providing little information. Ne IV 541+542 are lost in complex blends, but constraints are provided by Ne IV 543, which lies in the outmost wing of a strong line. Although Ne V 357+568 fit considerably well into lines at 1329 Å and 2110 Å respectively, their existence is called into question by the non-detection of Ne V 480. In contrast, Ne VI 558 and Ne VII 465 might well be present as parts of more complex blends. This result does not come as a surprise, since higher ionization stages are more likely to prevail in this QSO associated system.

t) $z = 2.7444$

R-P 95 report possible C IV absorption at $z = 2.7444$, but find no other metal lines. Ly α might well be present as a feature detected by PRR 96 at 4551.6 Å, although they identify it with Al II 1670 of $z = 1.7242$. On the other hand, this Al II identification is rather uncertain (see above). The new data do not remove doubts concerning the presence of metals. O III 507 and O IV 553 agree well with lines at 1898 Å and 2071 Å respectively, but other reliable identifications are found as well, and the intrinsically stronger O IV 554 component reveals only weak absorption. O III 374, though, fits well into a relatively weak feature otherwise only identified with N III 374 of this system, possibly present in the wing of this line. C III 386 is located in the noisy edge of the GHRS data and provides no additional information. He I 584+537+522 fall into blends but still put useful constraints upon the He I column density.

u) Summary of all absorption systems

Table 4 lists all absorption systems together with ions reliably detected in either optical or UV data and/or a brief comment concerning the designation as MLS.

Table 4: Absorption systems

z	comment
0.09	Ly α , C IV
0.214	O VI, C III
0.5524	C III ^b , N IV
0.722	O III, O IV, O VI, N IV, Si III, Mg II ^{d,e}
0.8643	O III, O IV ^b , O V, O VI, C III, N IV, Mg II ^{d,e} ?
1.1574	O III, O IV, O V, C III, S IV, Mg II ^{d,e}
1.371	O IV?, O V ^b
1.4735	uncertain
1.725	no unambiguous identification
1.8451	O III ^a , O IV, O V, C III ^a , C IV ^{a,c,e} , Mg II ^{c,e}
2.168	O IV, O V, C III ^a , C IV ^{c,e} , Si III ^c , Si IV ^c
2.189	C III ^a ? uncertain
2.290	O V? uncertain
2.308	C IV ^{c,e} ?, O V? no unambiguous identification
2.315	O III, O IV, O V, C III ^a , C IV ^{d,e} , Si IV ^{d,e} , S III, Ne IV
2.37995	C IV ^e ; no unambiguous id in new UV data
2.433	O III, O IV, O V, C IV ^{d,e} , Si IV ^e
2.439	O III, O IV, O V, C IV ^e
2.579	O III, O IV ^a , C IV ^{a,c,d,e}
2.7125	C IV ^{c,d,e} , N V ^{d,e} ; no unambiguous id in new UV data
2.7444	C IV ^c ? uncertain

^a : data of VR 95

^b : data of KRW 96

^c : data of R-P 95

^d : data of PRR 96

^e : data of TLS 97

5 Column Densities

The standard, single-component absorption line depends upon three parameters : the position λ , the column density N and the doppler parameter b (see Appendix A). Alternative, but equivalent parameter sets are also used, e.g. the central optical depth τ_0 instead of N . Although the absorption of one particular transition originating in an absorber cloud often consists of several components with different parameters τ_0 and b , reliable column densities can be derived from the analysis of one composite line with a single Gaussian velocity distribution as long as the parameter distribution of the individual components is reasonably well behaved (Jenkins 1986).

Unfortunately, the analysis of the present data is still affected by a variety of problems described in §5.1. Most analysis techniques described in §5.2 are therefore not applicable to the data.

5.1 Error Sources

The derivation of accurate column densities from the present data is difficult for several reasons. As a result of the high line density in combination with the low resolution of the data, the vast majority of lines is blended. In this context, one has to distinguish between two kinds of blends.

- (a) The blending might simply be a result of the convolution of the Voigt profiles with the instrumental SSF. In this case, the lines are adequately separated before the convolution.
- (b) In some cases, though, lines are located so close to each other, that they do even overlap before being convolved with the SSF.

Let $f(\lambda)$ and $g(\lambda)$ describe the flux (before convolution with the SSF) in the presence of just one line respectively. The combined spectrum is then $f \cdot g$. In case (a) this may be written as $f \cdot g = f + g - 1$. Figure 5 illustrates this relation in the case of Ly γ at $z = 0.8643$ and N IV 765 at $z = 1.371$. If s represents the instrumental SSF, after convolution the spectrum will always be $[f \cdot g] * s$, which in case (a) can be written as $f * s + g * s + 1$. That is, the final spectrum is just the sum of the spectra produced by the individual lines. If the parameters of one line, for example a Lyman series line, are sufficiently accurately known, it can simply be deducted from the spectrum and the difference can be used in order to fit the second line. This possibility has been exploited in the determination of the line parameters (see below).

The accuracy of the results is also reduced by uncertainties in the continuum. In particular the possibility of underestimating the continuum, as outlined in §3, might result in too small column densities. Weaker lines are more severely affected by this kind of error.

Apart from the systems unambiguously detected in optical data, the redshifts are also subject to inaccuracies. Proper motions of individual components in the absorber clouds enhance this problem.

Furthermore the structure of the lines is blurred by the instrumental SSF and consequently multiple components are not resolved and reliable velocity parameters are hard to come by, especially if only one line of a specific ion is observed. Figure 6 illustrates the implications of inaccurate Doppler parameters. The O V 629 line at $z = 2.168$ is plotted for different

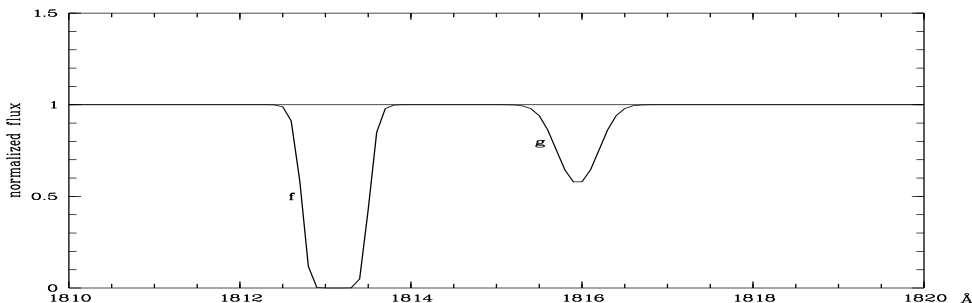


Figure 5: Ly γ of $z = 0.8643$ (left) and N IV 765 of $z = 1.371$ (right)

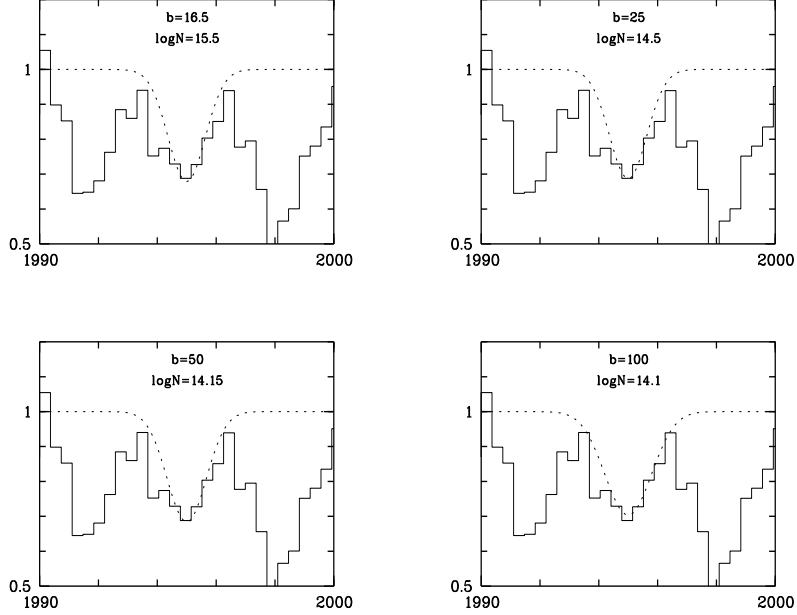


Figure 6: O v 629 at $z = 2.168$ fitted for different Doppler parameters

combinations of $\log N$ and b . This effect will play an important role in the investigation of the absorber at $z = 2.168$ in §6.1.1.

Finally, there is always the danger of unrecognized line saturation.

5.2 Analysis Techniques

Several techniques are commonly used in order to derive column densities of individual ions. The "apparent column density method" uses the observed optical depth per velocity interval $\tau_{\text{obs}}(v)$. Following Savage & Sembach (1991), the apparent column density per velocity unit is calculated as

$$N(v) = \frac{m_e c}{\pi e^2} \cdot \frac{\tau(v)}{f \lambda}$$

and the total column density is then

$$N = \frac{m_e c}{\pi e^2 f \lambda} \int \ln \frac{I_0(v)}{I(v)} dv$$

where I describes the line profile, I_0 the continuum intensity and f is the oscillator strength of the transition. Even if the line is not well-resolved, this method provides good results,

as long as the profile is not affected by unrecognized saturation. Furthermore, the degree of saturation can be assessed, if two or more lines with different values of $f \cdot \lambda$ of the ion in question are observed. For details about this method the reader is referred to Savage & Sembach (1991). In the case of the present data, though, measurements of this kind are hardly applicable, since most lines are located in blends sometimes not even completely accounted for. It is virtually impossible to find out to what extent the optical depth in a blend can be attributed to one particular line.

Another way to obtain column densities is the "curve of growth analysis". The equivalent width of a line, as measured in the absorber's rest frame, depends on the column density N and the velocity parameter b . If the equivalent widths of two or more transitions of a species are known, information about N and b can be derived. In Figure 7, for example, the

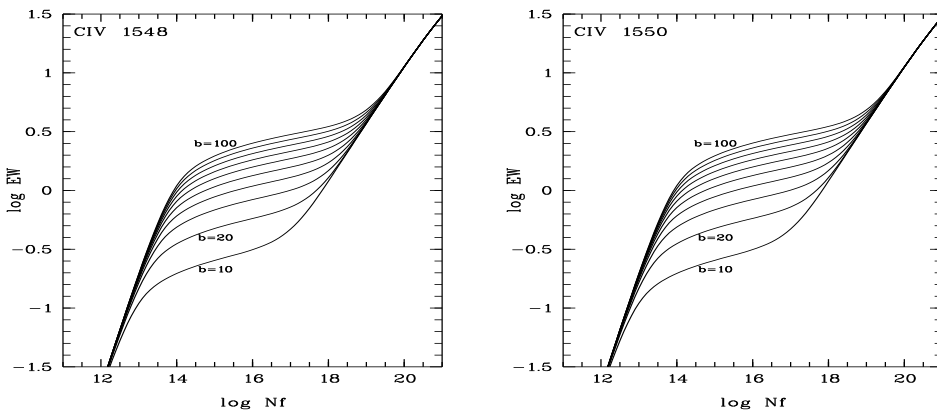


Figure 7: Curves of growth of the C IV doublet

curves of growth of C IV 1548 and C IV 1550 are displayed. N , b and the equivalent widths are measured in cm^{-2} , km/s and \AA respectively. Both curves look quite similar, since the difference of the transitions is largely due to the oscillator strength f incorporated into the y-axis. This method, however, suffers from the same difficulties as mentioned above. Due to the blending problem, reliable equivalent widths can only be obtained for a few lines.

Line fitting routines can be used to fit Voigt profiles convolved with the instrumental SSF. By minimizing χ^2 they can supply the redshift z , the Doppler parameter b and the column density N for each component (see for example Lanzetta & Bowen 1992 and references therein). The present UV data, though, are not appropriate for such fitting routines. Because of the low resolution, derived velocity parameters are highly uncertain and, consequently, so are the column densities. Furthermore, there might always be contributions from unidentified lines.

As a result, the present data were analysed with the only applicable, though least objective method : fit by eye.

Unfortunately it is impossible to quantify the uncertainty of the results. The variety of error sources described in §5.1 cannot be quantified in the form of a 1σ error. Furthermore, the metal abundances are neither necessarily upper nor lower limits. The fitted column densities may be too large because of unrecognized blending or wrong velocity

parameters. Too small column densities might result from continuum underestimation, inaccurate redshifts, unresolved saturation or once again from wrong velocity parameters.

5.3 Results

Using David Mar's Xvoigt, version 3.0, Voigt profiles convolved with the instrumental SSF were interactively fitted to the normalized spectrum. Since the velocity parameters b are not known, adhoc assumptions had to be made. The velocity distribution takes into account thermal as well as turbulent motion of the absorbing particles, and thus b can be calculated from

$$b^2 = b_{\text{T}}^2 + b_{\text{turb}}^2 = \frac{2kT}{m_{\text{ion}}} + b_{\text{turb}}^2.$$

Values for b derived from high quality optical data usually lie in the range of 10-40 km/s. But multiple components not resolved in UV data might give rise to greater composite velocity parameters. Assuming a turbulence dominated velocity distribution, all metal lines were fitted by eye for several values of b : 100 km/s, 50 km/s and the value derived from the hydrogen lines of the absorber in question (usually ≈ 30 km/s). In order to assess the impact of substantially smaller b values on the final results for the metal abundances, the lines of the system at $z = 2.168$ were also fitted for $b = 16.5$ km/s, which TLS 97 derived from their high quality data for the C IV doublet of this absorber (see §6.1.1). The procedure was carried out in several steps. First of all, only lines of those species were fitted, for which either the column density was known from a Lyman edge, or else two or more lines obviously not affected by blending problems were unambiguously detected. These lines were deducted from the spectrum according to the relation described in §5.1, and the resulting spectrum was fitted again. This step was repeated for a couple of times, and the resulting line parameters were used to calculate a synthetic spectrum, which was compared with the data and checked for consistency. In an iterative process several adjustments still had to be made, in particular corrections for "true blends" (i.e. case (b) of §5.1) hitherto unrecognized. If a line of a particular species is not detected above the 3.5σ limit and all stronger lines are either lost in complex blends presumably dominated by other transitions or outside range, only an upper limit for the column density is given, and the ion in question has not been included in the calculation of the synthesized spectrum. The same applies, of course, in the case of the non-detection of the strongest line of an ion. If all lines are located in complex blends with stronger lines, only conservative upper limits for N are given. Atomic parameters used for the calculations are summarized in Appendix A, and in Appendix D the observed and synthesized spectra are displayed together with all line identifications.

It can be seen, that there is still plenty of absorption not adequately accounted for by the lines and absorber clouds considered in this work. Several factors might be responsible for this absorption :

1. Ly α clouds are not considered in the calculation and certainly provide some contribution in the form of Lyman series lines and maybe metal lines (Songaila & Cowie 1996).
2. Although a total of 21 MLS and LLS candidates have been identified in the course of time, there might still be additional, undetected MLSs.

3. Some systems reveal a complex structure in the optical data, which has not strictly been taken into account in the calculation (for example the complex at $z = 2.432 - 2.441$).
4. The existence of unknown transitions of considerable strength cannot be excluded. Thus the incompleteness of the line list might be responsible for missing identifications to a certain extent.
5. Continuum uncertainties in both directions can result in missing absorption in the calculated spectrum. In many cases several lines of one particular ion are observed. In the fitting procedure the lines must not produce stronger, but are allowed to cause weaker absorption than observed, since there is always the possibility of a blend. Consequently the line parameters are restricted by all lines, and either an overestimation or an underestimation of the continuum at the expected position of one line will somewhere cause overabundant absorption in the observed spectrum with respect to the calculated one.

6 Ionization Models

The source of ionization of the intergalactic medium (IGM) is still a matter of discussion. Several authors have proposed mechanisms, appropriate for heating the IGM to sufficiently high temperatures required for scenarios of collisional ionization (see for example Tegmark, Silk and Evrard 1993 or Nath & Biermann 1993). On the other hand, photoionization must be taken into consideration and may even play the dominant role in ionizing the absorber clouds seen in QSO spectra (Steidel 1990).

TLS 97 derived upper limits for the gas temperature of absorbers at $z > 2$ from Doppler parameters of the C IV doublets. Unless the lines are artificially narrowed by noise, they find $T < 50,000$ K for four absorption systems, which does not produce enough C IV in collisional equilibrium (Sutherland & Dopita 1993). Although equivalent information is not available for systems at smaller redshift due to the low resolution of the UV data, photoionization models might well be an appropriate way to infer abundances in the moderate column density QSO absorbers at redshifts ≤ 2 , largely dealt with in this work.

The integrated flux of quasars and/or hot massive stars is likely to provide the primary contribution to this ionizing field (Haardt & Madau 1996), although in some cases local sources must be taken into account, as for example the effect of the observed QSO itself on associated systems. Haardt & Madau (1996) computed photoionization fields for different redshifts based on the QSO background, taking also into account the absorption and reprocessing of quasar radiation by discrete absorbing systems. Furthermore, they have shown that the observed quasars can provide enough hydrogen-ionizing photons to satisfy the proximity effect at $z \leq 4$. The proximity effect predicts a reduced Ly α line density in the vicinity of the QSO because of stronger hydrogen ionization by the quasar flux.

Assuming photoionization, cloud models have been constructed with Ferland's ionization code CLOUDY (Ferland 1993) for six absorber systems detected toward HS 1700. Following Bergeron et al. (1994) and KRW 96, two components of different, though constant hydrogen density have been modelled for each absorber system. Both components are assumed as plane parallel slabs illuminated on one side by the intergalactic ionizing field

computed by Haardt & Madau (1996), whose z is closest to the studied absorption system. The characteristics of the low ionization (i.e. high hydrogen density) phase (LIP) are constrained by the neutral hydrogen column density, which has been required to reproduce the observed one. The size of the high ionization (low hydrogen density) component (HIP) was chosen to be either 50 or 100 kpc (cf. Bergeron et al. 1994, who derived 67.8 kpc in their two component model for an absorber at $z = 0.7913$ toward PKS 2145+06). In order not to introduce too many free parameters, both phases have been assumed to have identical metallicities.

The heavy element abundances have been determined in an iterative process. Starting with reasonable uniform metallicities for all elements relative to solar ($[M/H] = -2$ at $z \approx 2$, $[M/H] = -1$ at $z \approx 1$), the hydrogen density of both components has been varied so as to reproduce the relative abundances of the different ionization stages of the elements (e.g. OIV/OV for the HIP), taking into account that intermediate ionization species are present in significant quantities in both phases. The individual metal abundances have then been adjusted to reproduce the observed column densities. In some cases the variation of the metallicities had an influence on the relative abundances of different ionization stages and the process had to be repeated.

Since lines of different ions of one element may arise in different phases, they may have different Doppler parameters. In general, for ions obviously associated with the lower ionization phase the column densities obtained for $b = b_{\text{HI}}$ have been used as reference.

Table 5: Solar heavy element abundances

He	0.1
O	$8.32 \cdot 10^{-4}$
C	$4.68 \cdot 10^{-4}$
N	$9.77 \cdot 10^{-5}$
Mg	$3.98 \cdot 10^{-5}$
Si	$3.72 \cdot 10^{-5}$
S	$1.86 \cdot 10^{-5}$
Ne	$1.26 \cdot 10^{-4}$

Solar abundances (see Table 5) as specified by number relative to hydrogen have been taken from Gehren (1988). The only exception is neon, for which Grevesse's (1989) value is used.

6.1 Results for individual Absorber Systems

6.1.1 $z = 2.168$

The photoionizing spectrum used for this absorber is the one calculated by Haardt & Madau (1996) for $z = 2.16$. The lines of this system reveal only one velocity component even in the high resolution optical data (TLS 97). Thus it might be described to some accuracy by a two component model. The column densities derived for different Doppler parameters are listed in Table 6 together with model values and physical parameters. Additional values for O VI, C III, N IV, N V and Ne VIII are taken from VR 95. Further-

Table 6: Two component cloud model for the absorber at $z = 2.168$ ionized by the radiation field from Haardt & Madau at $z = 2.16$. Column densities are measured in cm^{-2} , the velocity parameter b is given in km/s and the hydrogen density in cm^{-3} .

ion	observed column density				LIP	HIP
	$b=16.5$	$b = 25$	$b = 50$	$b = 100$	$\log n_{\text{H}} = -2.4$	$\log n_{\text{H}} = -3.4$
H I		16.85 ^a			16.85	15.7
H II					20.15	20.1
He I	15.1	14.5			15.75	13.3
He II					18.9	17.5
O II	≤ 14.3	≤ 14.2	14.2	14.2	12.9	10.9
O III	14.8	14.6	14.4	14.4	14.8	13.6
O IV ⁺	14.8	14.7	14.45	14.45	14.1	14.4
O V ⁺	15.5	14.6	14.15	14.1	13.2	14.4
O VI	15.0	14.7 ^a			12.2	13.8
C II	≤ 14.8	≤ 14.7	14.4	14.4	13.15	11.55
C III	14.5 ^d	13.9 ^a			14.5	13.4
C IV	13.94 ^c	13.6 ^a			13.8	13.55
N II	≤ 14.7	≤ 14.4	14.3	14.3	12.2	10.55
N III	13.8	13.7	13.7	13.7	13.9	12.95
N IV	14.5 ^d	14.0 ^a			13.55	13.55
N V		$\leq 13.8^a$			12.35	13.1
S II					12.25	10.45
S III	13.4	13.2	13.2	13.2	13.4	12.2
S IV	13.4	13.2	13.2	13.2	13.3	12.75
S V		$\leq 13.6^a$			12.45	12.6
S VI		$\leq 13.5^a$			11.55	12.15
Ne III					14.75	12.95
Ne IV	14.7	14.5	14.5	14.5	14.3	13.95
Ne V	14.7	14.6	14.5	14.5	13.7	14.55
Ne VI	15.0	14.7	14.6	14.6	12.5	14.45
Ne VII		14.5 ^b		14.2 ^b	10.55	13.35
Ne VIII		< 14.6			9.6	12.65
size [kpc]					11.0	100
$\log T[\text{K}]$					$2.5 \cdot 10^4$	$4 \cdot 10^4$

⁺ : at least one line of this ion is apparently unblended

^a : value taken from VR 95

^b : value taken from KRW 96

^c : value taken from TLS 97

^d : value chosen so as to resemble the line calculated by VR 95

more, TLS 97 provide $\log N = 13.94$ and $b = 16.5 \text{ km/s}$ for C IV and conclude that the corresponding lines are not significantly affected by unresolved saturation. The simple structure of the C IV lines in combination with the reliable velocity parameter provides an excellent chance to assess the impact of smaller values of b on the metal abundances. Therefore, all lines have also been fitted for $b=16.5 \text{ km/s}$. Since the majority of C IV is present in the LIP, at least for those ions also largely prevailing there, the corresponding column densities have been chosen as reference.

As listed in Table 6, the model fails to reproduce the observed column densities of very highly ionized species (O VI, Ne VII and Ne VIII). Although the observed column densities are far from certain, it is worth considering what kinds of modification of the model are required in order to reproduce these values, if they are true. The modifications, though,

lead to only slightly different metal abundances (compare with results for the absorber at $z = 1.8451$ in §6.2.1). They also predict smaller He I column densities, close to the observed value. On the other hand this discrepancy between observed and calculated column density of He I might also be explained in terms of the Doppler parameter. In the range dealt with here He I 584 is very sensitive to variations of the velocity parameter and decreasing b to 13 km/s provides sufficiently large values of $\log N_{\text{HeI}}$.

Table 7: metal abundances for the system at $z = 2.168$

	VR 95	KRW 96
[O/H]	-2.15	-1.37
[C/H]	-2.15	-2.31
[N/H]	-2.05	-1.49
[S/H]	-1.7	<-0.4
[Ne/H]	-1.3	<-0.66
[O/C]	0	0.94
[N/C]	0.1	0.82
[S/C]	0.45	
[Ne/C]	0.85	

Table 7 lists the metal abundances derived for this model in comparison with values presented by VR 95 and KRW 96. Two discrepancies between the new values and those of VR 95 are obvious :

1. Apart from carbon, VR 95 derive considerably larger metal abundances. This may be a result of two factors. VR 95 derive larger column densities, in part because they use the relatively small $b = 25$ km/s throughout. Furthermore, VR 95 calculated a one component model. The current model additionally uses a high ionization phase and thus simply contains more matter. VR 95 derive $\log N_{\text{HII}} = 19.9$ compared with 20.1 and 20.15 of the LIP and HIP of this model respectively. Consequently, lower metal abundances are needed in order to provide the observed heavy element quantities.
2. VR 95 derive a significant overabundance of oxygen and nitrogen relative to carbon. The model presented in this work leads to almost identical abundances for those three elements as compared with solar, although it still predicts neon and sulphur enrichment. Looking in more detail at the column densities fitted for $b = 25$ km/s and $b = 16.5$ km/s, this result does not come as a surprise. The carbon abundance is largely based on the lines C III 977 and C IV 1548+1550. In particular C III 977 is an extraordinarily strong line (oscillator strength $f = 0.768$) and therefore, in the range of parameters dealt with here, extremely sensible for small variations of b . Consequently a much larger column density is derived for $b = 16.5$ km/s. The only oxygen line of comparable strength ($f = 0.514$) is O V 629. Since O V for the most part prevails in the HIP, it might well have a larger velocity parameter and is indeed expected to do so, since a column density of $N_{\text{OV}}=15.5$ cannot be reconciled in the frame of the present models with the smaller values obtained for O III and especially O IV for any Doppler parameter. A larger b value for O V is also in good agreement with results

from Bergeron et al. (1994), who derive velocity parameters from the doublet ratio method and find an increase of line width with the ionization level.

These arguments, of course, do not exclude an oxygen and nitrogen overabundance relative to carbon, but they do show, that the observations are reconcilable with $[\text{O}/\text{C}] \approx [\text{N}/\text{C}] \approx 0$ at least for this absorption system.

Table 8: Two component cloud model for the absorber at $z = 1.8451$ ionized by the radiation field from Haardt & Madau at $z = 1.817$. Column densities are measured in cm^{-2} , the velocity parameter b is given in km/s and the hydrogen density in cm^{-3} .

ion	observed column density			LIP	HIP
	b = 30	b = 50	b = 100	$\log n_{\text{H}} = -2.2$	$\log n_{\text{H}} = -3.4$
H I	16.75 ^a			16.75	15.85
H II				19.65	20.1
He I	15.0			15.65	13.5
He II				18.4	17.6
O II	≤ 14.4	14.4	14.4	13.3	11.5
O III	15.0	14.7	14.5	14.8	14.15
O IV ⁺	14.9	14.7	14.7	13.9	14.9
O V	14.9	14.4	14.4	12.8	14.85
O VI	14.5 ^a			11.75	14.25
C II	≤ 14.3	14.3	14.3	13.45	12.25
C III	14.3 ^{a,*}			14.65	14.1
C IV	14.35 ^c			13.75	14.2
N II				12.3	10.95
N III	13.9	13.9	13.9	13.75	13.3
N IV	13.9	13.8	13.8	13.1	13.85
N V	$< 13.8^a$			11.9	13.35
S II	≤ 13.1	13.1	13.1	12.2	10.9
S III	13.2	13.15	13.15	13.2	12.55
S IV	≤ 13.3	13.3	13.3	12.9	13.05
S V	13.0	13.0	13.0	11.85	12.9
S VI	$< 13.6^a$			10.95	12.5
Ne III	14.6	14.5	14.5	14.45	13.15
Ne IV	14.85 ^b		14.7 ^b	13.8	14.15
Ne V	14.7	14.7	14.7	12.9	14.65
Ne VI	≤ 14.8	14.8	14.8	11.45	14.5
Ne VII	14.25	14.15	14.15	9.3	13.4
Ne VIII	≤ 14.3	14.3	14.3	-	12.65
size [kpc]				2.4	100
$\log T$ [K]				$2.1 \cdot 10^4$	$3.6 \cdot 10^4$

⁺ : at least one line of this ion is apparently unblended

^a : value taken from VR 95

^b : value taken from KRW 96

^c : value taken from TLS 97

* : VR 95's spectrum is reconcilable with $\log N = 14.6$ for $z = 1.8451$

6.1.2 $z = 1.8451$

The ionizing spectrum from Haardt & Madau at $z=1.817$ is used for this model. The list of column densities derived from the new data has been complemented with values from TLS 97 (who find $b = 32$ km/s for the C IV doublet), VR 95 and KRW 96, as outlined in Table 8. Some remarks, though, concerning the value for O III have to be made. The new data cover the lines O III 507+702. O III 507 is located in a strong blend at the noisy edge of the GHRS data and O III 702 forms a "true blend" (i.e. case (b) of §5.1) with Ly7 at $z = 1.1574$. If the redshift values are strictly correct, the lines are compatible with $\log N_{\text{OIII}} = 15.7$ for $b = 30$ km/s. However, if either line of the blend is displaced by as few as 30 km/s in its restframe, the lines do not overlap before convolution with the instrumental SSF. Therefore the smaller column densities derived on the basis of adequate separation of the lines are considered more reliable. Yet the large value has to be kept in mind as an upper limit. It is worth mentioning in this context, that VR 95, whose data also cover O III 832, derived $\log N = 14.7$. Yet they used a different redshift of $z = 1.8465$. A strong feature in their FOS spectrum identified with O III 832 does not coincide very well with neither $z = 1.8451$ nor their redshift. A blend seems to be possible, thus favoring the smaller column density.

Just like for the absorber at $z = 2.168$, the model fails to reproduce the column densities observed for highly ionized species as well as He I. As far as He I is concerned, a lower velocity parameter ($b \approx 20$ km/s) is able to reconcile observations and model. On the other hand, modifications of the model, considered in more detail in §6.2, do not only produce adequate quantities of highly ionized species, but also resolve the discrepancy found for He I.

Table 9: metal abundances for the system at $z = 1.8451$

	VR 95	KRW 96
[O/H]	-1.7	-1.12
[C/H]	-1.6	-1.72
[N/H]	-1.8	-1.29
[S/H]	-1.5	<-0.6
[Ne/H]	-1.2	-0.4
[O/C]	-0.1	0.6
[N/C]	-0.2	0.43
[S/C]	0.1	<1.12
[Ne/C]	0.4	

Metal abundances derived from this model, are listed in Table 9. Apart from carbon, VR 95 as well as KRW 96 derive larger metal abundances, which is for the most part a result of the additional matter introduced by the two component model used in this work. The results of VR 95 and KRW 96 are derived from one component clouds (cf., §6.1.1). In addition, the new data provide for the first time useful information for Ne V 568 located in regions of poor S/N in the data sets of VR 95 and KRW 96 and thus stronger constraints for the Ne V column density so far derived from Ne V 480 only. Finally, the strongest neon line Ne VII 465 is located in the blueward edge of a strong blend at 1325 Å. Consequently, the smaller redshift of $z = 1.8451$ leads to a smaller column density.

Reexamining the FOS data of VR 95, the feature associated with C III 977 is compatible with column densities as large as 14.6 for a Doppler parameter $b = 30$ km/s. Together with

the value for C IV taken from TLS 97 this compensates the decrease in carbon abundance introduced by the two component model.

6.1.3 $z = 1.1574$

Of all systems detected so far, this LLS shows the greatest variety of metal absorption lines in the new data. Information for numerous ionization stages of O, C, N, S and Ne are only obtained for this absorber. Values taken from VR 95 and TLS 97 supplement the set of column densities presented in Table 10. The Si III and Si IV lines, though, are located in complex blends in the spectrum of VR 95 and do not provide useful information.

Table 10: Two component cloud model for the absorber at $z = 1.1574$ ionized by the radiation field from Haardt & Madau at $z = 1.113$. Column densities are measured in cm^{-2} , the velocity parameter b is given in km/s and the hydrogen density in cm^{-3} .

ion	observed column density				LIP	HIP
	b=10	b = 30	b = 50	b = 100	$\log n_{\text{H}} = -2.6$	$\log n_{\text{H}} = -3.6$
H I		16.7			16.7	15.8
H II					19.65	19.9
He I	16.5 (b=15)	15.0			15.55	13.7
He II					18.4	17.6
O II	14.0	13.9	13.9	13.9	13.8	12.15
O III		15.8	15.0	14.85	15.3	14.6
O IV ⁺		15.6	15.0	14.7	14.5	15.25
O V ⁺		16.1	14.9	14.5	13.5	15.15
O VI		14.55	14.45	14.4	12.45	14.5
C II	≤ 13.7	13.5	13.5	13.5	13.7	12.6
C III ⁺		15.4	14.35	14.05	14.9	14.45
C IV					14.1	14.4
N II	≤ 14.0	≤ 13.8	13.8	13.8	12.6	11.35
N III		14.2	14.1	14.1	14.05	13.55
N IV		14.2	14.0	13.9	13.4	14.0
N V		$\leq 14.1^a$			12.3	13.5
S II	≤ 13.7	≤ 13.3	13.3	13.3	12.7	11.5
S III		$\leq 14.7^a$			13.8	13.1
S IV ⁺		13.8	13.7	13.7	13.5	13.5
S V		13.6	13.5	13.45	12.55	13.4
S VI		≤ 13.4	13.4	13.4	11.85	13.1
Ne III					14.75	13.5
Ne IV		14.5	14.5	14.5	14.2	14.35
Ne V		14.9	14.8	14.7	13.4	14.8
Ne VI		14.6	14.6	14.6	12.05	14.5
Ne VII					9.95	13.3
Ne VIII		≤ 14.7	14.6	14.6	8.7	12.5
Mg II	12.8 ^c				12.8	9.7
size [kpc]					6.0	100
$\log T$ [K]					$2.0 \cdot 10^4$	$3.1 \cdot 10^4$

⁺ : at least one line of this ion is apparently unblended

^a : value taken from VR 95

^c : value derived by TLS 97 for $b=6.5$ km/s

Table 11: Metal abundances for the system at $z = 1.1574$

	VR 95		KRW 96
[O/H]	-1.2	-0.82	-1.2
[C/H]	-1.3	-0.44	<-1.0
[N/H]	-1.5	<-0.79	-1.25
[S/H]	-0.9	<-0.6	-1.04
[Ne/H]	-0.9		<-0.8
[Mg/H]	-0.6		
[O/C]	0.1	-0.38	>-0.2
[N/C]	-0.2	<-0.35	>-0.25
[S/C]	0.4	<-0.16	>-0.04
[Ne/C]	0.4		0.2

Therefore, no reliable silicon abundance can be derived for this absorber. TLS 97 derive a velocity parameter $b = 6.5$ km/s for Mg II, which indicates, that Doppler broadening is dominated by thermal motions at least for the singly ionized species of this absorber. Therefore, column densities for O II, C II, S II and He I have also been measured by assuming $b = 10$ km/s and, in the case of helium, $b = 15$ km/s, which corresponds to velocity parameters expected for thermal motion and $b_{\text{HI}} = 30$ km/s. Except for He I, though, only slightly different column densities are found. The value for He I illustrates the extreme sensitivity of He I 584 for variations of b . Using $b = 10$ km/s for higher ionization species would lead to unreasonably high column densities (e.g. $\log N = 18.8$ for O III). Since these more highly ionized species are present for a larger range of ionization conditions (see e.g. Fig. 3 in Petitjean et al. 1992), they are much more likely to have a larger velocity spread than Mg II lines, and thus the values obtained for $b = 30, 50$ and 100 km/s are used as reference.

In contrast to the systems dealt with in the previous two sections, more reliable information about the O II and C II column densities can be obtained from O II 834 and C II 687. The model calculated as being photoionized by the radiation field from Haardt & Madau at $z = 1.113$ predicts O II and C II column densities close to the observed values. As far as N II and Ne VIII are concerned, only conservative upper limits are observed, and the discrepancies are not considered a problem of the cloud model.

No column density for C IV has been available for this absorption system. Therefore, the carbon abundance presented together with results for other elements in Table 11 is largely founded on C III 977.

Once again, the introduction of a two component model results in smaller metal abundances, as compared with VR 95. The discrepancy is particularly strong for carbon. VR 95 find slightly stronger absorption at the expected position of C III 977 and, since this line is rather insensitive to variations of $\log N$ in this range, a considerably larger column density of $\log N = 15.8$. In the absence of information about C IV, this leads to a smaller value of [C/H] derived from the new data. In spite of this discrepancy, though, the new data certainly confirm VR 95's result of similar oxygen, nitrogen and carbon abundances as compared with solar values.

Within the uncertainties, the new results agree well with the values, calculated by KRW 96 for a two component model.

6.1.4 $z = 0.8643$

While various elements reveal absorption for this system, exceptionally strong features coincide with the oxygen lines O III 702, O V 629 and, to a certain extent, O VI 1031+1037. The features, associated with the former two lines cannot be completely accounted for by using $z = 0.8643$. However, no other satisfying identifications are found. Either the redshift is slightly larger, though this collides with the positions of the Lyman series lines, or there are several components, or unidentified lines of other systems provide supplementary absorption. In any case, high column densities for oxygen are derived for this system resulting in an oxygen to carbon overabundance of $[O/C] = 0.8$. Higher velocity parameters might reduce this value. Unfortunately, in the high resolution optical data only Mg II is detected with moderate reliability (PRR 96, TLS 97). The latter authors find the weaker Mg II 2803 at 2.3σ and not in good alignment in redshift with Mg II 2796, for which a moderately complex 6.6σ feature can be seen. They leave open the possibility

Table 12: Two component cloud model for the absorber at $z = 0.8643$ ionized by the radiation field from Haardt & Madau at $z = 0.8813$. Column densities are measured in cm^{-2} , the velocity parameter b is given in km/s and the hydrogen density in cm^{-3} .

ion	observed column density				LIP	HIP
	$b = 10$	$b = 40$	$b = 50$	$b = 100$	$\log n_{\text{H}} = -2.8$	$\log n_{\text{H}} = -3.8$
H I		16.0			16.0	15.35
H II					18.85	19.4
He I					14.8	13.25
He II					17.55	17.15
O II					13.9	12.35
O III		15.4	14.9	14.7	15.25	14.8
O IV		16.0 ^b		15.3 ^b	14.65	15.5
O V		16.8	15.5	14.7	13.6	15.45
O VI		15.4	15.05	14.85	12.7	14.95
C II	≤ 14.8	≤ 14.0	13.9	13.9	12.95	12.0
C III		14.6	14.0	13.9	14.2	14.0
C IV		14.0 ^a			13.55	14.0
N II	≤ 14.8	≤ 14.3	14.2	14.2	12.4	11.25
N III		13.8	13.8	13.8	13.85	13.55
N IV		14.3	14.2	14.2	13.25	14.05
N V		13.7	13.7	13.7	12.3	13.7
S II	≤ 15.1	13.6	13.5	13.5	12.25	11.0
S III		13.7	13.6	13.6	13.65	12.8
S IV		13.7	13.65	13.6	13.4	13.35
S V		13.6 ^b		13.6 ^b	12.55	13.4
S VI		≤ 13.9	13.9	13.9	12.0	13.35
Si II	≤ 13.5	≤ 13.4	13.4	13.4	12.35	9.95
Si III		13.5	13.3	13.3	13.5	11.25
Si IV		$< 13.7^b$		13.6	13.35	11.5
Mg II	12.0 ^c	$> 12.28^d$			12.3	9.4
size [kpc]					1.5	50
$\log T$ [K]					$1.5 \cdot 10^4$	$2.6 \cdot 10^4$

^a : value taken from VR 95

^b : value taken from KRW 96

^c : calculated by TLS 97 for $b=6$ km/s

^d : value taken from PRR 96

Table 13: Metal abundances for the system at $z = 0.8643$

	VR 95	KRW 96
[O/H]	-0.4	-1.22
[C/H]	-1.2	-1.42
[N/H]	-0.9	<-0.2
[S/H]	-0.25	-0.66
[Si/H]	-0.7	-0.5
[Mg/H]	-0.7/-0.4	<-0.37
[O/C]	0.8	0.2
[N/C]	0.3	<1.22
[S/C]	0.95	0.63
[Si/C]	0.5	0.54
[Mg/C]	0.5/0.8	0.7
		<0.83

of contribution from unidentified lines. However, this result is compatible with a more complex structure of this absorber.

If the Mg II identification is true, the velocity parameter $b = 6$ km/s derived by TLS 97 suggests Doppler broadening dominated by thermal motion in the cases of singly ionized species. Consequently, the lines of these ions have been measured for $b = 10$ km/s as well. Apart from Si II 1190, though, all these lines are located in complex blends and provide only conservative upper limits. Considering also the uncertainties of the Mg II identification, this absorber is not regarded appropriate for the investigation of singly ionized elements. For the reasons presented in the previous section, absorption lines of higher ionization stages are assumed to have larger velocity parameters.

Results for this system computed with a photoionizing field as computed by Haardt & Madau for $z = 0.8813$, are presented in Table 12 and 13. In spite of the decrease of the metal abundances, normally resulting from a two component cloud model used in this work, only for nitrogen a significantly smaller abundance is found as compared with the values of VR 95. In part this is due to the fact that VR 95 used a higher neutral hydrogen column density of 16.35 in contrast to $\log N_{\text{HI}}=16.0$, obtained from the new FOS spectrum, by and large compensating the effect of different cloud models. As far as oxygen is concerned, VR 95 could derive information from the O VI doublet only, the other lines falling shortward of their FOS data range. Their calculated column densities for O III, O IV and O V are substantially smaller than the values derived by KRW 96 or from the new data, indicating a larger [O/H]. Furthermore, the new GHRS data provide stronger constraints upon the N III column density in the form of relatively weak absorption at the expected position of the N III 685 doublet, leading to a lower nitrogen abundance. Unfortunately, the results for carbon are rather uncertain. Although C III 977 is unambiguously detected at 1821 Å, contribution from the O IV 554 doublet at $z = 2.290$ cannot be excluded. If, on the other hand, this system has indeed a more complex structure, and O IV 553+554 of $z = 2.290$ are not present, the C III column density might be closer to the values of similar ionization stages of oxygen. To worsen the situation, the C IV doublet falls into the Lyman edge of the LLS at $z = 2.168$ and does not provide reliable information.

Within the uncertainties, the new results agree well with those derived by KRW 96.

6.1.5 $z = 0.722$

The Lyman edge of this system is located at 1570 Å, i.e. just outside the range of the FOS data. However, as outlined in §4.2, the data of KRW 96 are compatible with a reduction of the flux by $\approx 10\%$ corresponding to $\log N_{\text{HI}} = 16.2..16.3$.

The velocity parameter $b = 16.0$ km/s obtained for Mg II by TLS 97 indicates, that turbulent motion dominates the Doppler broadening. Lines of singly ionized species have also been fitted for this value, whereas more highly ionized elements are assumed to have larger velocity spreads than Mg II (see §6.1.3).

Compared with other absorbers, this system reveals particularly strong absorption at the expected positions of the O II 834 triplet. Although the model provides relatively large column densities for O II, C II and even N II, they still fall short of the observed values. Modifications required if these observed values are true are presented in §6.2.

The results obtained by using the ionizing field from Haardt & Madau at $z=0.6784$ are

Table 14: Two component cloud model for the absorber at $z = 0.722$ ionized by the radiation field from Haardt & Madau at $z = 0.6784$. Column densities are measured in cm^{-2} , the velocity parameter b is given in km/s and the hydrogen density in cm^{-3} .

ion	observed column density				LIP	HIP
	$b = 10$	$b = 25$	$b = 50$	$b = 100$	$\log n_{\text{H}} = -2.6$	$\log n_{\text{H}} = -3.9$
H I		16.3			16.3	15.35
H II					18.8	19.3
He I					15.3	13.3
He II					17.65	17.1
O II	14.8	14.7	14.6	14.5	14.1	12.1
O III ⁺		15.1	14.8	14.7	14.9	14.45
O IV		15.2	14.9	14.8	13.7	15.05
O V					12.45	15.0
O VI		14.6	14.4	14.4	11.3	14.45
C II	14.0	13.9	13.9	13.9	13.6	12.4
C III		14.8	14.1	13.9	14.45	14.25
C IV		14.0 ^a			13.3	14.15
N II	≤ 14.6	≤ 14.4	14.3	14.3	13.2	11.7
N III		14.0	13.9	13.8	14.05	13.85
N IV		14.4	14.1	14.05	13.0	14.25
N V		14.0	14.0	14.0	11.85	13.8
S II	≤ 13.4	≤ 13.3	13.3	13.3	12.5	11.1
S III		13.5	13.5	13.5	13.45	12.75
S IV		≤ 13.7	13.65	13.65	12.8	13.2
S V		13.4	13.3	13.3	11.45	13.15
S VI		≤ 13.7	13.7	13.7	10.55	13.05
Si II	≤ 14.0	≤ 13.6	13.5	13.5	12.45	9.8
Si III ⁺		13.4	13.2	13.2	13.4	11.05
Si IV		$\leq 13.6^a$			12.8	11.2
Mg II	12.78 ^c	$> 12.7^d$			12.7	9.55
size [kpc]					0.9	50
$\log T$ [K]					$1.5 \cdot 10^4$	$2.7 \cdot 10^4$

⁺ : at least one line of this ion is apparently unblended

^a : value taken from VR 95

^c : calculated by TLS 97 for $b=16$ km/s

^d : value taken from PRR 96 (unknown b)

Table 15: Metal abundances for the system at $z = 0.722$

	VR 95	
[O/H]	-0.75	<-0.32
[C/H]	-0.95	<-1.32
[N/H]	-0.65	<-0.2
[S/H]	-0.5	
[Si/H]	-0.85	
[Mg/H]	-0.4	
[O/C]	0.2	
[N/C]	0.3	
[S/C]	0.45	
[Si/C]	0.1	
[Mg/C]	0.55	

shown in Tables 14 and 15. Due to the effect of different cloud models (cf. §6.1.1) in combination with a slightly larger neutral hydrogen column density of $\log N_{\text{HI}} = 16.3$ used in this work, as compared to 16.2 of VR 95, the latter authors find larger abundances for oxygen and nitrogen. C III 977 is blended with O III 507 of the metal rich system at $z = 2.315$ and corresponding column densities are rather uncertain. VR 95 find $\log N_{\text{CIII}} = 16.0$, but obviously consider this an upper limit, since their model provides only 14.0. The C IV doublet is located in a complex blend at 2670 Å and allows for larger values than $\log N = 14.0$ (see their spectrum).

6.1.6 $z = 0.5524$

This system provides the lowest redshift at which a sufficient variety of metal absorption lines is detected. The neutral hydrogen column density is based on Ly α and Ly β . The photoionization field is the one computed by Haardt & Madau for $z = 0.5845$. C III 977 and N III 989 both fall into the gap between the GHRs and FOS data and therefore have been fitted using the spectrum of KRW 96. The results are displayed in Table 16. Since the nitrogen abundance depends heavily on the N IV column density and N IV 765 is severely affected by the blending problem, the value is rather uncertain. Similar problems arise for O III 832, although the contribution of the O II triplet is restricted by the non detection of O II 834.

The model, calculated for this absorber is able to reproduce the column densities of O II and C II. The metal abundances are presented in Table 17.

Table 16: Two component cloud model for the absorber at $z = 0.5524$ ionized by the radiation field from Haardt & Madau at $z = 0.5845$. Column densities are measured in cm^{-2} , the velocity parameter b is given in km/s and the hydrogen density in cm^{-3} .

ion	observed column density			LIP	HIP
	b = 25	b = 50	b = 100	$\log n_{\text{H}} = -2.8$	$\log n_{\text{H}} = -4.3$
H I	15.8			15.8	14.6
H II				18.4	18.9
He I				14.75	12.35
He II				17.2	16.4
O II	≤ 13.8	13.8	13.8	13.8	11.05
O III	14.7	14.6	14.6	14.65	13.65
O IV	14.7	14.6	14.6	13.65	14.6
O V				12.45	14.8
O VI	14.7	14.5	14.5	11.4	14.55
C II	13.5	13.5	13.5	13.5	11.65
C III ^d	14.5	14.1	14.1	14.4	13.75
C IV				13.4	13.9
N II	≤ 14.4	14.3	14.3	13.1	10.95
N III ^d	14.1	14.1	14.1	14.1	13.35
N IV	14.4	14.15	14.1	13.15	14.05
N V	≤ 14.1	14.1	14.1	12.05	13.9
Si II	≤ 13.2	13.2	13.2	12.55	8.4
Si III	13.5	13.3	13.2	13.5	9.8
Si IV	≤ 13.8	13.7	13.7	13.05	10.15
size [kpc]				0.5	50
$\log T$ [K]				$1.4 \cdot 10^4$	$2.8 \cdot 10^4$

^d : fitted for data of KRW 96

Table 17: metal abundances for the system at $z = 0.5524$

[O/H]	-0.55
[C/H]	-0.55
[N/H]	-0.2
[Si/H]	-0.25
[O/C]	0.0
[N/C]	0.35
[Si/C]	0.3

6.2 Modifications of the Models

As seen in §6.1, the column densities observed for singly and highly ionized species (O II, C II, Ne VII, Ne VIII), are not in all cases satisfyingly reproduced by the models. In order to assess the impact of these discrepancies, if the observed column densities are correct, modified models are calculated for the systems at $z = 1.8451$ and 0.722 respectively. In addition to the metal abundances and the total hydrogen density, the ionizing field has been allowed to vary in three different ways :

- The whole spectrum is multiplied by a constant factor
- The H I edge is changed by multiplying the flux below 912 \AA by a constant factor.
- The He II edge is changed by multiplying the flux below 228 \AA by a constant factor.

6.2.1 $z = 1.8451$

Since information about all high ionization stages of neon (Ne VI, Ne VII, Ne VIII) is obtained for this redshift from the new data and VR 95 provide the column density for O VI, this system is an appropriate candidate to gain information about modifications required for producing sufficient amounts of highly ionized species.

In the framework of the simple modifications mentioned above, the observed column densities are best reproduced by decreasing the He II edge of the ionizing field by a factor of three (see Figure 8). This reduction of the He II edge agrees rather well with results presented by Songaila & Cowie (1996), who expect $N(\text{HeII})/N(\text{HI}) = 20..40$ for $z < 3$. The modified ionization field provides $N(\text{HeII})/N(\text{HI}) = 25$ in contrast to 45 of the original field. The model also predicts lower He I column densities, which reconciles model and observations.

Both, the low and the high ionization phase, have been calculated as photoionized by this

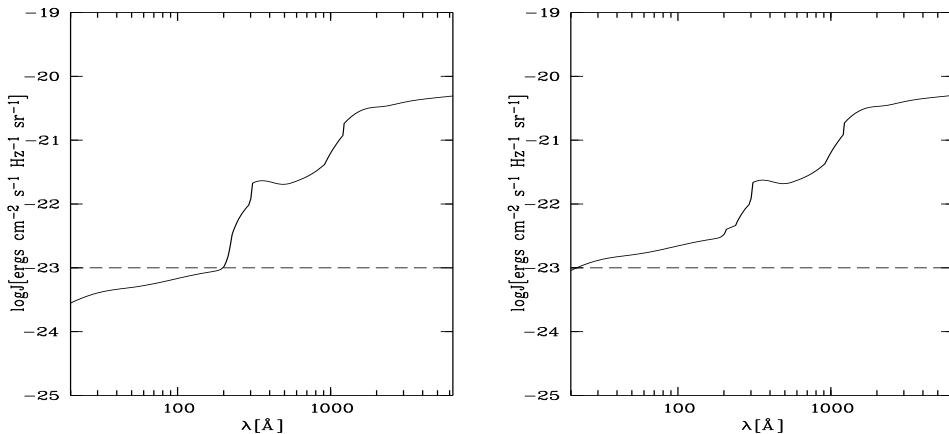


Figure 8: Photoionizing field as computed by Haardt & Madau for $z=1.817$ (left) and modified field (right)

Table 18: Modified two component cloud model for the absorber at $z = 1.8451$ ionized by the radiation field from Haardt & Madau at $z = 1.817$ with a reduced He II edge. Column densities are measured in cm^{-2} , the velocity parameter b is given in km/s and the hydrogen density in cm^{-3} .

ion	observed column density			LIP	HIP
	$b = 30$	$b = 50$	$b = 100$	$\log n_{\text{H}} = -2.4$	$\log n_{\text{H}} = -3.7$
H I	16.75 ^a			16.75	15.1
H II				19.9	19.8
He I	15.0			15.1	12.0
He II				18.15	16.5
O II	13.9	13.9	13.9	13.1	9.4
O III	15.0	14.7	14.5	15.0	12.15
O IV ⁺	14.9	14.7	14.7	14.95	13.65
O V	14.9	14.4	14.4	14.45	14.3
O VI	14.5 ^a			13.7	14.25
C II	≤ 14.3	14.3	14.3	13.35	10.05
C III	14.3 ^{a,*}			14.7	11.95
C IV	14.35 ^c			14.25	12.55
N II				12.2	8.9
N III	13.9	13.9	13.9	13.85	11.4
N IV	13.9	13.8	13.8	13.8	12.4
N V	$< 13.8^a$			13.1	12.6
S II	13.1	13.1	13.1	12.1	-
S III	13.2	13.15	13.15	13.15	8.1
S IV	≤ 13.3	13.3	13.3	13.2	8.95
S V	13.0	13.0	13.0	12.8	9.3
S VI	$< 13.6^a$			12.45	9.45
Ne III	14.6	14.5	14.5	14.55	11.0
Ne IV	14.85 ^b		14.7 ^b	14.75	12.75
Ne V	14.7	14.7	14.7	14.65	14.1
Ne VI	≤ 14.8	14.8	14.8	13.85	14.7
Ne VII	14.25	14.15	14.15	12.2	14.35
Ne VIII	≤ 14.3	14.3	14.3	11.4	14.05
size [kpc]				6.7	100
$\log T$ [K]				$2.5 \cdot 10^4$	$4.8 \cdot 10^4$

⁺ : at least one line of this ion is apparently unblended

^a : value taken from VR 95

^b : value taken from KRW 96

^c : value taken from TLS 97

* : VR 95's spectrum is reconcilable with $\log N = 14.6$ for $z=1.8451$

radiation field. The results are displayed in Table 18.

Except for neon, the metal abundances of the new model do not differ significantly from the values derived in §6.1 (see Table 19). The higher value found for neon, does not come as a surprise, since additional amounts of neon in the form of Ne VII and Ne VIII have to be supplied. The discrepancy between the neon abundance and those of the other elements is even larger in this model and gives rise to further doubts about the column densities observed for Ne VII and Ne VIII. Data of higher resolution in combination with less crowded sightlines are required to firmly resolve this question.

Table 19: Metal abundances for the system at $z = 1.8451$

	original model	modified model
[O/H]	-1.7	-1.5
[C/H]	-1.6	-1.6
[N/H]	-1.8	-1.7
[S/H]	-1.5	-1.55
[Ne/H]	-1.2	-0.85
[O/C]	-0.1	0.1
[N/C]	-0.2	-0.1
[S/C]	0.1	0.05
[Ne/C]	0.4	0.75

6.2.2 $z = 0.722$

As mentioned above, the spectrum reveals strong absorption at the expected position of the O II 834 triplet at this redshift. In combination with a moderately strong feature found for C II 687, this makes the absorber suitable for testing modified ionization fields in order

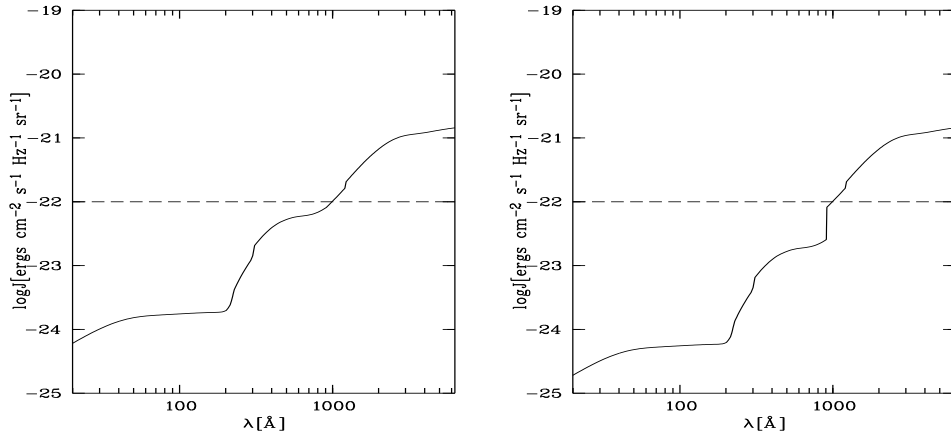


Figure 9: Photoionizing field as computed by Haardt & Madau for $z = 0.6784$ (left) and modified field (right)

to produce adequate amounts of singly ionized oxygen, carbon and possibly sulphur and nitrogen.

The best agreement between observed and calculated column densities has been found by increasing the H I edge of the radiation field from Haardt & Madau at $z = 0.6784$ by a factor of three, resulting in a softer radiation field (see Figure 9).

The results are presented in Table 20 and 21. Except for magnesium, the new model predicts higher metal abundances, which is mainly due to the reduced amount of total matter in both phases as compared with the original cloud model of §6.1.5. The total hydrogen column density there was $\log N_{\text{H}} = 18.8$ and 19.3 for the LIP and HIP respectively

Table 20: Modified two component cloud model for the absorber at $z = 0.722$ ionized by the radiation field from Haardt & Madau at $z = 0.6784$ with an increased H I edge. Column densities are measured in cm^{-2} , the velocity parameter b is given in km/s and the hydrogen density in cm^{-3} .

ion	observed column density				LIP	HIP
	$b = 10$	$b = 25$	$b = 50$	$b = 100$	$\log n_{\text{H}} = -2.8$	$\log n_{\text{H}} = -4.3$
H I		16.3			16.3	15.1
H II					18.4	18.9
He I					15.4	13.25
He II					17.35	16.85
O II	14.8	14.7	14.6	14.5	14.5	12.35
O III ⁺		15.1	14.8	14.7	14.8	14.6
O IV		15.2	14.9	14.8	13.05	15.1
O V					11.75	14.9
O VI		14.6	14.4	14.4	10.3	14.4
C II	14.0	13.9	13.9	13.9	13.85	12.3
C III		14.8	14.1	13.9	14.3	14.25
C IV		14.0 ^a			12.7	14.2
N II	≤ 14.6	≤ 14.4	14.3	14.3	13.55	11.7
N III		14.0	13.9	13.8	13.95	13.9
N IV		14.4	14.1	14.05	12.45	14.2
N V		14.0	14.0	14.0	11.15	13.8
S II	≤ 14.0	≤ 13.4	13.4	13.4	12.85	11.1
S III		13.5	13.5	13.5	13.55	12.85
S IV		≤ 13.7	13.65	13.65	12.4	13.3
S V		13.4	13.3	13.3	10.55	13.3
S VI		≤ 13.7	13.7	13.7	9.3	13.4
Si II	≤ 14.0	≤ 13.6	13.5	13.5	13.1	10.2
Si III ⁺		13.4	13.2	13.2	13.35	11.55
Si IV		$\leq 13.6^a$			12.8	11.8
Mg II	12.78 ^c	$> 12.7^d$			12.7	9.75
size [kpc]					0.5	50
$\log T$ [K]					$1.0 \cdot 10^4$	$2.1 \cdot 10^4$

⁺ : at least one line of this ion is apparently un blended

^a : value taken from VR 95

^c : calculated by TLS 97 for $b=16$ km/s

^d : value taken from PRR 96

compared with 18.4 and 18.9 of Table 20. All elements considered in the form of various ionization stages must be correspondingly more abundant. In the case of magnesium this effect is compensated by the characteristic quality of the new model to produce higher amounts of singly ionized species, whereas a possible depletion of higher ionization stages of Mg is not restricted by any measurements. Apart from magnesium, the modifications do not significantly change the relative heavy element abundances.

Table 21: Metal abundances for the system at $z = 0.722$

	original model	modified model
[O/H]	-0.75	-0.35
[C/H]	-0.95	-0.65
[N/H]	-0.65	-0.3
[S/H]	-0.5	0
[Si/H]	-0.85	-0.5
[Mg/H]	-0.4	-0.45
[O/C]	0.2	0.3
[N/C]	0.3	0.2
[S/C]	0.45	0.65
[Si/C]	0.1	0.15
[Mg/C]	0.55	0.2

6.3 The Absorber Complex at $z = 2.315$

A complicated structure of this metal rich absorption complex is distinguished in high resolution optical data (R-P 95, TLS 97). Apart from oxygen, nitrogen and carbon, strong lines of neon and sulphur are unambiguously detected. In the face of very high metal abundances of $[M/H] \approx -0.45$ derived for this absorber by TLS 97 by calculating a model for the strongest component of this absorption complex, it is worth checking these results for compatibility with the new UV data.

Since the structure of this system is not resolved in the UV data, it is not possible to derive results for the individual components. Therefore, composite column densities must be used for a comparison with the model of TLS 97. The model has been constructed so as to resemble that used by TLS 97 as much as possible. Therefore it also consists of one component assumed as a plane parallel slab illuminated on one side by the same radiation field from Madau (1992). A uniform metallicity of $[M/H] = -0.45$ has been used and the total hydrogen density varies between $-1.0 \leq \log n_H \leq -3.8$. The resulting column densities of numerous ions are plotted in Figure 10. The upper left panel shows the results for those ions observed by TLS 97, including their observed column densities displayed at the right border. Similar plots have been constructed for ions detected in the new UV data. Again observed column densities are presented at the right edge of the panels, where vertical lines at the symbols indicate the range of $\log N$ measured for different velocity parameters. In contrast to 16.6 used by TLS 97, the total neutral hydrogen column density of all components of this absorber, $\log N_{\text{HI}} = 16.88$, has been used in the new model. Column densities of N IV and Ne VII are taken from VR 95 and KRW 96, since the corresponding lines fall outside the range of the new data.

The vertical line at $\log n_H = -1.8$ marks the hydrogen density, at which the best agreement is found for the measured column densities of TLS 97. Lower densities are not compatible with the value for Si II. The model clearly fails to reproduce the column densities observed for the majority of the higher ionization species (N IV, O V, Ne V, Ne VI and Ne VII) in the hydrogen density range compatible with the results of TLS 97. On the other hand, it predicts higher values for N III and O III. The discrepancy for the higher ionization species would be even greater, if the strong oxygen, carbon and nitrogen lines are affected by saturation, as suggested by TLS 97.

Although this discrepancy might to some extent be overcome by using a harder ionization

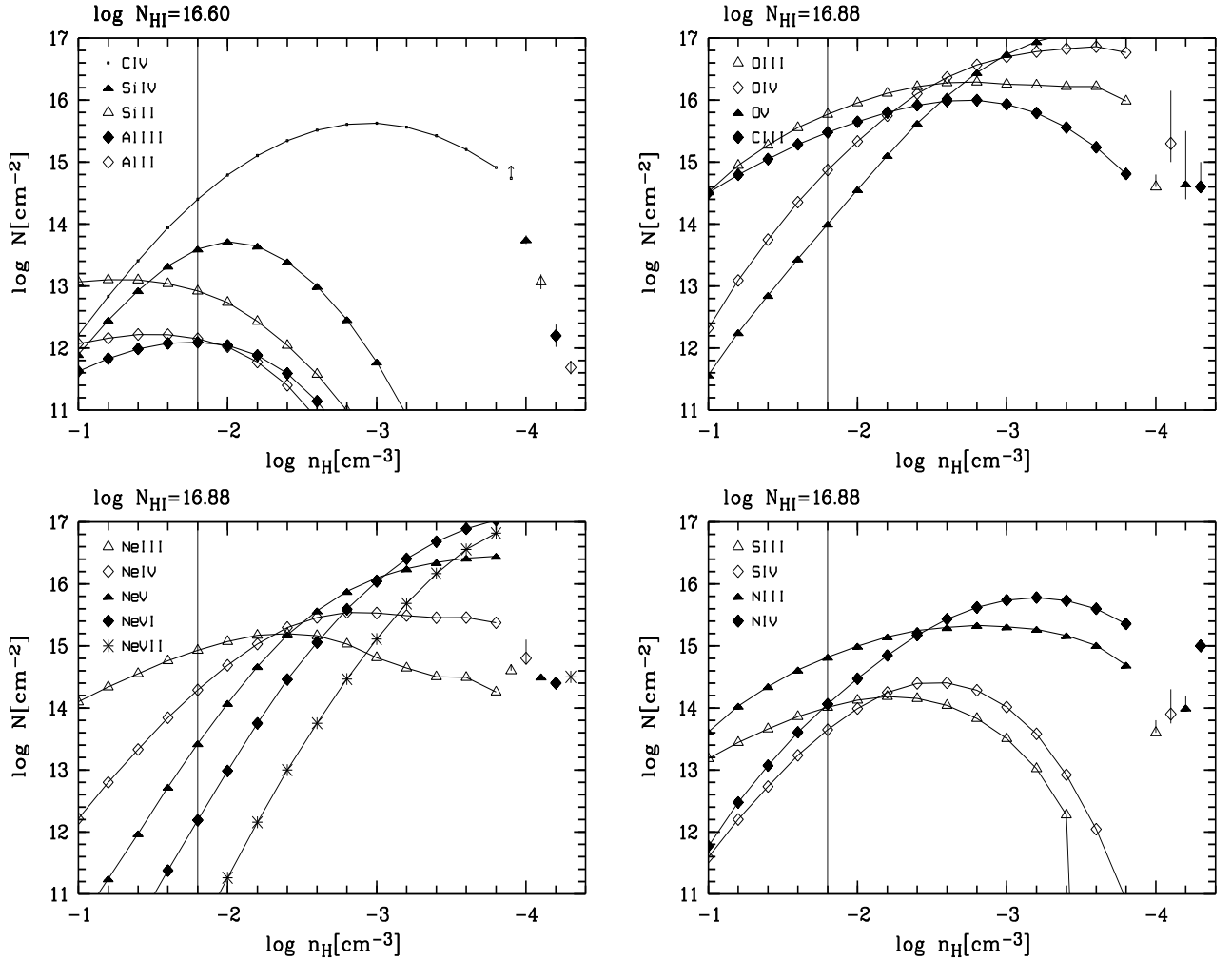


Figure 10: One component cloud models for the absorption complex at $z = 2.315$, ionized by the field from Madau (1992). The column densities of various metals are plotted versus the total hydrogen density. Measured values are displayed at the right edges. The upper left panel shows results of TLS 97 and the corresponding column densities, obtained for the strongest component of the absorber complex, assumed to contain $\log N_{\text{HI}} = 16.6$. The other three panels present results calculated for the whole absorption system ($\log N_{\text{HI}} = 16.88$ in comparison with column densities derived in this work).

field, information from UV data of higher resolution in combination with more sophisticated cloud models are definitely required in order to derive accurate metal abundances for this absorber complex.

In this context, it has to be kept in mind, that a two component cloud model results in systematically lower metal abundances by ≈ 0.3 dex (cf., §6.1.1). However, the prominent absorption by a variety of ions including S III and Ne IV and correspondingly high metal column densities found for this system indicate, that higher metallicities at $z \geq 2$ than

those found for the systems at $z = 2.168$ and 1.8451 in this work cannot be excluded on the basis of the present data.

6.4 Results

The metal abundances derived in §6.1 and §6.2 are summarized in Table 22 and plotted in Figure 11. In spite of the uncertainties of the values, the increase of heavy element abundances with decreasing redshift is obvious, which is in good agreement with previous observations of HS1700 (cf., VR 95 and PRR 96). The investigation of the absorber complex at $z = 2.315$ does not provide accurate metal abundances but leaves open the possibility of higher metallicities at $z \approx 2$.

Except for the absorber at $z = 0.8643$, no significant overabundance of oxygen and nitrogen relative to carbon as compared with solar values is found. According to the models of §6.1, though, silicon, magnesium, sulphur and in particular neon are systematically overabundant with respect to carbon relative to solar. Since the values calculated for oxygen, nitrogen and carbon are generally derived from strong absorption lines, this discrepancy might hint at unresolved saturation of these lines and consequently underestimated column densities for C, N and O thus indicating larger abundances. Unrecognized blending in the case of the silicon, neon and sulphur lines might also provide an explanation and the accuracy of column densities derived for Mg II from optical data seems to be limited as well, as shown by results for the absorber at $z = 0.8643$. TLS 97 derive $\log N_{\text{MgII}} = 12.00 \pm 0.05$, which contradicts $\log N_{\text{MgII}} > 12.28$ reported by PRR 96.

On the other hand, evidence for a silicon overabundance at $z \approx 3$ is found in high resolution optical data. Songaila & Cowie (1996) report $\text{Si/C} \approx 3(\text{Si/C})_{\odot}$, whereas Giroux & Shull derive $\text{Si/C} \approx 2(\text{Si/C})_{\odot}$ using different photoionization models.

Applying a harder ionization field in order to reproduce column densities of highly ionized species (O VI, Ne VII and Ne VIII) leads to no significantly different metal abundances,

Table 22: Metal abundances

z	2.168	1.8451	1.8451 _{mod}	1.1574	0.8643	0.722	0.722 _{mod}	0.5524
[O/H]	-2.15	-1.7	-1.5	-1.2	-0.4	-0.75	-0.35	-0.55
[C/H]	-2.15	-1.6	-1.6	-1.3	-1.2	-0.95	-0.65	-0.55
[N/H]	-2.05	-1.8	-1.7	-1.5	-0.9	-0.65	-0.3	-0.2
[S/H]	-1.7	-1.5	-1.55	-0.9	-0.25	-0.5	0.0	
[Si/H]					-0.7	-0.85	-0.5	-0.25
[Ne/H]	-1.3	-1.2	-0.85	-0.9				
[Mg/H]				-0.6	-0.55	-0.4	-0.45	
[O/C]	0.0	-0.1	0.1	0.1	0.8	0.2	0.3	0
[N/C]	0.1	-0.2	-0.1	-0.2	0.3	0.3	0.35	0.35
[S/C]	0.45	0.1	0.05	0.4	0.95	0.45	0.65	
[Si/C]					0.5	0.1	0.15	0.3
[Ne/C]	0.85	0.4	0.75	0.4				
[Mg/C]				0.7	0.65	0.55	0.2	

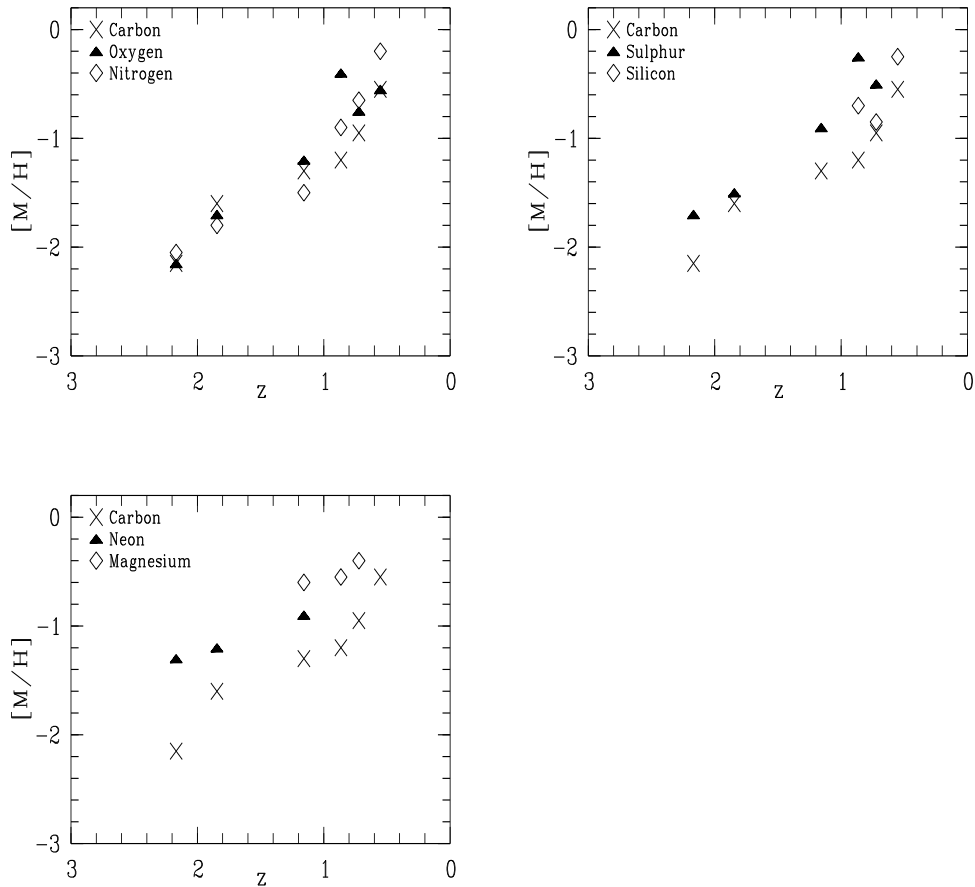


Figure 11: Evolution of metal abundances with decreasing redshift. The results from the modified models are not plotted, but they differ only slightly from values obtained from the original models. For $z = 1.8451$ a slightly larger neon abundance is found. For the absorber at $z = 0.722$, slightly larger values, comparable to those of the system at $z = 0.5524$ are found for all elements, apart from magnesium.

apart from neon, for which a slightly higher value is found. If the high column densities of singly ionized species observed for the system at $z = 0.722$ are true, an increase of the hydrogen decrement of the radiation field is required, shifting the heavy element abundances toward slightly larger values, comparable to those found for the absorber at $z = 0.5524$. The relative metal abundances are, however, not significantly affected, except for magnesium, for which no change in the absolute abundance is predicted by the modified model.

7 Conclusions

New ultraviolet spectra of HS1700+6416 obtained with the GHRS and FOS onboard the Hubble Space Telescope provide an improved data base for the investigation of intervening absorbers with particular regard to absorption by neon and sulphur and systems at lower redshifts. The analysis has been substantially helped by recently published high resolution optical data.

Among various heavy element lines, absorption by S III-S V and Ne III-Ne VII is found, confirming results of Köhler et al. (1996).

The new data suggest the existence of a new metal line system at $z \approx 0.09$, rising the total number of MLSs and MLS candidates to 21. Systems at $z = 2.37995$, 2.7125 and 2.7444 identified in optical data have been investigated in UV spectral ranges down to 1150 \AA for the first time, but no unambiguous identification of heavy element absorption at either redshift is found.

Cloud models with two components of different density but identical metallicities photoionized by a metagalactic radiation field as computed by Haardt & Madau (1996) have been constructed in order to derive metal abundances for 6 MLS. In some cases, though, these models fail to reproduce measured column densities of singly and highly ionized heavy elements (O II, C II, O VI, Ne VII, Ne VIII) and predict an excess of He I. A harder radiation field obtained by decreasing the He II edge by a factor of 3 produces adequate amounts of highly ionized species and resolves the discrepancy observed for He I. This modification has no significant effect on the metal abundances, apart from neon, for which a slightly larger value is obtained, and it is also in good agreement with $N(\text{HeII})/N(\text{HI}) = 20..40$ expected for $z < 3$ by Songaila & Cowie (1996). Discrepancies between measured and calculated column densities of singly ionized species found for the MLS at $z = 0.722$ can be removed by increasing the H I edge of the photoionizing field by a factor of three, which results in slightly larger heavy element abundances, comparable to those found for the system at $z = 0.5524$. The relative metal abundances, though, are not significantly affected by this modification, except for magnesium, for which no increase in abundance is predicted by the modified model.

Except for the system at $z = 0.8643$, no significant [O/C] or [N/C] overabundance is found, but the models predict enrichment relative to solar of magnesium, silicon, sulphur and in particular neon. In metal poor stars, overabundance of these elements as well as oxygen is found (e.g. Gehren 1988 reports values for [O/Fe], [Mg/Fe], [Si/Fe] and [S/Fe] scattering about 0.5). If the gas clouds considered here do form the progenitors of Pop.II stars, oxygen enrichment would also be expected.

However, unresolved saturation of the strong C, N and O lines, which leads to an underestimation of the column densities and, consequently, of the carbon, nitrogen and oxygen abundances, and/or unrecognized blending of silicon, sulphur and neon lines might result in artificial overabundances of these elements. The reliability of column densities for Mg II derived from optical data is questioned by contradictory results for Mg II at $z = 0.8643$ reported by Tripp et al. (1997) and Petitjean et al. (1996). As far as silicon is concerned, though, evidence for marginal overabundances is derived from optical data for $z \approx 3$. Songaila & Cowie (1996) and Giroux & Shull find $\text{Si/C} \approx 3(\text{Si/C})_{\odot}$ and $2(\text{Si/C})_{\odot}$ respectively.

Differences to [O/C] and [N/C] values derived from previous UV data analyses can be attributed to more reliable redshifts and velocity parameters obtained from high quality optical data and the improved S/N of the new UV data. The introduction of additional

matter in the form of a high ionization phase, as compared with one component models used by Vogel & Reimers (1995) results in lower metallicities by ≈ 0.3 dex.

In general metal abundances are found to increase with decreasing redshift with $[M/H] \approx -2$ at $z \approx 2$, $[M/H] \approx -1$ at $z \approx 1$ and values slightly below solar at $z \approx 0.5$, which agrees well with the results from Petitjean et al. (1996).

A one component model calculated for the complex absorption system at $z = 2.315$ for comparison purposes with respect to high metallicities of this system reported by Tripp et al. (1997) fails to reproduce the wide variety of different ionization stages. Considering the model dependancy of heavy element abundances, information from UV data of higher resolution in combination with more sophisticated cloud models are required in order to derive accurate metal abundances for this absorber complex. However, the prominent absorption by a variety of ions including S III and Ne IV and correspondingly high metal column densities found for this system leave open the possibility of higher metallicities at $z \approx 2$ than those found for the systems at $z = 2.168$ and 1.8451 .

Several assumptions forming the basis of the photoionization models, calculated in this work are still a matter of discussion. Results from Rauch et al. (1997) suggest, that shock heating might lead to higher temperatures than expected in photoionization equilibrium. Even if photoionization plays the dominant role, the origin of the ionizing field remains uncertain. Apart from the QSO background, local sources and/or hot massive stars might substantially contribute to the radiation field. The integrated flux of the quasar background strongly depends on the QSO luminosity function and the intrinsic QSO flux energy distribution. Finally, different metallicities in the LIP and HIP cannot be excluded but would lead to too many free parameters in the models.

In addition to these uncertainties, the low resolution of the data in combination with the high line density imposes limitations upon the data analysis. These problems might to a certain extent be overcome, when brighter quasars at lower redshift are observed with the Space Telescope Imaging Spectrograph. Such observations are particularly important, since UV data are the only gateway to information about neon and sulphur abundances, absorption systems at lower redshifts and a sufficiently wide variety of different ionization stages to provide adequate constraints upon the cloud models.

Comparison of UV data with predictions from hydrodynamical simulations of galaxy formation (e.g. Rauch et al. 1997) might provide an alternative way to derive information about the physical and chemical properties of QSO absorption systems.

8 References

- Bergeron, J., Petitjean, P., Sargent, W. L. W. et al., 1994, *ApJ*, 436, 33
- Ferland, G. J. 1993, University of Kentucky Department of Physics and Astronomy Internal Report
- Gehren, T. 1988, *Reviews in Mod. Astr.* 1, 52
- Giroux, M. L., & Shull, J. M. 1997, *AJ*, 113(5), 1505
- Grevesse, N., & Anders, E. 1989, in *Cosmic abundances of matter*, AIP conference proceedings 183, ed. C. J. Waddington
- Haardt, F., & Madau, P. 1996, *ApJ*, 461, 20
- Jenkins, E. B. 1986, *ApJ*, 304, 739
- Köhler, S., Reimers, D., & Wamsteker, W., 1996, *A&A*, 312, 33
- Lanzetta, K. M., & Bowen, D. V. 1992, *ApJ*, 391, 48
- Leitherer C., & Kinney, A., 1994, *GHRS Instrument Science Report* 66
- Lockman, F. J., & Savage, B. D. 1995, *ApJS*, 91, 1
- Madau, P. 1992, *ApJ*, 389, L1
- Nath, B. B., & Biermann, P. L. 1993, *MNRAS*, 265, 241
- Petitjean, P., Bergeron, J., & Puget, J.-L. 1992, *A&A*, 265, 375
- Petitjean, P., Riediger, R., & Rauch, M. 1996, *A&A*, 307, 417
- Press, W. H., Flannery B. P., Teukolsky S. A., & Vetterling, W. T. 1986, *Numerical Recipes*, Cambridge University Press
- Rauch, M., Haehnelt, M. G., & Steinmetz, M. 1997, *ApJ*, 481 in press
- Reimers, D., Clavel, J., Groote, D., Engels, D., Hagen, H.-J., Naylor, T., Wamsteker, W., & Hopp, U. 1989, *Astron. Astrophys.* 218, 71
- Reimers, D., Vogel, S., Hagen, H.-J., Engels, D., Groote, D., Wamsteker, W., Clavel, J., & Rosa, M. R. 1992, *Nature*, 360, 561
- Reimers, D., Bade, N., & Schartel, N. et al., 1995, *A&A*, 296, L49
- Rodríguez-Pascual, P. M., de al Fuente, A., Sanz, J. L., Recondo, M. C., Clavel, J., Santos-Lleó, M., & Wamsteker, W. 1995, *ApJ*, 448, 575
- Savage, B. D., & Sembach, K. R. 1991, *ApJ*, 379, 245
- Schneider, D. P., Hartig, G. F., Jannuzi, B. T. et al. 1993, *ApJS* 87, 45
- Songaila, A., & Cowie, L. L. 1996, *AJ*, 112, 335
- Steidel, C. C. 1990, *ApJS*, 74, 37

Sutherland, R. S., & Dopita, M. A. 1993, ApJS, 88, 253

Tegmark, M., Silk, J., & Evrard, A. 1993, ApJ, 417, 54

Tripp, T. M., Lu, L., & Savage, B. D. 1997, ApJS, accepted

Unsöld, A. 1955, Physik der Sternatmosphären, Springer Verlag Berlin

Verner, D. A., Barthel, P. D., & Tytler, D. 1994, A&AS, 108, 287

Vogel, S., & Reimers, D. 1995, A&A, 294, 377

A Atomic Parameters

According to Unsöld (1955), the optical depth caused by a specific transition is

$$\tau = \frac{2\pi^{3/2}e^2}{mc} \cdot \frac{Nf}{\Delta\omega_D} \cdot H(\alpha, v)$$

with

$$\begin{aligned}\alpha &= \frac{\gamma}{2\Delta\omega_D} \\ v &= \frac{\omega - \omega_0}{\Delta\omega_D} \\ \Delta\omega_D &= \frac{\omega}{c}b\end{aligned}$$

where N is the column density of the ion, f the oscillator strength of the transition, $H(\alpha, v)$ the Voigt function, γ the damping constant and b the Doppler parameter. Atomic parameters used throughout this work are taken from the list given by VR 95 (see their paper and references therein), extended on the basis of parameters taken from Verner et al. (1994).

Table 23: Atomic Parameters

ion	λ_{vac} [Å]	f	γ	ion	λ_{vac} [Å]	f	γ
H I	1215.6701	0.416200	6.2650e+08	H I	912.3530	0.000026	7.0000e+04
H I	1025.7223	0.079100	1.8970e+08	H I	912.3240	0.000024	6.5000e+04
H I	972.5368	0.028990	8.1260e+07	C II	1334.5323	0.127800	2.8700e+08
H I	949.7430	0.013940	4.2030e+07	C II	1036.3367	0.123100	2.2900e+09
H I	937.8035	0.007800	2.4500e+07	C II	903.9616	0.336000	4.1000e+09
H I	930.7483	0.004814	1.2000e+07	C II	903.6235	0.168000	4.1900e+09
H I	926.2257	0.003183	8.2000e+06	C II	687.0526	0.336000	2.2000e+09
H I	923.1504	0.002216	5.8000e+06	C II	594.8000	0.117000	1.1029e+09
H I	920.9631	0.001605	4.2000e+06	C II	560.2393	0.057100	6.0671e+08
H I	919.3610	0.001201	3.1000e+06	C II	543.2570	0.034900	3.9438e+08
H I	918.1290	0.000921	2.4000e+06	C II	530.2740	0.036200	4.2934e+08
H I	917.1810	0.000723	1.9000e+06	C III	977.0200	0.768000	1.7750e+09
H I	916.4290	0.000577	1.5000e+06	C III	386.2028	0.232000	3.8000e+09
H I	915.8240	0.000469	1.2000e+06	C III	322.5741	0.045200	9.6600e+08
H I	915.3290	0.000385	1.0000e+06	C IV	1550.7700	0.095220	2.6410e+08
H I	914.9190	0.000321	8.5000e+05	C IV	1548.1949	0.190800	2.6450e+08
H I	914.5760	0.000270	7.1000e+05	O II	834.4655	0.132000	1.3000e+09
H I	914.2860	0.000230	6.0700e+05	O II	833.3294	0.088600	1.4000e+09
H I	914.0390	0.000197	5.2000e+05	O II	832.7572	0.044400	8.5400e+08
H I	913.8260	0.000170	4.5000e+05	O II	539.0855	0.065200	8.6000e+08
H I	913.6410	0.000148	3.9000e+05	O II	539.5489	0.043500	8.6000e+08
H I	913.4800	0.000128	3.3800e+05	O II	539.8544	0.021700	8.6000e+08
H I	913.3390	0.000114	3.0000e+05	O II	430.1770	0.186000	3.9000e+09
H I	913.2150	0.000101	2.6600e+05	O II	430.0410	0.124000	3.9000e+09
H I	913.1040	0.000089	2.3700e+05	O II	429.9180	0.061800	4.4600e+09
H I	913.0060	0.000080	2.1100e+05	O II	392.0020	0.082100	2.3800e+09
H I	912.9180	0.000071	1.8900e+05	O II	391.9430	0.054800	2.3800e+09
H I	912.8390	0.000064	1.7000e+05	O II	391.9120	0.027300	2.3700e+09
H I	912.7680	0.000058	1.5400e+05	O II	376.7450	0.043600	1.3700e+09
H I	912.7030	0.000053	1.4000e+05	O II	376.6930	0.029000	1.3600e+09
H I	912.6450	0.000048	1.2700e+05	O III	832.9270	0.107000	8.4300e+08
H I	912.5920	0.000044	1.1600e+05	O III	702.3320	0.137000	6.1800e+08
H I	912.5430	0.000040	1.0600e+05	O III	507.3910	0.185000	1.5900e+09
H I	912.4990	0.000037	9.7000e+04	O III	374.0050	0.083100	2.9000e+09
H I	912.4580	0.000034	8.9000e+04	O IV	787.7110	0.111000	6.0000e+08
H I	912.4200	0.000031	8.2000e+04	O IV	608.3980	0.067000	5.0000e+09
H I	912.3850	0.000029	7.6000e+04	O IV	554.0750	0.224000	8.3000e+09

Table 23 continued

ion	λ_{vac} [Å]	f	γ	ion	λ_{vac} [Å]	f	γ
O IV	553.3300	0.112000	8.2000e+09	Si II	1190.4158	0.250200	3.5030e+09
O V	629.7300	0.514000	3.0000e+09	Si II	989.8670	0.200000	7.8700e+08
O VI	1037.6167	0.066090	4.0950e+08	Si III	1206.5000	1.680000	2.5500e+09
O VI	1031.9261	0.132900	4.1630e+08	Si IV	1402.7700	0.260000	8.6560e+08
N I	1199.5496	0.163000	5.5000e+08	Si IV	1393.7550	0.524000	8.8250e+08
N I	1200.2233	0.108000	5.3000e+08	S II	1259.5179	0.015500	4.4568e+07
N I	1200.7098	0.054100	5.5000e+08	S II	1253.8051	0.010300	4.3702e+07
N II	1083.9937	0.109000	3.5080e+08	S II	1250.5780	0.005200	4.4354e+07
N II	915.6131	0.160000	1.1510e+09	S II	912.7350	0.062000	9.9300e+08
N II	671.4102	0.076600	1.3200e+09	S II	910.4840	0.124000	9.9800e+08
N II	644.6337	0.224000	1.1100e+10	S II	906.8850	0.187000	1.0000e+09
N II	533.5099	0.299000	3.6920e+09	S II	765.6930	1.190000	9.0255e+09
N II	529.3572	0.103000	8.1723e+08	S II	764.4200	0.795000	9.0750e+09
N II	475.6481	0.119000	1.1694e+09	S II	763.6570	0.398000	9.1000e+09
N II	474.4909	0.043600	4.3100e+08	S II	641.7670	0.260000	2.8070e+09
N II	453.2370	0.062500	6.7600e+08	S II	640.9020	0.174000	2.8300e+09
N II	452.6390	0.022200	2.4090e+08	S II	640.4120	0.086800	2.8200e+09
N II	442.0520	0.046100	5.2500e+08	S II	594.4750	0.082800	1.0400e+09
N II	441.5990	0.013600	1.5500e+08	S II	593.8350	0.055200	1.0400e+09
N III	989.7990	0.122000	4.3520e+08	S II	593.5070	0.027600	1.0500e+09
N III	763.3400	0.082000	3.8000e+09	S II	571.7790	0.036000	4.9000e+08
N III	685.5130	0.268000	6.5000e+09	S II	571.3640	0.024100	4.9200e+08
N III	684.9960	0.135000	6.4000e+09	S II	571.1560	0.012000	4.9100e+08
N III	451.8690	0.031600	4.5000e+09	S III	1190.2080	0.022170	6.2320e+07
N III	374.2040	0.441000	9.4000e+09	S III	1012.5020	0.035500	2.2810e+08
N III	323.4930	0.034800	2.2200e+09	S III	724.2890	0.352000	1.4918e+09
N III	323.4360	0.017300	5.5200e+08	S III	698.7300	0.783000	3.5657e+09
N III	314.7150	0.194000	6.5322e+09	S III	681.4700	0.068300	3.2700e+08
N IV	765.1480	0.616000	2.4000e+09	S III	677.7460	1.640000	7.9381e+09
N V	1242.8040	0.078000	3.3780e+08	S III	484.1720	0.057800	5.4800e+08
N V	1238.8210	0.157000	3.4110e+08	S IV	1062.6620	0.039990	1.4100e+08
Si II	1808.0126	0.002180	6.7490e+06	S IV	809.6680	0.104000	1.0581e+09
Si II	1526.7065	0.116000	1.9600e+09	S IV	748.4000	0.500000	8.8000e+09
Si II	1304.3702	0.094000	1.7200e+09	S IV	744.9200	0.251000	2.2000e+09
Si II	1260.4221	1.180000	2.5330e+09	S IV	657.3400	1.180000	2.0000e+08
Si II	1193.2897	0.584000	3.4950e+09	S IV	551.1700	0.086900	6.1000e+09

Table 23 continued

ion	λ_{vac} [Å]	f	γ
S v	786.4800	1.460000	5.2500e+09
S vi	944.5230	0.218100	1.6310e+09
S vi	933.3780	0.441400	1.6900e+09
Al II	1670.7874	1.833000	1.4600e+09
Al III	1862.7896	0.286000	5.3610e+08
Al III	1854.7164	0.575000	5.4320e+08
He I	584.3340	0.276200	1.8010e+09
He I	537.0300	0.073400	5.7960e+08
He I	522.2130	0.030200	2.5500e+08
He I	515.6155	0.015400	1.2800e+08
He I	512.0982	0.008830	7.1900e+07
He I	509.9979	0.005530	5.0700e+07
He I	508.6431	0.003690	3.4300e+07
He I	507.7178	0.002590	2.3700e+07
He I	507.0576	0.001880	1.8100e+07
Ne III	489.5050	0.131000	6.9000e+09
Ne III	488.1080	0.043800	7.1000e+09
Ne IV	543.8910	0.116000	2.5000e+09
Ne IV	542.0730	0.077900	2.5000e+09
Ne IV	541.1270	0.039000	2.5000e+09
Ne v	568.4200	0.092800	1.3500e+09
Ne v	480.4100	0.110000	8.0000e+09
Ne v	357.9500	0.139000	2.1800e+10
Ne vi	558.5900	0.090700	1.7800e+09
Ne vi	433.1760	0.050500	3.3000e+09
Ne vi	401.1400	0.168000	1.0300e+10
Ne vi	399.8200	0.084400	1.0300e+10
Ne vii	465.2210	0.389000	5.8000e+09
Ne viii	780.3240	0.050500	5.5000e+08
Ne viii	770.4090	0.103000	5.7200e+08

B Line Identifications

All absorption features detected above 3.5σ are listed together with line identifications located less than 0.637 FWHM (i.e. 1.5σ) from the center of the gaussian. If the measured FWHM is smaller than that of the instrumental SSF, 1.44 \AA , the maximum distance has been replaced by $0.637 \cdot 1.44 \text{ \AA}$.

Table 24: Absorption Lines associated with 3.5σ Features

λ_{obs}	σ_λ	FWHM	EW	σ_{EW}	ID	z	λ_{exp}	$\lambda_{exp} - \lambda_{obs}$
1165.12	0.34	1.9	0.61	0.08	O II 539.8	1.1574	1164.68	-0.44
1167.35	0.26	1.5	0.60	0.08	S III 677	0.722	1167.08	-0.27
					Ne IV 541	1.1574	1167.43	0.08
1171.93	0.23	1.4	0.36	0.07	O II 429	1.725	1171.53	-0.40
					O II 430.0	1.725	1171.86	-0.07
					O II 430.1	1.725	1172.23	0.30
1174.21	0.07	1.5	1.28	0.07	Ne IV 543	1.1574	1173.39	-0.82
					O V 629	0.8643	1174.01	-0.20
1179.12	0.44	1.3	0.25	0.06	N III 684	0.722	1179.56	0.44
1180.64	0.20	1.2	0.50	0.06	N III 685	0.722	1180.45	-0.19
					Ly γ	0.214	1180.66	0.02
1183.50	0.18	1.2	0.31	0.06	C II 687	0.722	1183.10	-0.40
					Ne V 357	2.308	1184.10	0.60
1187.23	0.20	4.0	1.80	0.05	N III 374	2.168	1185.48	-1.75
					S II 763	0.5524	1185.50	-1.73
					C III 977	0.214	1186.10	-1.13
					Ne V 357	2.315	1186.60	-0.63
					S II 764	0.5524	1186.69	-0.54
					N IV 765	0.5524	1187.82	0.59
					S II 765	0.5524	1188.66	1.43
1190.31	0.07	1.0	0.57	0.05	Si II 1190	0.0	1190.42	0.11
1193.33	0.05	1.8	1.61	0.05	O III 374	2.189	1192.70	-0.63
					Si II 1193	0.0	1193.29	-0.04
					N III 374	2.189	1193.34	0.01
					O II 376.6	2.168	1193.36	0.03
					O II 376.7	2.168	1193.53	0.20
					O IV 553	1.1574	1193.75	0.42
1195.44	0.04	0.6	0.38	0.05	O IV 554	1.1574	1195.36	-0.08
1196.31	0.09	0.6	0.20	0.05				
1200.16	0.08	2.5	1.54	0.05	N I 1199	0.0	1199.55	-0.61
					N I 1200.2	0.0	1200.22	0.06

Table 24 continued

λ_{obs}	σ_λ	FWHM	EW	σ_{EW}	ID	z	λ_{exp}	$\lambda_{exp} - \lambda_{obs}$
					N I 1200.7	0.0	1200.72	0.56
					O II 376.6	2.189	1201.27	1.11
1203.31	0.16	1.3	0.28	0.05	O III 507	1.371	1203.02	-0.29
					S III 698	0.722	1203.21	-0.10
1206.18	0.06	1.6	1.04	0.04	Si III 1206	0.0	1206.50	0.32
1209.45	0.10	1.2	0.40	0.04	O III 702	0.722	1209.42	-0.03
1220.43	0.13	2.0	0.58	0.04	S V 786	0.5524	1220.93	0.50
1223.29	0.07	1.4	0.64	0.04	O IV 787	0.5524	1222.84	-0.45
					O II 429	1.8451	1223.16	-0.13
					C III 386	2.168	1223.49	0.20
					O II 430.0	1.8451	1223.51	0.22
					O II 430.1	1.8451	1223.90	0.61
1225.93	0.07	1.5	0.68	0.04	S IV 657	0.8643	1225.48	-0.45
					Ne V 568	1.1574	1226.31	0.38
1229.29	0.11	0.8	0.16	0.04	Ne V 357	2.433	1228.84	-0.45
1231.90	0.23	1.9	0.28	0.03	Ne V 357	2.439	1230.99	-0.91
					N III 374	2.290	1231.13	-0.77
					C III 386	2.189	1231.60	-0.30
					Ne VI 433	1.8451	1232.43	0.53
1235.58	0.05	0.8	0.37	0.03				
1236.73	0.11	0.8	0.18	0.03				
1240.29	0.05	1.5	0.76	0.03	O III 374	2.315	1239.83	-0.46
					N III 374	2.315	1240.49	0.20
1245.34	0.04	1.5	0.94	0.03	Ly β	0.214	1245.23	-0.11
1249.28	0.09	0.9	0.23	0.03	O II 376.7	2.315	1248.91	-0.37
1250.83	0.10	0.9	0.20	0.03	S II 1250	0.0	1250.58	-0.25
1252.74	0.09	1.0	0.28	0.03	O VI 1031	0.214	1252.76	0.02
1253.95	0.06	0.7	0.22	0.03	S II 1253	0.0	1253.81	-0.14
1257.66	0.15	1.5	0.27	0.03	C II 1036	0.214	1258.11	0.45
1260.22	0.03	1.8	1.68	0.03	S II 1259	0.0	1259.52	-0.70
					O VI 1037	0.214	1259.67	0.45
					Si II 1260	0.0	1260.42	0.20
					He I 584	1.1574	1260.64	0.42
1263.70	0.10	2.1	0.86	0.03	S III 677	0.8643	1263.52	-0.18
					O III 374	2.38	1264.14	0.42
					N III 374	2.38	1264.81	1.09
					N II 533	1.371	1264.95	1.25
1266.92	0.31	1.6	0.25	0.03	Ne VI 399	2.168	1266.63	-0.29
					He I 512	1.4735	1266.67	-0.25
1267.77	0.11	0.9	0.20	0.03	Ne VII 465	1.725	1267.73	-0.04
1268.55	0.07	0.6	0.17	0.03				
1269.72	0.04	0.8	0.40	0.03				
1271.00	0.08	0.8	0.23	0.03	C III 386	2.290	1270.61	-0.39

Table 24 continued

λ_{obs}	σ_λ	FWHM	EW	σ_{EW}	ID	z	λ_{exp}	$\lambda_{exp} - \lambda_{obs}$
					Ne VI 401	2.168	1270.81	-0.19
1277.50	0.15	1.1	0.21	0.03	N III 684	0.8643	1277.04	-0.46
					C III 386	2.308	1277.56	0.06
					N III 685	0.8643	1278.00	0.50
1278.55	0.06	0.6	0.21	0.03				
1280.70	0.04	1.3	0.84	0.03	C III 386	2.315	1280.26	-0.44
					C II 687	0.8643	1280.87	0.17
					Ne V 357	2.579	1281.10	0.40
1283.53	0.09	2.3	0.92	0.03	S IV 744	0.722	1282.75	-0.78
					Ne IV 541	1.371	1283.01	-0.52
					C II 594	1.1574	1283.22	-0.31
					O III 374	2.433	1283.96	0.43
					N III 374	2.433	1284.64	1.11
1286.14	0.14	1.4	0.30	0.03	O III 374	2.439	1286.20	0.06
1288.68	0.15	0.7	0.12	0.03	S IV 748	0.722	1288.74	0.06
1289.90	0.08	1.1	0.53	0.03	O II 391.94	2.290	1289.49	-0.41
					Ne IV 543	1.371	1289.57	-0.33
					O II 392	2.290	1289.69	-0.21
1291.14	0.15	1.0	0.27	0.03				
1293.16	0.12	2.2	0.77	0.03	O II 832	0.5524	1292.77	-0.39
					O III 832	0.5524	1293.04	-0.12
					O II 376.6	2.433	1293.19	0.03
					O II 376.7	2.433	1293.37	0.21
					O II 833	0.5524	1293.66	0.50
1309.65	0.03	1.4	0.97	0.03	Ne V 480	1.725	1309.12	-0.53
					O III 702	0.8643	1309.36	-0.29
1312.41	0.05	1.2	0.89	0.03	O IV 553	1.371	1311.95	-0.46
					O IV 608	1.1574	1312.56	0.15
1314.10	0.06	1.6	1.19	0.03	O IV 554	1.371	1313.71	-0.39
					N III 763	0.722	1314.47	0.37
1316.67	0.08	0.6	0.15	0.03				
1317.65	0.05	0.9	0.44	0.03	N IV 765	0.722	1317.58	-0.07
1318.83	0.06	0.5	0.11	0.03	S II 765	0.722	1318.52	-0.31
1325.31	0.04	2.9	2.14	0.03	Ne VII 465	1.8451	1323.60	-1.71
					Ne VI 558	1.371	1324.42	-0.89
					Ly α	0.09	1325.08	-0.23
					Ne VI 399	2.315	1325.40	0.09
					C III 386	2.433	1325.83	0.52
					Ne VIII 770	0.722	1326.64	1.33
					Ne VI 401	2.308	1326.97	1.66
1328.54	0.09	0.9	0.22	0.03	C III 386	2.439	1328.15	-0.39
					He I 537	1.4735	1328.34	-0.20
					Ne V 357	2.7125	1328.89	0.35

Table 24 continued

λ_{obs}	σ_λ	FWHM	EW	σ_{EW}	ID	z	λ_{exp}	$\lambda_{exp} - \lambda_{obs}$
1330.16	0.09	1.3	0.41	0.03	Ne VI 401	2.315	1329.79	0.37
					Ne III 488	1.725	1330.09	-0.07
1334.25	0.04	1.3	1.15	0.03	O II 539.0	1.4735	1333.43	-0.82
					Ne III 489	1.725	1333.90	-0.35
					C II 1334	0.0	1334.53	0.28
					O II 539.5	1.4735	1334.57	0.32
1335.64	0.10	1.0	0.29	0.03	O II 539.8	1.4735	1335.33	-0.31
					C II* 1335	0.0	1335.71	0.07
1338.21	0.22	2.4	0.43	0.03	O III 374	2.579	1338.56	0.35
1339.88	0.18	1.6	0.29	0.03	N III 374	2.579	1339.28	-0.60
1342.05	0.12	0.8	0.12	0.03				
1343.89	0.11	1.4	0.32	0.03	Ne VIII 780	0.722	1343.72	-0.17
1345.85	0.07	0.9	0.26	0.03	O II 391.91	2.433	1345.43	-0.42
					O II 391.94	2.433	1345.54	-0.31
					O II 392	2.433	1345.74	-0.11
1347.44	0.10	1.0	0.24	0.03	Ne V 568	1.371	1347.72	0.28
					O II 391.91	2.439	1347.79	0.35
					O II 391.94	2.439	1347.88	0.44
1349.98	0.10	2.8	1.07	0.03	O II 376.7	2.579	1348.37	-1.61
					N V 1238	0.09	1350.31	0.33
1352.05	0.10	0.6	0.13	0.03				
1353.41	0.34	1.5	0.49	0.03				
1354.73	0.33	1.1	0.25	0.03	S V 786	0.722	1354.32	-0.41
					N V 1242	0.09	1354.66	-0.07
1356.59	0.08	1.7	0.83	0.03	O IV 787	0.722	1356.44	-0.15
1358.64	0.03	1.0	0.76	0.03	O V 629	1.1574	1358.58	-0.06
1359.84	0.08	0.7	0.17	0.03				
1360.65	0.10	0.8	0.16	0.03				
1362.70	0.14	2.0	0.52	0.03	O II 429	2.168	1361.98	-0.72
					O II 430.0	2.168	1362.37	-0.33
					O II 430.1	2.168	1362.80	0.10
1365.43	0.66	2.2	0.52	0.03				
1366.68	0.05	0.9	0.51	0.03	Ne III 480	1.8451	1366.81	0.13
1367.93	0.06	1.1	0.54	0.03				
1370.18	0.20	3.2	1.06	0.03	O IV 553	1.4735	1368.66	-1.52
					O IV 554	1.4735	1370.50	0.32
					O II 429	2.189	1371.01	0.83
					O II 430.0	2.189	1371.40	1.22
					O II 430.1	2.189	1371.83	1.65
1372.88	0.35	1.1	0.24	0.03	Ne VI 433	2.168	1372.30	-0.58
					Ne VI 399	2.433	1372.58	-0.30
1374.21	0.31	1.3	0.29	0.03	Si II 1260	0.09	1373.86	-0.35
					Ne VI 399	2.439	1374.98	0.77

Table 24 continued

λ_{obs}	σ_λ	FWHM	EW	σ_{EW}	ID	z	λ_{exp}	$\lambda_{exp} - \lambda_{obs}$
1376.01	0.16	1.1	0.22	0.03				
1379.04	0.17	3.9	1.40	0.03	Ne VI 401	2.433	1377.11	-1.92
					Ne VI 401	2.439	1379.52	0.48
1382.27	0.07	1.6	0.74	0.03	C III 386	2.579	1382.22	-0.05
					O III 507	1.725	1382.64	0.37
1385.77	0.12	2.0	0.58	0.03	He I 584	1.371	1385.46	-0.31
1389.02	0.07	2.0	0.88	0.03	O III 374	2.7125	1388.49	-0.53
					Ne III 488	1.8451	1388.72	-0.30
					S IV 744	0.8643	1388.75	-0.27
					N III 374	2.7125	1389.23	0.21
1391.74	0.18	1.0	0.17	0.03				
1393.51	0.10	1.8	0.76	0.03	Ne III 489	1.8451	1392.69	-0.82
					Si IV 1393	0.0	1393.76	0.25
1395.46	0.06	0.9	0.38	0.03	S IV 748	0.8643	1395.24	-0.22
					He I 512	1.725	1395.47	0.01
1398.70	0.14	1.4	0.31	0.04	O II 376.6	2.7125	1398.47	-0.23
					O II 376.7	2.7125	1398.67	-0.03
1400.43	0.18	1.2	0.18	0.04				
1402.42	0.17	1.3	0.31	0.04	O II 391.91	2.579	1402.65	0.23
					O II 391.94	2.579	1402.76	0.34
					Si IV 1402	0.0	1402.77	0.35
					C II 903.6	0.5524	1402.79	0.37
					O II 392	2.579	1402.98	0.56
1404.70	0.12	2.2	0.92	0.04	C II 903.9	0.5524	1403.31	-1.39
					He I 515	1.725	1405.05	0.35
1409.93	0.14	1.8	0.47	0.04	C II 594	1.371	1410.27	0.34
1411.99	0.21	1.4	0.23	0.04				
1414.10	0.12	1.5	0.45	0.04	O II 429	2.290	1414.43	0.33
1415.56	0.24	2.1	0.53	0.04	O II 430.0	2.290	1414.83	-0.73
					O II 430.1	2.290	1415.28	-0.28
1418.11	0.08	1.2	0.45	0.04	S IV 657	1.1574	1418.15	0.04
1420.33	0.26	1.3	0.26	0.04				
1421.41	0.12	0.6	0.17	0.04	N II 915	0.5524	1421.40	-0.01
1422.74	0.13	1.3	0.66	0.04	O II 429	2.308	1422.17	-0.57
					O II 430.0	2.308	1422.58	-0.16
					He I 522	1.725	1423.03	0.27
					O II 430.1	2.308	1423.03	0.27
					N III 763	0.8643	1423.09	0.35
1424.16	0.15	1.1	0.53	0.04	S II 763	0.8643	1423.69	-0.47
1426.61	0.08	2.3	1.33	0.04	S II 764	0.8643	1425.11	-1.50
					O II 429	2.315	1425.18	-1.43
					O II 430.0	2.315	1425.59	-1.02
					O II 430.1	2.315	1426.04	-0.57

Table 24 continued

λ_{obs}	σ_λ	FWHM	EW	σ_{EW}	ID	z	λ_{exp}	$\lambda_{exp} - \lambda_{obs}$
					N IV 765	0.8643	1426.47	-0.14
					S II 765	0.8643	1427.48	0.87
1431.42	0.23	4.7	1.89	0.04	H I 920	0.5524	1429.70	-1.72
					Ne VI 399	2.579	1430.96	-0.46
					Ne VI 433	2.308	1432.95	1.53
					H I 923	0.5524	1433.10	1.68
1434.45	0.07	1.1	0.51	0.04	C III 386	2.7125	1433.78	-0.67
					O II 832	0.722	1434.01	-0.44
					O III 832	0.722	1434.30	-0.15
					O II 833	0.722	1434.99	0.54
1437.08	0.13	2.9	1.48	0.04	Ne VI 401	2.579	1435.68	-1.40
					Ne VI 433	2.315	1435.98	-1.10
					Ne VIII 770	0.8643	1436.27	-0.81
					O II 834	0.722	1436.95	-0.13
					H I 926	0.5524	1437.87	0.79
1443.28	0.13	2.8	1.54	0.06	O IV 608	1.371	1442.51	-0.77
					O III 507	1.8451	1443.58	0.30
					H I 930	0.5524	1444.89	1.61
1576.78	0.24	2.5	0.91	0.09	O IV 554	1.8451	1576.40	-0.38
					N II 915	0.722	1576.69	-0.09
1579.39	0.12	1.2	0.55	0.08				
1581.43	0.15	1.3	0.42	0.08				
1583.48	0.18	1.4	0.43	0.08				
1588.90	0.35	3.1	0.78	0.08	Ne V 480	2.308	1589.20	0.30
					Ne VI 558	1.8451	1589.24	0.34
					H I 923	0.722	1589.67	0.77
1592.71	0.16	2.5	1.23	0.08	He I 584	1.725	1592.31	-0.40
					Ly β	0.5524	1592.33	-0.38
					Ne V 480	2.315	1592.56	-0.15
1599.31	0.32	4.4	1.71	0.08	Ne VII 465	2.433	1597.10	-2.21
					Ne VII 465	2.439	1599.90	0.59
1602.92	0.17	1.9	0.68	0.08	O VI 1031	0.5524	1601.96	-0.96
					H I 930	0.722	1602.75	-0.17
1607.56	0.36	4.0	1.05	0.08	S III 677	1.371	1606.94	-0.62
					S IV 744	1.1574	1607.09	-0.47
					S VI 933	0.722	1607.28	-0.28
					O III 507	2.168	1607.41	-0.15
					Ne VI 433	2.7125	1608.17	0.61
					C II 1036	0.5524	1608.81	1.25
1611.59	0.29	1.9	0.49	0.08	O VI 1037	0.5524	1610.80	-0.79
1614.89	0.25	2.5	0.83	0.08	S IV 748	1.1574	1614.60	-0.29
					Ne III 488	2.308	1614.66	-0.23
					Ly ϵ	0.722	1614.90	0.01

Table 24 continued

λ_{obs}	σ_λ	FWHM	EW	σ_{EW}	ID	z	λ_{exp}	$\lambda_{exp} - \lambda_{obs}$
1617.63	0.29	1.6	0.42	0.08	Ne v 568	1.8451	1617.21	-0.42
					O III 507	2.189	1618.07	0.44
					Ne III 488	2.315	1618.08	0.45
1622.78	0.24	1.7	0.41	0.09	He I 512	2.168	1622.33	-0.45
					Ne III 489	2.315	1622.71	-0.07
1628.69	0.23	2.1	0.50	0.08	C II 687	1.371	1629.00	0.31
1633.32	0.44	2.3	0.56	0.08	He I 512	2.189	1633.08	-0.24
					He I 515	2.168	1633.47	0.15
1635.54	0.28	1.5	0.44	0.08	Ly δ	0.722	1635.46	-0.08
1638.95	0.77	4.5	0.73	0.08				
1643.62	0.22	1.4	0.32	0.08	He I 515	2.189	1644.30	0.68
1647.10	0.20	2.5	0.95	0.09	N III 763	1.1574	1646.83	-0.27
					S II 763	1.1574	1647.51	0.41
1650.86	0.41	2.6	0.70	0.08	Ne v 480	2.433	1649.25	-1.61
					N IV 765	1.1574	1650.73	-0.13
					S II 765	1.1574	1651.91	1.05
					Ne v 480	2.439	1652.13	1.27
1654.68	0.50	3.8	1.13	0.08	He I 522	2.168	1654.37	-0.31
					S III 698	1.371	1656.69	2.01
1660.51	0.32	1.7	0.37	0.08				
1662.86	0.17	1.6	0.56	0.08	Ne VIII 770	1.1574	1662.08	-0.78
1670.01	0.20	2.7	1.05	0.08	He I 584	1.8451	1662.49	-0.37
					O III 507	2.290	1669.32	-0.69
1675.21	0.51	5.7	1.37	0.08	Al II 1670	0.0	1670.79	0.78
					Ly γ	0.722	1674.71	-0.50
1682.35	0.24	3.0	1.31	0.08	Ne III 488	2.433	1675.67	0.46
					O III 507	2.308	1678.45	3.24
					Ne III 488	2.439	1678.60	3.39
					Ne III 489	2.433	1680.47	-1.88
					O III 507	2.315	1682.00	-0.35
					C III 977	0.722	1682.43	0.08
1686.85	0.25	3.5	1.45	0.08	Ne III 489	2.439	1683.41	1.06
					Ne VIII 780	1.1574	1683.47	1.12
1690.29	0.32	1.9	0.45	0.08	C II 903.6	0.8643	1684.63	-2.22
					He I 512	2.290	1684.80	-2.05
					C II 903.9	0.8643	1685.26	-1.59
					C IV 1548	0.09	1687.53	0.68
1696.85	0.90	3.7	0.86	0.08	N II 533	2.168	1690.16	-0.13
					C IV 1550	0.09	1690.34	0.05
1696.85	0.90	3.7	0.86	0.08	N III 685	1.4735	1695.62	-1.23
					He I 515	2.290	1696.38	-0.47
					S v 786	1.1574	1696.75	-0.10
					He I 512	2.315	1697.61	0.76

Table 24 continued

λ_{obs}	σ_λ	FWHM	EW	σ_{EW}	ID	z	λ_{exp}	$\lambda_{exp} - \lambda_{obs}$
1700.48	0.44	3.1	1.18	0.08	O IV 787	1.1574	1699.41	-1.07
					C II 687	1.4735	1699.42	-1.06
					He I 537	2.168	1701.31	0.83
1704.30	0.12	1.4	0.48	0.08	N III 989	0.722	1704.43	0.13
1706.20	0.14	1.2	0.36	0.08	He I 515	2.308	1705.66	-0.54
					N II 915	0.8643	1706.98	0.78
1709.43	0.24	2.8	0.77	0.08	O II 539.0	2.168	1707.82	-1.61
					He I 515	2.315	1709.27	-0.16
					O II 539.5	2.168	1709.29	-0.14
					O II 539.8	2.168	1710.26	0.83
1714.09	0.17	1.4	0.38	0.08	Ne IV 541	2.168	1714.29	0.20
					O III 507	2.380	1714.98	0.87
1716.77	0.20	3.3	1.31	0.08	O V 629	1.725	1716.01	-0.76
					H I 920	0.8643	1716.95	0.18
					Ne IV 542	2.168	1717.29	0.52
					He I 522	2.290	1718.08	1.31
					O II 539.5	2.189	1720.62	-0.37
1720.99	0.39	2.5	0.48	0.08	H I 923	0.8643	1721.03	0.04
					O II 539.8	2.189	1721.60	0.61
					H I 926	0.8643	1726.76	0.12
1726.64	0.09	1.9	1.24	0.08	Ne VII 465	2.7125	1727.13	0.49
					He I 522	2.308	1727.48	0.84
					O IV 608	1.8451	1730.95	0.65
1730.30	0.30	3.8	1.14	0.07	He I 522	2.315	1731.14	0.84
					H I 930	0.8643	1735.19	0.04
1735.15	0.12	2.1	0.85	0.07	H I 930	0.8643	1735.19	0.04
1741.97	0.12	2.4	1.20	0.07	O III 507	2.433	1741.87	-0.10
1745.53	0.21	2.1	0.62	0.07	O III 507	2.439	1744.92	-0.61
1748.23	0.12	1.8	0.93	0.07	Ly ϵ	0.8643	1748.35	0.12
1751.94	0.30	3.9	1.22	0.07	Ne III 489	2.579	1751.94	0.00
					O IV 553	2.168	1752.95	1.01
1755.10	0.23	1.2	0.24	0.07	O IV 554	2.168	1755.31	0.21
1758.36	0.58	4.2	0.71	0.07	N II 644	1.725	1756.63	-1.73
					He I 512	2.433	1758.03	-0.33
					S VI 944	0.8643	1760.87	2.51
1766.05	0.14	2.4	1.07	0.07	O IV 553	2.189	1764.57	-1.48
					N II 533	2.308	1764.85	-1.20
					Ly β	0.722	1766.29	0.24
					He I 537	2.290	1766.83	0.78
					O IV 554	2.189	1766.95	0.90
1770.37	0.14	3.5	1.89	0.07	N II 533	2.315	1768.59	-1.78
					Ne VI 558	2.168	1769.61	-0.76
					He I 515	2.433	1770.11	-0.26
					Ly δ	0.8643	1770.61	0.24

Table 24 continued

λ_{obs}	σ_λ	FWHM	EW	σ_{EW}	ID	z	λ_{exp}	$\lambda_{exp} - \lambda_{obs}$
1775.62	0.21	1.8	0.47	0.07	O II 539.5	2.290	1775.12	-0.50
					O II 539.8	2.290	1776.12	0.50
					He I 537	2.308	1776.50	0.88
1778.08	1.34	4.7	1.08	0.07	O VI 1031	0.722	1776.98	-1.10
					He I 537	2.315	1780.25	2.17
1786.74	0.11	0.9	0.32	0.08	O VI 1037	0.722	1786.78	0.04
					O II 539.0	2.315	1787.07	0.33
1792.16	0.21	3.7	1.36	0.07	Ne IV 541	2.308	1790.05	-2.11
					S IV 657	1.725	1791.25	-0.91
					O V 629	1.8451	1791.64	-0.52
					He I 522	2.433	1792.76	0.60
					Ne IV 542	2.308	1793.18	1.02
					Ne IV 541	2.315	1793.84	1.68
					He I 522	2.439	1795.89	-1.04
1796.93	0.14	2.6	1.13	0.07	O II 832	1.1574	1796.59	-0.34
					O III 832	1.1574	1796.96	0.03
					Ne IV 542	2.315	1796.97	0.04
					O II 833	1.1574	1797.82	0.89
1801.14	0.39	2.1	0.47	0.07	O II 834	1.1574	1800.28	-0.86
					Ne V 568	2.168	1800.75	-0.39
1803.23	0.19	1.4	0.49	0.07	Ne IV 543	2.315	1803.00	-0.23
1807.36	0.23	1.8	0.40	0.07	Si II 1808	0.0	1808.01	0.65
1813.15	0.09	1.9	0.97	0.07	Ne III 488	2.7125	1812.10	-1.05
					S II 764	1.371	1812.44	-0.71
					Ly γ	0.8643	1813.10	-0.05
					NIV 765	1.371	1814.17	1.02
1816.35	0.13	1.0	0.29	0.07	S II 765	1.371	1815.46	-0.89
					O III 507	2.579	1815.95	-0.40
1821.53	0.13	2.8	1.23	0.07	O IV 553	2.290	1820.46	-1.07
					C III 977	0.8643	1821.46	-0.07
					O IV 554	2.290	1822.91	1.48
1834.17	0.19	3.2	1.57	0.07	He I 512	2.579	1832.80	-1.37
					O IV 554	2.308	1832.88	-1.29
					N II 644	1.8451	1834.05	-0.12
					O IV 553	2.315	1834.29	0.12
					N II 533	2.439	1834.74	0.57
1837.05	0.11	1.6	0.94	0.07	O IV 554	2.315	1836.76	-0.29
1843.59	0.48	3.1	0.71	0.08	He I 537	2.433	1843.62	0.03
					N III 989	0.8643	1845.28	1.69
					He I 515	2.579	1845.39	1.80
1846.90	0.39	2.3	0.54	0.08	He I 537	2.439	1846.85	-0.05
					S III 677	1.725	1846.86	-0.04
					Ne VI 558	2.308	1847.82	0.92

Table 24 continued

λ_{obs}	σ_λ	FWHM	EW	σ_{EW}	ID	z	λ_{exp}	$\lambda_{exp} - \lambda_{obs}$
					Si II 1190	0.5524	1848.00	1.10
1850.80	0.22	1.8	0.50	0.08	Ne VIII 780	1.371	1850.15	-0.65
					O II 539.0	2.433	1850.68	-0.12
					He I 584	2.168	1851.17	0.37
					Ne VI 558	2.315	1851.73	0.93
1854.35	0.30	4.1	1.39	0.08	O II 539.5	2.433	1852.27	-2.08
					Si II 1193	0.5524	1852.46	-1.89
					O II 539.8	2.433	1853.32	-1.03
					O II 539.0	2.439	1853.92	-0.43
					O II 539.5	2.439	1855.51	1.16
					O II 539.8	2.439	1856.56	2.21
1858.44	0.21	2.0	0.61	0.08	Ne IV 541	2.433	1857.69	-0.75
1867.26	0.17	2.2	0.78	0.08	N III 684	1.725	1866.61	-0.65
					Ne IV 543	2.433	1867.18	-0.08
					O IV 787	1.371	1867.66	0.40
					N III 685	1.725	1868.02	0.76
1871.69	0.20	3.2	1.52	0.08	S IV 657	1.8451	1870.20	-1.49
					O IV 553	2.380	1870.26	-1.46
					Ne IV 543	2.439	1870.44	-1.25
					C II 687	1.725	1872.22	0.53
					O IV 554	2.380	1872.77	1.06
					Si III 1206	0.5524	1872.97	1.28
1875.96	0.43	3.0	0.69	0.08				
1880.07	0.23	2.8	0.83	0.08	C IV 1548	0.214	1879.51	-0.56
					Ne V 568	2.308	1880.33	0.26
1884.85	0.16	1.4	0.41	0.08	Ne V 568	2.315	1884.31	-0.54
					C II 594	2.168	1884.33	-0.52
1887.18	0.08	1.7	1.06	0.08	Ly α	0.5524	1887.21	0.03
					N III 763	1.4735	1888.12	0.94
1898.97	0.45	2.6	0.47	0.09	O IV 553	2.433	1899.58	0.61
					O III 507	2.7444	1899.87	0.90
1902.44	0.26	2.1	0.95	0.08	He I 512	2.7125	1901.16	-1.28
					O IV 554	2.433	1902.14	-0.30
					O IV 553	2.439	1902.90	0.46
1905.33	0.55	3.5	1.45	0.09	S III 698	1.725	1904.04	-1.29
					O IV 554	2.439	1905.46	0.13
1912.72	0.11	3.2	1.88	0.08	Ly β	2.579	1912.25	-0.47
					O III 702	1.725	1913.85	1.13
					He I 515	2.7125	1914.22	1.50
1917.89	0.23	2.9	0.99	0.08	He I 512	2.7444	1917.50	-0.39
					Ne VI 558	2.433	1917.64	-0.25
1922.97	0.16	4.2	2.53	0.08	Ne VI 558	2.439	1920.99	-1.98
					He I 537	2.579	1922.03	-0.94

Table 24 continued

λ_{obs}	σ_λ	FWHM	EW	σ_{EW}	ID	z	λ_{exp}	$\lambda_{exp} - \lambda_{obs}$
					He I 584	2.290	1922.46	-0.51
					N v 1238	0.5524	1923.15	0.18
					O VI 1031	0.8643	1923.82	0.85
1927.98	0.33	2.3	0.47	0.08	O IV 608	2.168	1927.40	-0.58
					S III 677	1.8451	1928.26	0.28
					N v 1242	0.5524	1929.33	1.35
					O II 539.0	2.579	1929.39	1.41
1933.29	0.44	2.7	1.07	0.08	C II 1036	0.8643	1932.04	-1.25
					O II 539.8	2.579	1932.14	-1.15
					He I 584	2.308	1932.98	-0.31
					O VI 1037	0.8643	1934.43	1.14
1936.36	1.09	4.5	1.87	0.08	Ne IV 541	2.579	1936.69	0.33
					He I 584	2.315	1937.07	0.71
					He I 522	2.7125	1938.72	2.36
1941.04	0.27	1.5	0.30	0.08	Ne IV 542	2.579	1940.08	-0.96
					O IV 608	2.189	1940.18	-0.86
1946.15	0.16	1.4	0.40	0.08	Ne IV 543	2.579	1946.59	0.44
1950.40	0.19	3.2	1.10	0.08	O IV 787	1.4735	1948.40	-2.00
					N III 684	1.8451	1948.88	-1.52
					C II 903.6	1.1574	1949.48	-0.92
					C II 903.9	1.1574	1950.21	-0.19
					N III 685	1.8451	1950.35	-0.05
					Ne v 568	2.433	1951.39	0.99
1954.75	0.37	2.3	0.39	0.08	C II 687	1.8451	1954.73	-0.02
					Ne v 568	2.439	1954.80	0.05
					He I 522	2.7444	1955.37	0.62
1964.48	0.28	2.8	0.64	0.08				
1991.70	0.10	1.5	0.60	0.06	H I 923	1.1574	1991.60	-0.10
1994.77	0.17	2.2	0.70	0.06	He I 537	2.7125	1993.72	-1.05
					O v 629	2.168	1994.98	0.21
1998.19	0.10	2.2	1.06	0.06	O III 702	1.8451	1998.20	0.01
					H I 926	1.1574	1998.24	0.05
					Ne VI 558	2.579	1999.19	1.00
2006.46	0.70	2.8	1.47	0.06	He I 584	2.433	2006.02	-0.44
2008.96	1.05	3.0	1.20	0.06	H I 930	1.1574	2008.00	-0.96
					O v 629	2.189	2008.21	-0.75
					Ne IV 541	2.7125	2008.93	-0.03
					He I 584	2.439	2009.52	0.56
					C II 594	2.380	2010.42	1.43
					He I 537	2.7444	2010.86	1.90
2014.34	0.23	3.4	1.40	0.06	Ne IV 542	2.7125	2012.45	-1.89
					O IV 608	2.308	2012.58	-1.76
					S VI 933	1.1574	2013.67	-0.67

Table 24 continued

λ_{obs}	σ_λ	FWHM	EW	σ_{EW}	ID	z	λ_{exp}	$\lambda_{exp} - \lambda_{obs}$
2017.29	0.13	1.8	0.80	0.06	O IV 608	2.315	2016.84	-0.45
2023.08	0.08	1.8	0.86	0.06	Ly ϵ	1.1574	2023.22	0.14
2042.36	0.22	2.8	0.65	0.06	N II 644	2.168	2042.20	-0.16
2045.46	0.10	1.2	0.39	0.06				
2049.10	0.07	1.5	0.78	0.06	Ly δ	1.1574	2048.98	-0.12
					Si II 1190	0.722	2049.90	0.80
2064.31	0.20	2.8	0.64	0.06	O II 834	1.4735	2064.05	-0.26
2069.01	0.14	1.4	0.37	0.06				
2072.34	0.23	3.6	0.97	0.06	C II 1334	0.5524	2071.73	-0.61
					O V 629	2.290	2071.81	-0.53
					O IV 553	2.7444	2071.89	-0.45
					Ne VI 558	2.7125	2073.77	1.43
2077.57	0.16	1.8	0.49	0.06	Si III 1206	0.722	2077.59	0.02
2079.59	0.17	1.1	0.21	0.06	N III 763	1.725	2080.10	0.53
2083.32	0.12	2.7	0.99	0.06	S IV 657	2.168	2082.45	-0.87
					S II 764	1.725	2083.04	-0.28
					O V 629	2.308	2083.15	-0.17
2087.90	0.07	3.0	1.81	0.05	S II 765	1.725	2086.51	-1.39
					O V 629	2.315	2087.56	-0.34
					O IV 608	2.433	2088.63	0.73
2092.98	0.06	2.8	1.90	0.05	He I 584	2.579	2091.33	-1.65
					O IV 608	2.439	2092.28	-0.70
					Ly α	0.722	2093.38	0.40
2095.89	0.12	1.5	0.63	0.05				
2097.79	0.15	2.4	1.68	0.05	Ly γ	1.1574	2098.15	0.36
2105.63	0.21	1.3	0.20	0.05				
2108.00	0.06	1.8	1.09	0.05	C III 977	1.1574	2107.82	-0.18
2110.15	0.11	1.2	0.35	0.05	Ne V 568	2.7125	2110.26	0.11
2122.57	0.28	1.6	0.20	0.05				
2126.82	1.66	2.8	0.37	0.05	Ne VIII 780	1.725	2126.38	-0.44
2129.48	0.75	2.6	0.66	0.05	O V 629	2.380	2128.49	-1.02
					S IV 748	1.8451	2129.27	-0.21
2133.27	0.42	3.7	0.70	0.05	N II 644	2.308	2132.45	-0.82
					N V 1238	0.722	2133.25	-0.02
2135.76	0.54	2.8	0.47	0.05	N III 989	1.1574	2135.39	-0.37
					N II 644	2.315	2136.96	1.20
2137.84	0.09	1.2	0.52	0.05				
2140.21	0.24	2.9	0.75	0.05	N V 1242	0.722	2140.11	-0.10
2143.31	0.50	2.3	0.33	0.05	C II 903.6	1.371	2142.49	-0.82
					S V 786	1.725	2143.16	-0.15
					C II 903.9	1.371	2143.29	-0.02
2146.37	0.27	2.7	0.75	0.05	O IV 787	1.725	2146.51	0.14
					S III 677	2.168	2147.10	0.73

Table 24 continued

λ_{obs}	σ_λ	FWHM	EW	σ_{EW}	ID	z	λ_{exp}	$\lambda_{exp} - \lambda_{obs}$
2149.66	0.32	2.4	0.36	0.05				
2154.18	0.18	4.7	1.73	0.05				
2158.80	0.16	1.7	0.53	0.05				
2161.57	0.11	2.5	1.25	0.05	O v 629	2.433	2161.86	0.29
2165.73	0.10	3.3	1.86	0.05	Si iv 1393	0.5524	2163.67	-2.06
					O v 629	2.439	2165.64	-0.09
2170.64	0.43	3.1	0.76	0.05	N III 684	2.168	2170.07	-0.57
					Si II 1260	0.722	2170.45	-0.19
					N II 915	1.371	2170.92	0.28
					N III 685	2.168	2171.71	1.07
					N III 763	1.8451	2171.78	1.14
2175.97	2.48	4.6	1.60	0.05	S IV 657	2.308	2174.48	-1.49
					S II 764	1.8451	2174.85	-1.12
					C II 687	2.168	2176.58	0.61
					N IV 765	1.8451	2176.92	0.95
2178.65	0.38	2.8	1.28	0.05	O IV 608	2.579	2177.46	-1.19
					Si IV 1402	0.5524	2177.66	-0.99
					S II 765	1.8451	2178.47	-0.18
					S IV 657	2.315	2179.08	0.43
2183.77	0.21	2.9	0.64	0.05	H I 920	1.371	2183.60	-0.17
					N III 684	2.189	2184.45	0.68
2187.99	0.24	2.3	0.41	0.05	He I 584	2.7444	2187.98	-0.01
					H I 923	1.371	2188.79	0.80
2191.66	0.17	2.1	0.44	0.05	C II 687	2.189	2191.01	-0.65
					Ne VIII 770	1.8451	2191.89	0.23
2196.06	0.25	3.7	0.70	0.05	H I 926	1.371	2196.08	0.02
2200.70	0.16	1.8	0.40	0.05				
2206.80	0.09	1.4	0.45	0.05	H I 930	1.371	2206.80	0.00
2210.12	0.30	1.9	0.31	0.05				
2212.82	0.09	2.3	1.40	0.05	Ly β	1.1574	2212.89	0.07
					N II 644	2.433	2213.03	0.21
					S VI 933	1.371	2213.04	0.22
					S III 698	2.168	2213.58	0.76
2223.86	0.24	3.4	1.07	0.05	Ly ϵ	1.371	2223.53	-0.33
					Si II 1193	0.8643	2224.65	0.79
					O III 702	2.168	2224.99	1.13
2226.06	0.08	0.9	0.32	0.05	O VI 1031	1.1574	2226.28	0.22
2228.15	0.14	1.9	0.55	0.05				
2238.24	0.26	2.3	0.52	0.05	S V 786	1.8451	2237.61	-0.63
					O VI 1037	1.1574	2238.55	0.31
					S VI 944	1.371	2239.46	1.22
2241.23	0.16	2.0	0.62	0.05	O IV 787	1.8451	2241.12	-0.11
					S III 677	2.308	2241.98	0.75

Table 24 continued

λ_{obs}	σ_λ	FWHM	EW	σ_{EW}	ID	z	λ_{exp}	$\lambda_{exp} - \lambda_{obs}$
2246.79	0.14	1.7	0.62	0.05	S III 677	2.315	2246.73	-0.06
2249.34	0.25	2.6	0.85	0.05	Si III 1206	0.8643	2249.28	-0.06
2252.61	0.27	3.2	1.38	0.05	Ly δ	1.371	2251.84	-0.77
					N III 684	2.290	2253.64	1.03
					O V 629	2.579	2253.80	1.19
2260.87	0.46	2.8	0.42	0.05	C II 687	2.290	2260.40	-0.47
					S IV 657	2.439	2260.59	-0.28
2263.84	0.20	1.8	0.57	0.05				
2266.46	0.13	3.0	2.20	0.05	N III 684	2.308	2265.97	-0.49
					Ly α	0.8643	2266.37	-0.09
					N III 685	2.308	2267.68	1.22
2269.45	0.15	1.1	0.28	0.06	O II 832	1.725	2269.26	-0.19
					O III 832	1.725	2269.73	0.28
2272.09	0.36	3.8	0.89	0.06	N III 684	2.308	2270.76	-1.33
					O II 833	1.725	2270.82	-1.27
					N III 685	2.315	2272.48	0.39
					O II 834	1.725	2273.92	1.83
2277.62	0.10	1.8	0.55	0.05	C II 687	2.315	2277.58	-0.04
					H I 920	1.4735	2278.00	0.38
					O IV 608	2.7444	2278.09	0.47
2295.58	0.23	1.8	0.25	0.05	S III 724	2.168	2294.55	-1.03
2298.29	0.20	2.1	0.42	0.05	C II 1334	0.722	2298.06	-0.23
2300.70	0.17	1.3	0.29	0.05				
2302.56	0.73	2.8	0.46	0.05	H I 930	1.4735	2302.21	-0.35
2306.16	0.12	2.6	0.94	0.05	Ly γ	1.371	2305.88	-0.28
					N II 644	2.579	2307.14	0.98
2316.67	0.09	2.2	0.84	0.05	S III 698	2.315	2316.29	-0.38
					C III 977	1.371	2316.51	-0.16
					N V 1242	0.8643	2316.96	0.29
					N III 685	2.380	2317.03	0.33

C Column Densities

Column densities as fitted by eye using David Mar's Xvoigt are always given as $\log N[\text{cm}^{-2}]$ and the velocity parameter b is measured in km/s. Values, marked by a $^+$ are more reliable, since either at least one line (or multiplet) is unambiguously identified and obviously not affected by the blending problem or the value is derived from a Lyman edge. The values for neutral hydrogen of absorbers with $z \geq 1.4735$ are taken from VR 95. No value is given, if all sufficiently strong lines fall outside the covered spectral range or are too blended to provide useful constraints.

The interstellar absorption lines were fitted with $b = 50$ km/s, except for N I, for which 30 km/s was used.

Table 25 : Column Densities

z	H I(b)	He I(b)	O II			O III			O IV			O V			O VI			
			b=b _{HI}	50	100	b=b _{HI}	50	100	b=b _{HI}	50	100	b=b _{HI}	50	100	b=b _{HI}	50	100	
0.0																		
0.09	16.1 (30)																	
0.214	15.6 (30)																	
0.5524	15.8 (35) ⁺		<13.8	13.8	13.8	14.7	14.6	14.6	14.7	14.6	14.6					14.4 ⁺	14.3	14.3
0.722	16.3 (25) ⁺		14.7	14.6	14.5	15.1 ⁺	14.8	14.7	15.2	14.9	14.8					14.7	14.5	14.5
0.8643	16.0 (40) ⁺					15.4	14.9	14.7								14.6	14.4	14.4
1.1574	16.7 (30) ⁺	15.0 (30)				15.8	15.0	14.85				16.8	15.5	14.7	15.4	15.05	14.85	
1.371	15.85 (25) ⁺	<14.0 (25)	13.9	13.9	13.9	15.6 ⁺	15.0	14.7	16.1 ⁺	14.9	14.5	16.1 ⁺	14.9	14.5	14.55	14.45	14.4	
1.4735	15.4 (35) ^a	<14.1 (35)	13.8	13.8	13.8	<14.2	14.2	14.2	<14.2	14.7	14.7	<14.2	14.7	14.7				
1.725	17.05 (30) ^a	<14.2 (30)	<14.2	14.1	14.1	<14.2	14.2	14.2	<14.2	14.2	14.2	<14.2	14.2	14.2	14.4	14.1	14.1	
1.8451	16.75 (30) ^a	14.9 (30)	<14.4	14.4	14.4	14.3	14.3	14.3	14.3	14.2	14.2	14.4	14.1	14.1	14.9	14.4	14.4	
2.168	16.85 (25) ^a	15.0 (30)	<14.4	14.4	14.4	14.9 ⁺	14.7	14.5	14.9 ⁺	14.7	14.7	14.9	14.4	14.4	14.9	14.4	14.4	
2.189	15.4 (30) ^a	14.7 (25)	<14.2	14.2	14.2	14.7 ⁺	14.45	14.45	14.7 ⁺	14.45	14.45	14.6 ⁺	14.15	14.1	14.6 ⁺	14.15	14.1	
2.290	15.7 (30) ^a	<14.2 (30)	<14.2	14.2	14.2	<14.4	14.3	14.3	<14.4	14.4	14.4	<14.4	14.4	14.4	13.5	13.5	13.5	
2.308	15.7 (30) ^a	<14.2 (30)	<14.2	14.2	14.2	13.7	13.7	13.7	14.4	14.3	14.2	13.8	13.7	13.7	13.8	13.7	13.7	
2.308	15.7 (30) ^a	14.3 (30)	<14.0	14.0	14.0	14.5	14.4	14.4	14.3	14.3	14.2	14.0	13.8	13.8	14.0	13.8	13.8	
2.315	16.88 (30) ^a	14.8 (30)	14.0	14.0	14.0	14.8	14.6	14.6	16.15 ⁺	15.3	15.0	15.5	14.65	14.4	15.5	14.65	14.4	
2.380		<14.6 (30)				<14.7	14.5	14.5	<13.8	13.8	13.8	13.9	13.8	13.8	13.9	13.8	13.8	
2.433	16.6 (38) ^a	15.0 (38)	<14.6	14.6	14.6	15.2 ⁺	15.05	15.0	14.6	14.55	14.55	14.8	14.45	14.3	14.8	14.45	14.3	
2.439	15.89 (25) ^a	14.7 (25)	<14.2	14.2	14.2	14.8	14.6	14.5	15.5	14.85	14.75	15.5	14.6	14.35	15.5	14.6	14.35	
2.579	15.4 (40) ^a	14.2 (40)	14.2	14.2	14.2	14.4	14.3	14.3	15.3	14.75	14.65	14.2	14.1	14.0	14.2	14.1	14.0	
2.7125		14.2 (30)	<14.2	14.2	14.2	<14.4	14.3	14.3	<14.2	14.2	14.2	<14.2	14.2	14.2	<14.2	14.2	14.2	
2.7444		<14.2 (30)	<14.2	14.2	14.2	<13.7	13.7	13.7	<13.9	13.9	13.9	<13.9	13.9	13.9	<13.9	13.9	13.9	

69

Table 25 continued

z	C II			C III			C IV			N II			N III			N IV		
	b=b _{HI}	50	100	b=b _{HI}	50	100	b=b _{HI}	50	100	b=b _{HI}	50	100	b=b _{HI}	50	100	b=b _{HI}	50	100
0.0			15.1															
0.09									14.4	14.3	14.25	<14.0	14.0	14.0				
0.214	<14.1	14.1	14.1	13.5	13.5	13.5	14.2	14.1	14.1	<14.1	14.1	14.1	14.3	14.3	14.3			
0.5524	13.5	13.5	13.5							<14.4	14.3	14.3				14.4	14.15	14.1
0.722	13.9	13.9	13.9	14.8	14.1	13.9	<14.4	14.3	14.3	<14.4	14.3	14.3	14.0	13.9	13.8	14.4	14.1	14.05
0.8643	<14.0	13.9	13.9	14.6	14.0	13.9	<14.3	14.2	14.2	<14.3	14.2	14.2	13.8	13.8	13.8	14.3	14.2	14.2
1.1574	<13.5	13.5	13.5	15.4 ⁺	14.35	14.05	<13.8	13.8	13.8	<13.8	13.8	13.8	14.2	14.1	14.1	14.2	14.0	13.9
1.371	<13.5	13.5	13.5	13.6	13.55	13.5	<14.2	14.2	14.2	<14.2	14.2	14.2	<13.6	13.6	13.6	13.5	13.4	13.4
1.4735	<13.4	13.4	13.4										<14.0	14.0	14.0	<13.5	13.5	13.5
1.725	13.9	13.9	13.9				<14.1	14.1	14.1	<14.1	14.1	14.1	<14.4	14.3	14.3	<13.4	13.4	13.4
1.8451	<14.3	14.3	14.3										13.9	13.9	13.9	13.9	13.8	13.8
2.168	<14.7	14.4	14.4				<14.4	14.3	14.3	<14.4	14.3	14.3	13.7	13.7	13.7			
2.189	<13.9	13.9	13.9	14.3	14.2	14.2							<13.8	13.7	13.7			
2.290	<13.9	13.9	13.9	<14.5	14.5	14.5							<13.6	13.6	13.6			
2.308	<14.0	14.0	14.0	14.0	14.0	14.0	<14.0	14.0	14.0	<14.0	14.0	14.0	<13.4	13.4	13.4			
2.315	14.1	14.05	14.05	15.0	14.6	14.6	14.1	14.1	14.1	14.1	14.1	14.1	14.2	14.0	14.0			
2.380	<14.5	14.3	14.3										<14.0	14.0	14.0			
2.433				14.5	14.4	14.4	<14.1	14.1	14.1	<14.1	14.1	14.1	13.7	13.7	13.7			
2.439				14.1	14.1	14.1	<13.9	13.9	13.9	<13.9	13.9	13.9	<13.6	13.6	13.6			
2.579				14.5	14.4	14.4	<13.9	13.9	13.9	<13.9	13.9	13.9	13.9	13.9	13.9			
2.7125				<14.6	14.5	14.5							<14.7	14.5	14.5			
2.7444							<13.7	13.7	13.7	<13.7	13.7	13.7	<13.7	13.7	13.7			

Table 25 continued

z	Si II			Si III			Si IV			N I			Al II			C II*		
	b=b _{HI}	50	100	b=b _{HI}	50	100	b=b _{HI}	50	100	b=b _{HI}	50	100	b=30	50	100	b=30	50	100
0.0		14.8			13.8			13.55		15.0				13.5				14.3
0.09	13.2	13.2	13.2	13.0	13.0	13.0												
0.214							<13.4	13.3	13.3									
0.5524	<13.2	13.2	13.2	13.5	13.3	13.2	<13.8	13.7	13.7									
0.722	<13.6	13.5	13.5	13.4 [†]	13.2	13.2												
0.8643	<13.4	13.4	13.4	13.5	13.3	13.3												
1.1574																		
1.371																		
1.4735																		
1.725																		
1.8451																		
2.168																		
2.189																		
2.290																		
2.308																		
2.315																		
2.380																		
2.433																		
2.439																		
2.579																		
2.7125																		
2.7444																		

D Calculated Spectrum

The normalized spectrum is plotted together with the 1σ error. The synthetic spectrum (dotted line) is computed with the column densities of the lines listed in Table 26. Apart from the hydrogen, helium and interstellar N I lines, $b = 50$ km/s was used throughout. Line identifications, plotted at the top of the spectrum denote those lines, included in the artificial spectrum, those at the bottom indicate lines, not considered reliably detected and thus not used for the calculation.

Table 25: Ions included in the synthetic spectrum

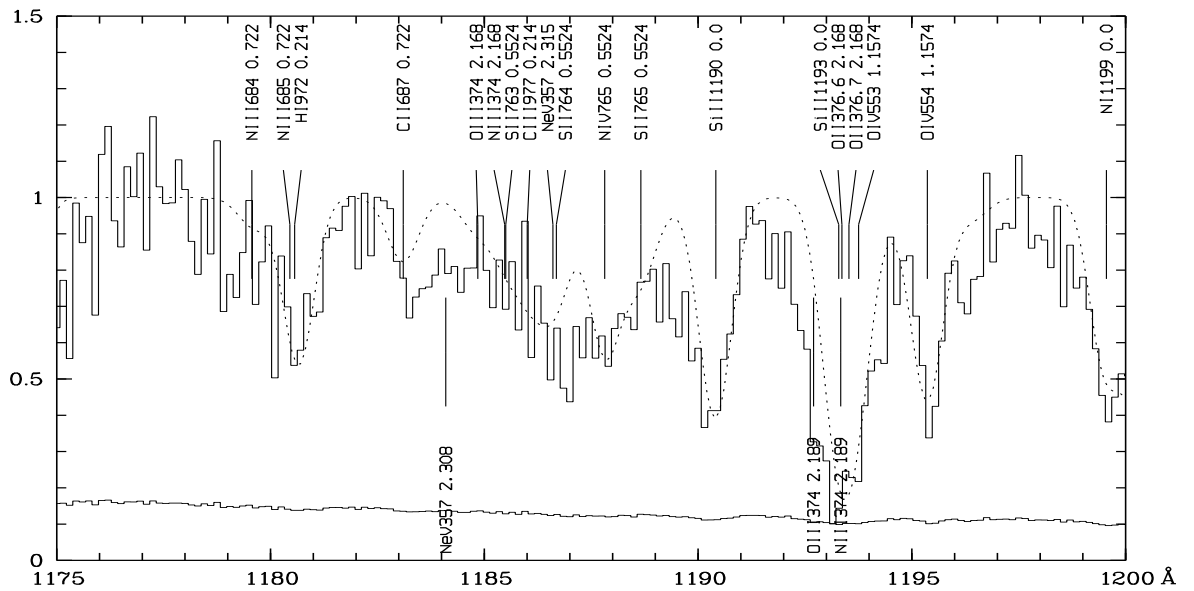
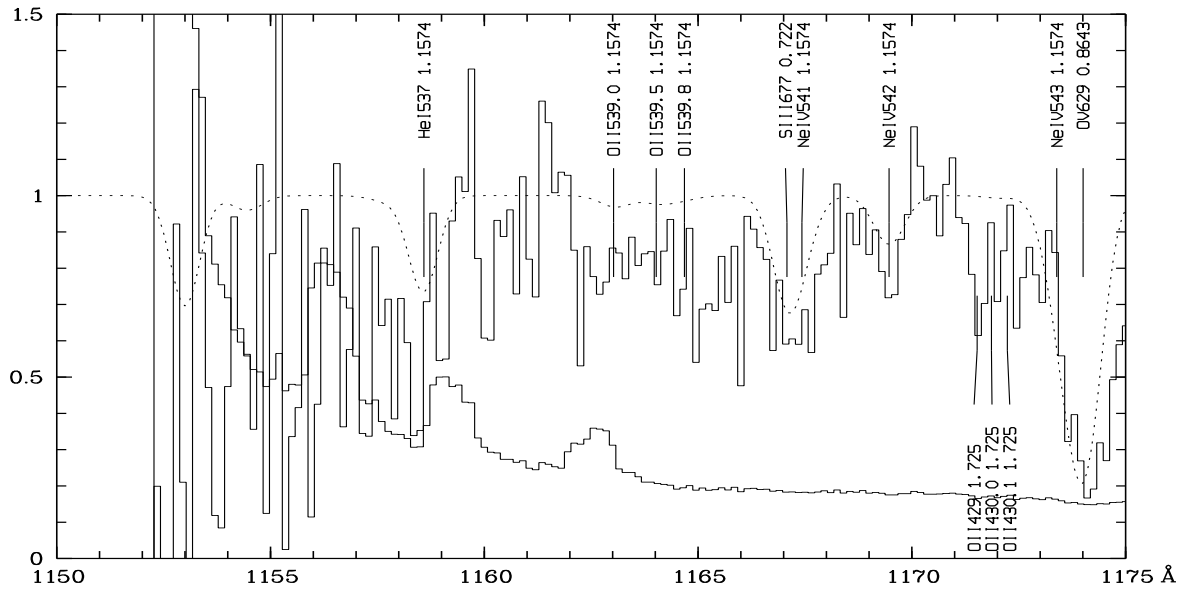
z	ion	b [km/s]	$\log N [cm^{-2}]$	z	ion	b [km/s]	$\log N [cm^{-2}]$
0.0	Al II	50	13.5	0.722	Si III	50	13.3
	C II	50	15.1		H I	25	16.3
	C II*	50	14.3		O II	50	14.6
	N I	30	15.0		O III	50	14.8
	S II	50	15.35		O IV	50	14.9
	Si II	50	14.80		O VI	50	14.4
	Si III	50	13.80		C II	50	13.9
	Si IV	50	13.55		C III	50	14.1
0.09	H I	30	16.1	N III	50	13.9	
	C IV	50	14.3	N IV	50	14.1	
	N V	50	14.3	N V	50	14.0	
	Si II	50	13.2	S III	50	13.5	
	Si III	50	13.0	S IV	50	13.65	
0.214	H I	30	15.6	S V	50	13.3	
	O VI	50	14.3	Si III	50	13.2	
	C III	50	13.5	Ne VIII	50	14.5	
	C IV	50	14.1	H I	40	16.0	
	N III	50	14.3	O III	50	14.9	
0.5524	H I	35	15.8	0.8643	O V	50	15.5
	O III	50	14.6		O VI	50	15.05
	O IV	50	14.6		C II	50	13.90
	O VI	50	14.5		C III	50	14.0
	C II	50	13.5		N III	50	13.8
	N IV	50	14.15		N IV	50	14.2
	S II	50	13.4		N V	50	13.7
	S V	50	13.3		S II	50	13.5

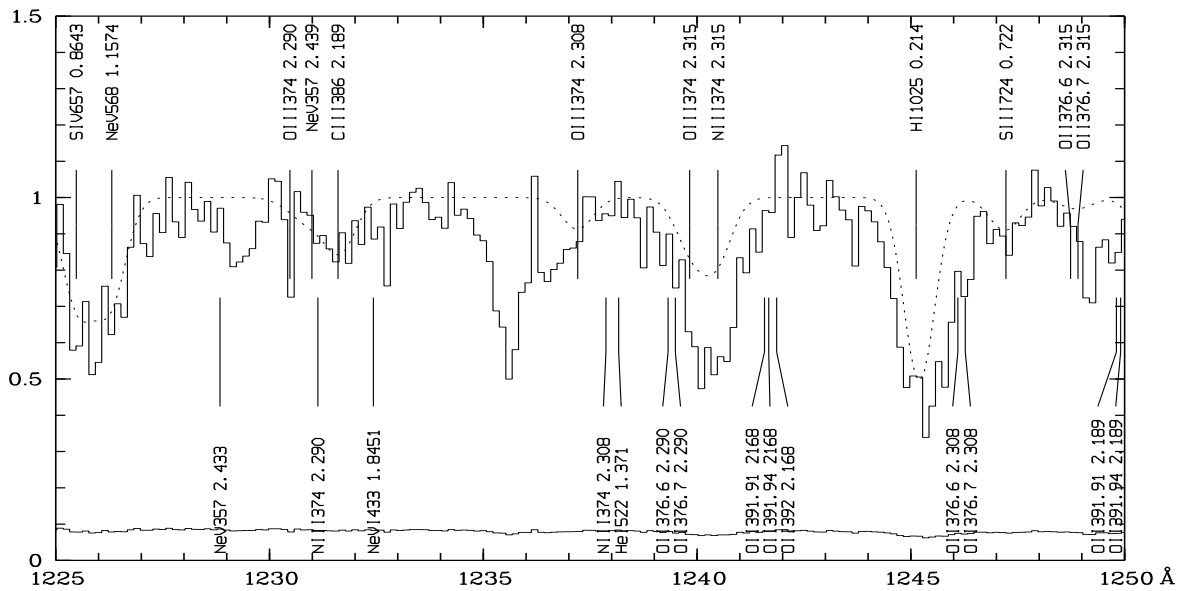
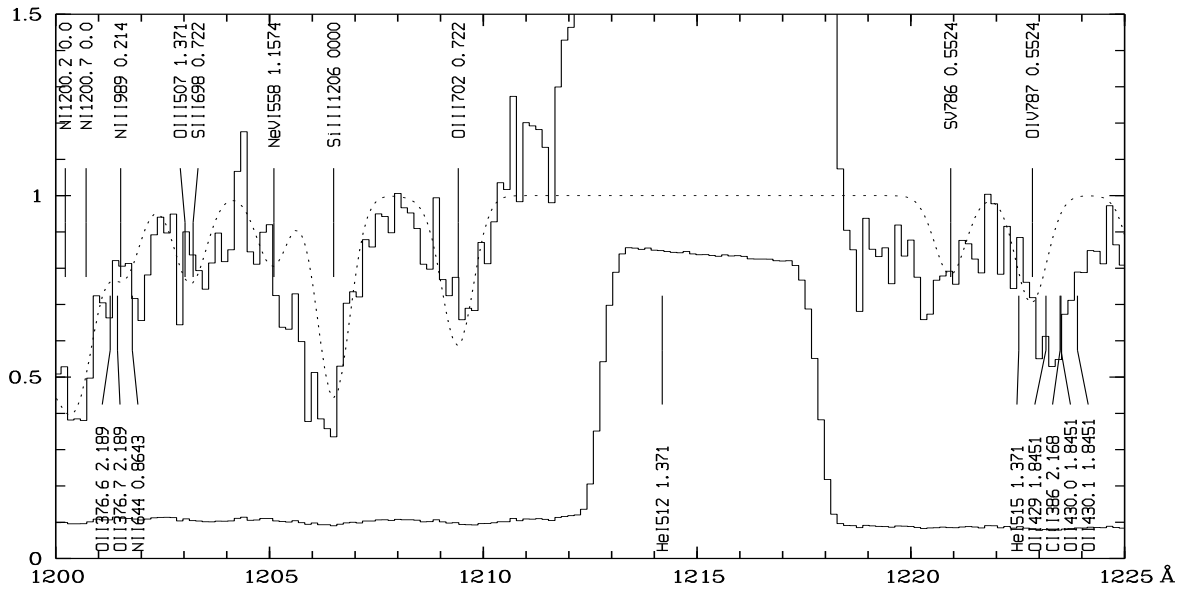
Table 26 continued

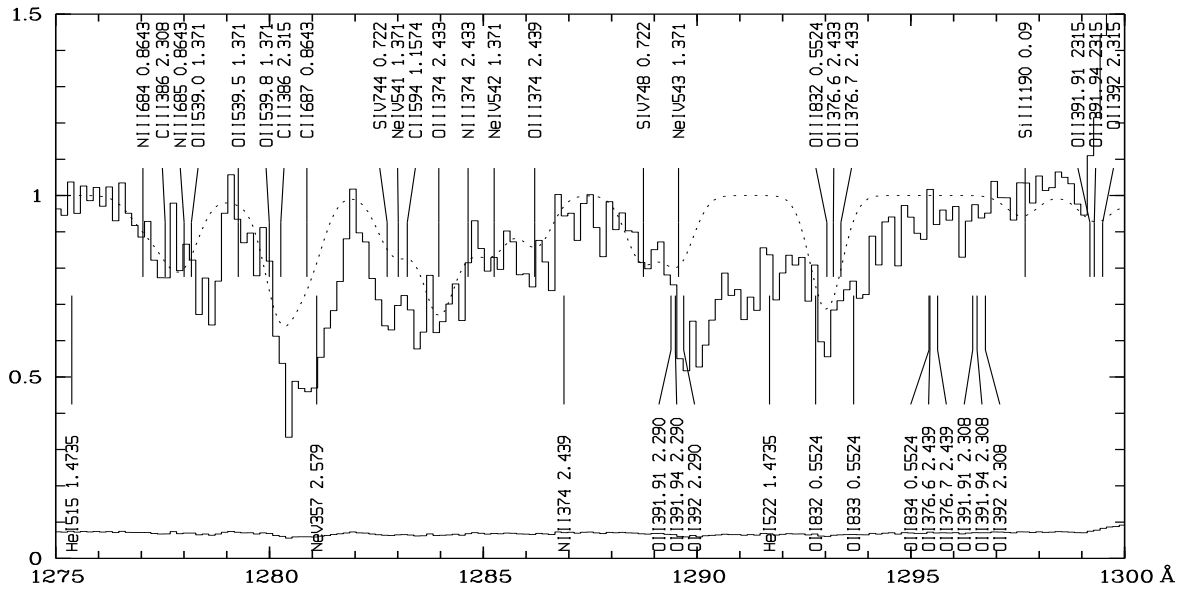
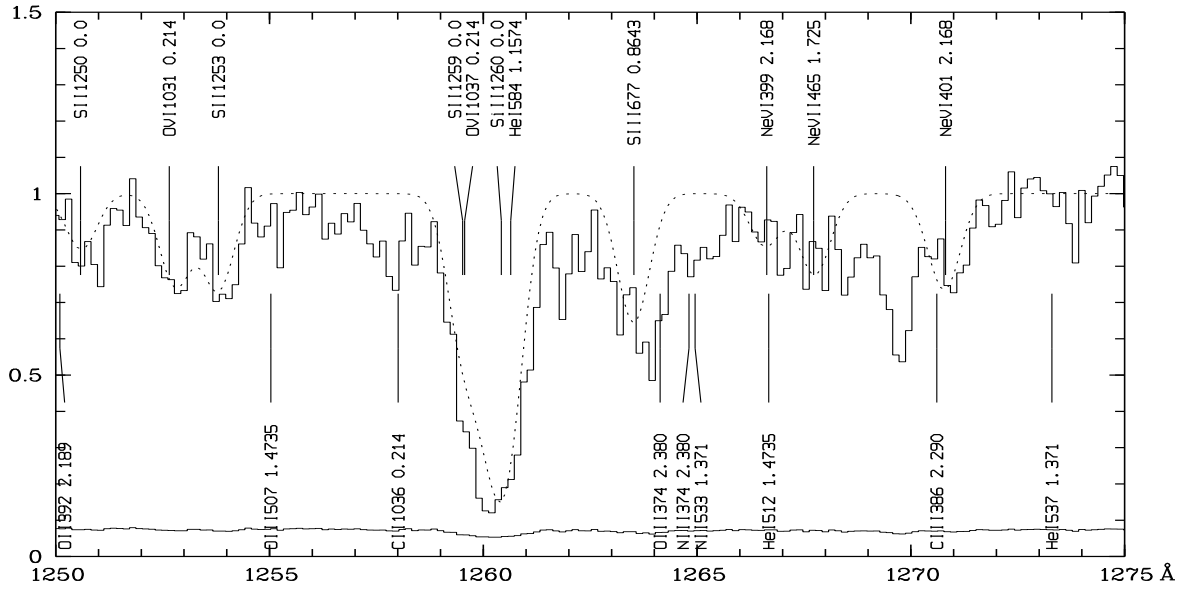
z	ion	b [km/s]	$\log N [cm^{-2}]$	z	ion	b [km/s]	$\log N [cm^{-2}]$		
1.1574	S III	50	13.6	1.8451	Ne VII	50	14.1		
	S IV	50	13.65		Ne VIII	50	14.3		
	Si III	50	13.3		He I	30	15.0		
	Ne VIII	50	14.4		O III	50	14.7		
	H I	30	16.7		O IV	50	14.7		
	He I	30	15.0		O V	50	14.4		
	O II	50	13.9		N III	50	13.9		
	O III	50	15.0		N IV	50	13.8		
	O IV	50	15.0		S II	50	13.1		
	O V	50	14.9		S III	50	13.15		
	O VI	50	14.45		S V	50	13.0		
	C II	50	13.5		Ne III	50	14.5		
	C III	50	14.35		Ne v	50	14.7		
	N III	50	14.1		Ne VII	50	14.15		
	N IV	50	14.0		Ne VIII	50	14.3		
	1.371	S IV	50		13.7	2.168	He I	50	14.7
S V		50	13.5	O III	50		14.4		
Ne IV		50	14.5	O IV	50		14.45		
Ne v		50	14.8	O V	50		14.15		
Ne VI		50	14.6	C II	50		13.6		
H I		25	15.85	N III	50		13.7		
O II		50	13.8	S III	50		13.2		
O III		50	14.0	S IV	50		13.2		
O IV		50	14.7	Ne IV	50		14.5		
C III		50	13.55	Ne v	50		14.5		
N IV		50	13.4	Ne VI	50		14.6		
Ne IV		50	14.45	2.189	O V		50	13.5	
Ne v		50	14.5		C III		50	14.2	
1.4735		H I	35	15.4	2.290		O III	50	13.7
1.725		He I	30	14.9			O IV	50	14.3
		O III	50	14.3	O V		50	13.7	
	O IV	50	14.2	2.308	He I	30	14.3		
	O V	50	14.1		O III	50	14.4		
	C II	50	13.9		O IV	50	14.3		
	S III	50	13.3		O V	50	13.8		
	Ne III	50	15.1		C III	50	14.0		
	Ne v	50	14.4		S IV	50	13.4		

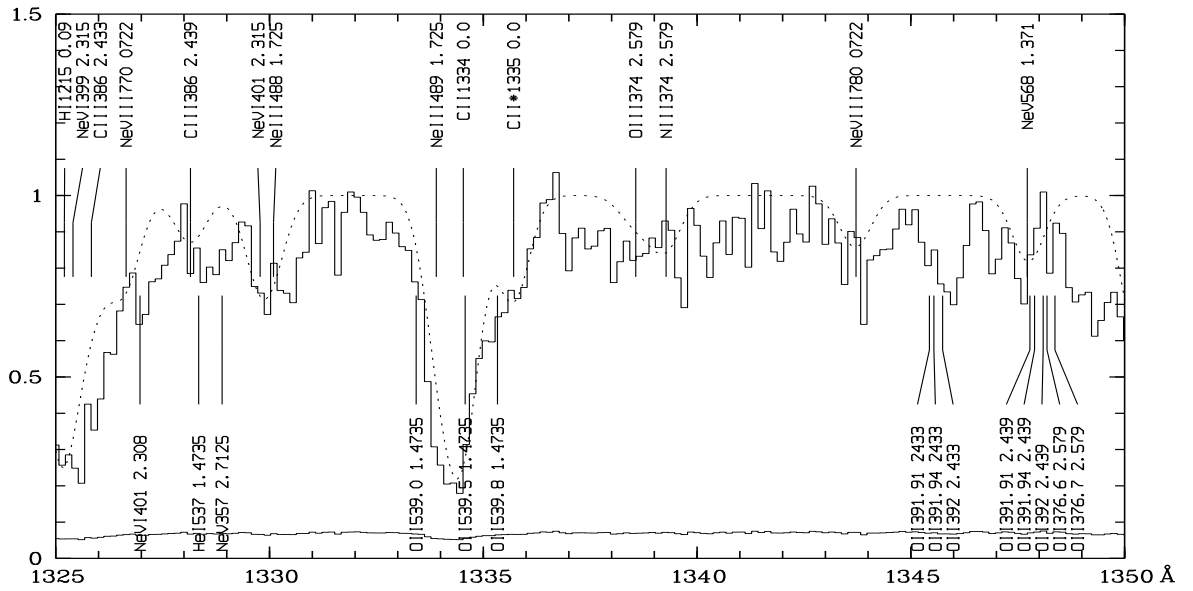
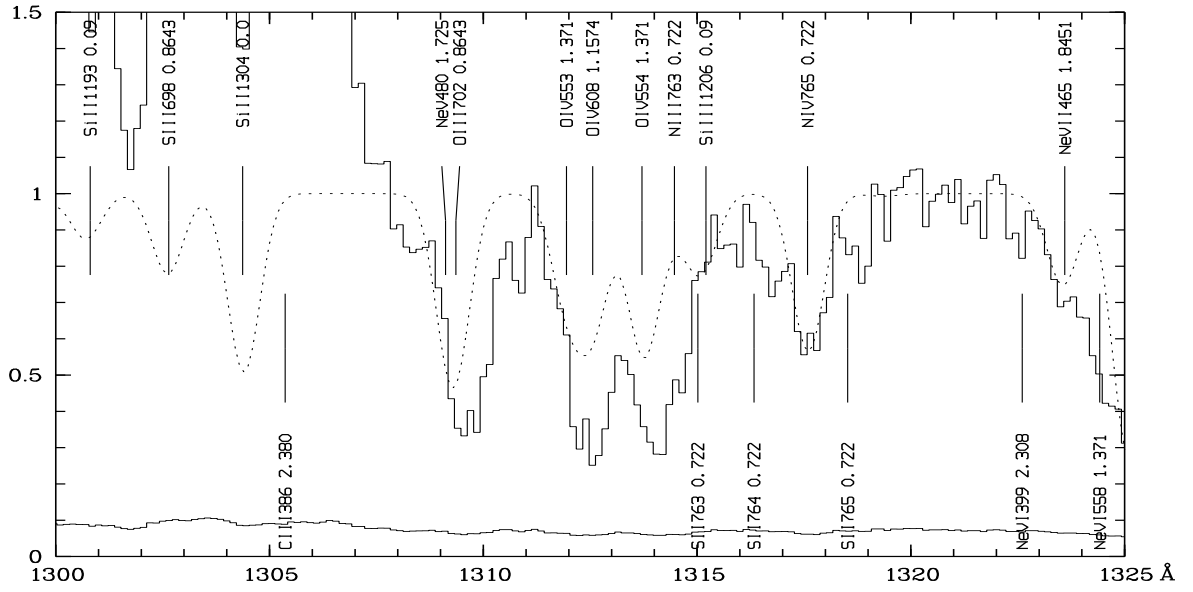
Table 26 continued

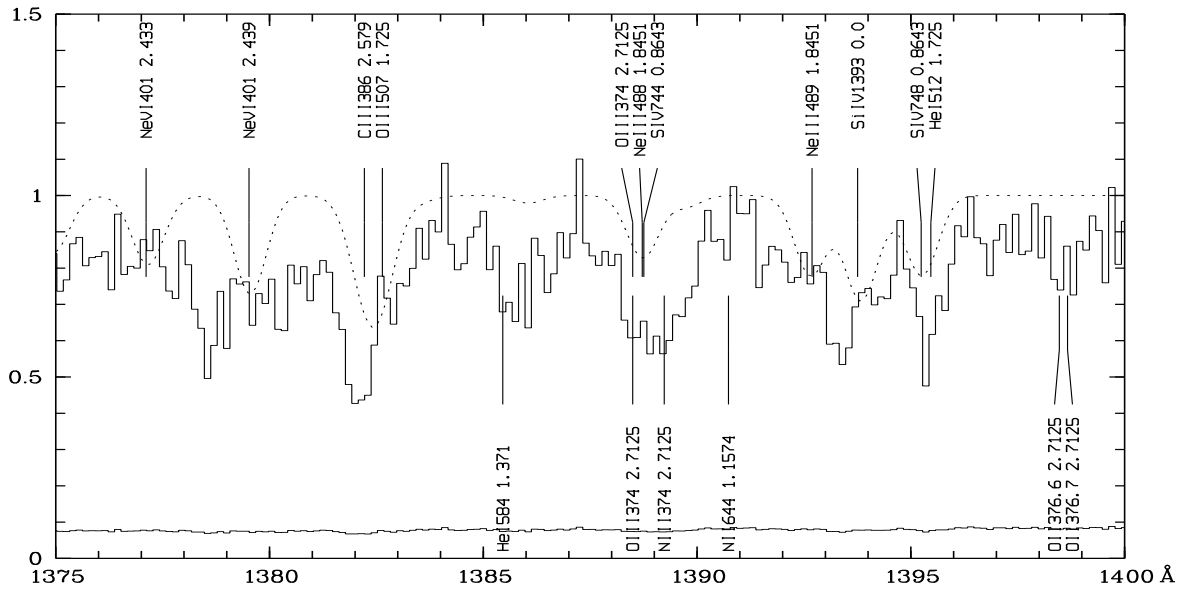
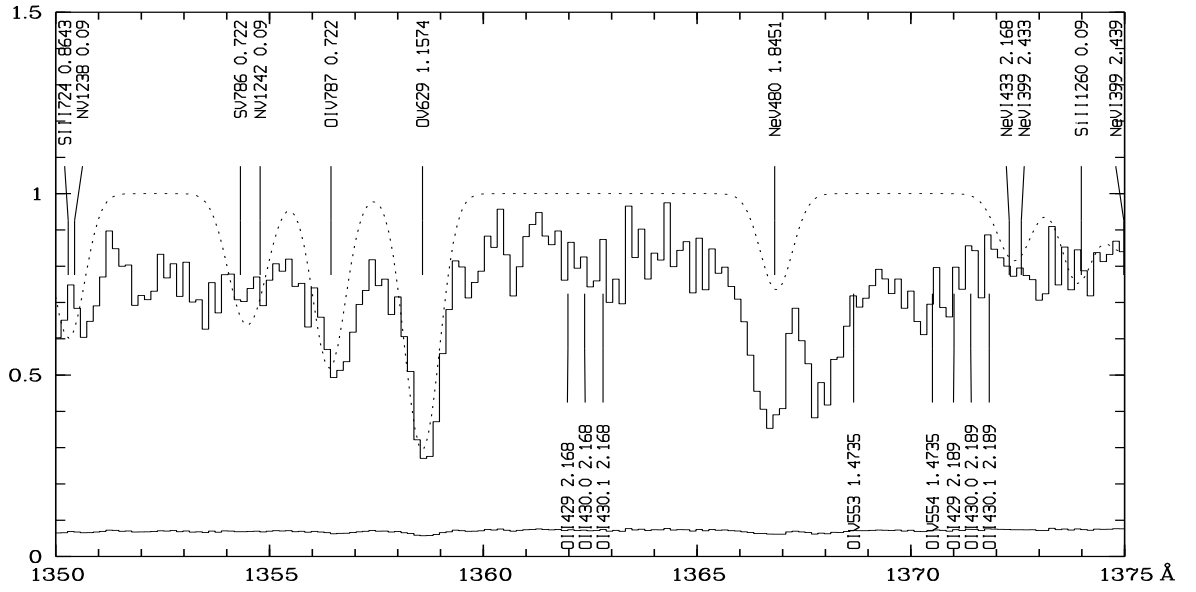
z	ion	b [km/s]	$\log N [cm^{-2}]$	z	ion	b [km/s]	$\log N [cm^{-2}]$
2.315	He I	30	14.8	2.579	Ne VII	50	14.6
	O II	50	14.0		He I	40	14.2
	O III	50	14.6		O III	50	14.3
	O IV	50	15.3		O IV	50	14.75
	O V	50	14.65		O V	50	14.1
	C II	50	14.05		C III	50	14.4
	C III	50	14.4		N III	50	13.9
	N II	50	14.1		Ne III	50	14.5
	N III	50	14.0		Ne IV	50	14.6
	S III	50	13.6		2.7125	He I	30
	S IV	50	13.9	Ne VI		50	14.5
	Ne III	50	14.6	Ne VII		50	14.7
	Ne IV	50	14.8				
	Ne V	50	14.5				
	Ne VI	50	14.4				
2.380	O V	50	13.8				
2.433	He I	38	15.0				
	O III	50	15.05				
	O IV	50	14.55				
	O V	50	14.45				
	C III	50	14.4				
	N III	50	13.7				
	S III	50	13.2				
	Ne III	50	14.4				
	Ne IV	50	14.3				
	Ne VI	50	14.4				
Ne VII	50	14.2					
2.439	He I	25	14.7				
	O III	50	14.6				
	O IV	50	14.85				
	O V	50	14.6				
	C III	50	14.1				
	S IV	50	13.2				
	Ne IV	50	14.5				
	Ne V	50	14.0				
Ne VI	50	14.6					

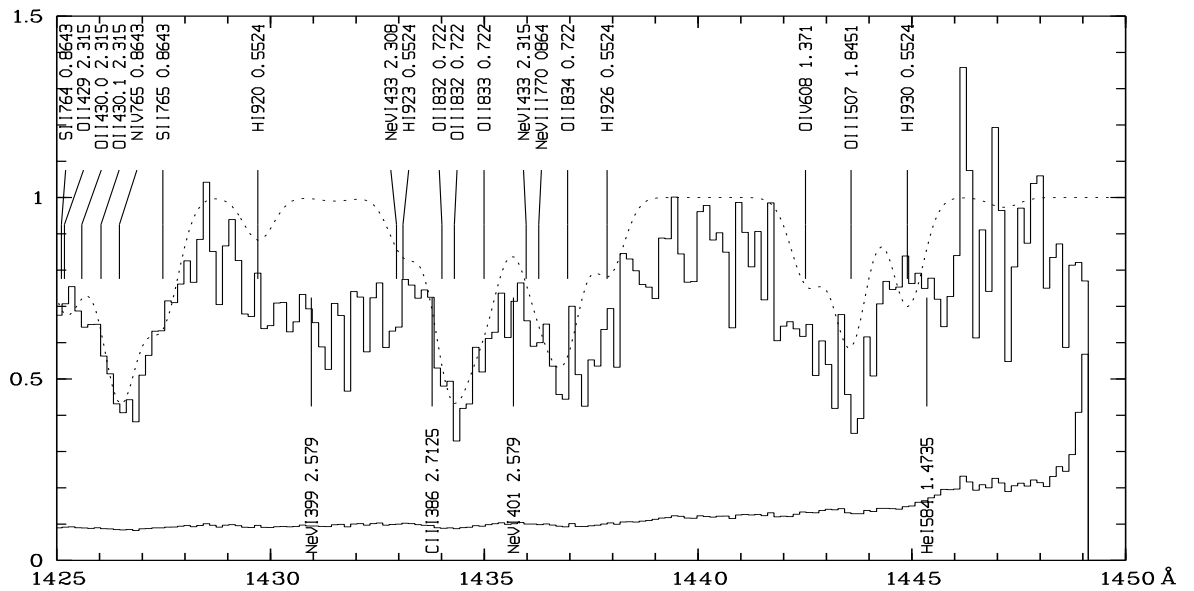
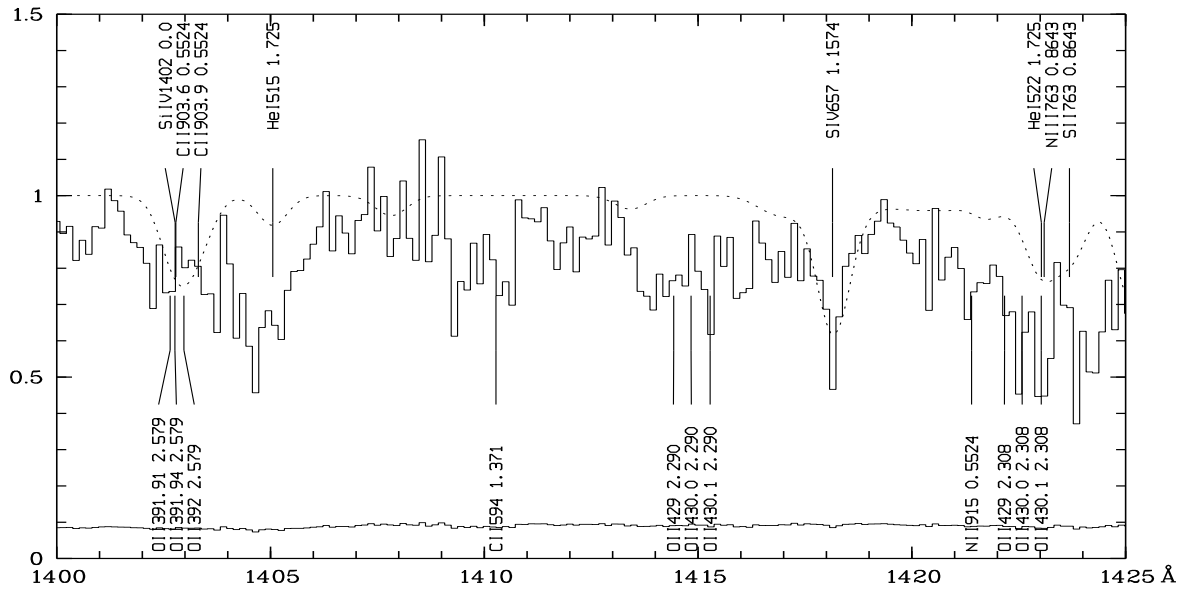


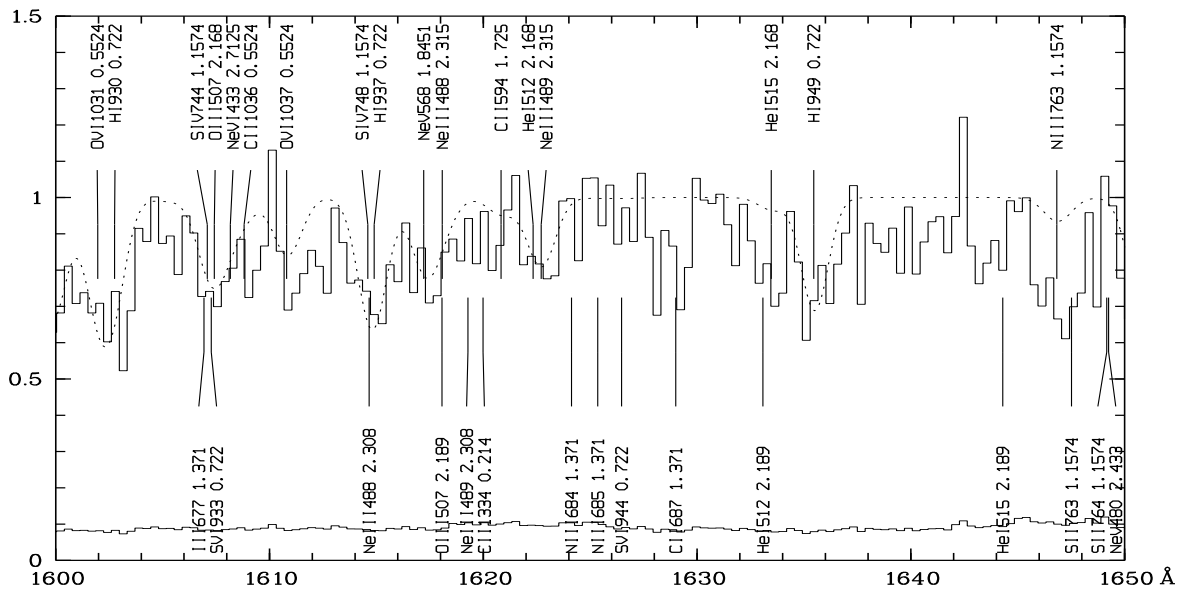
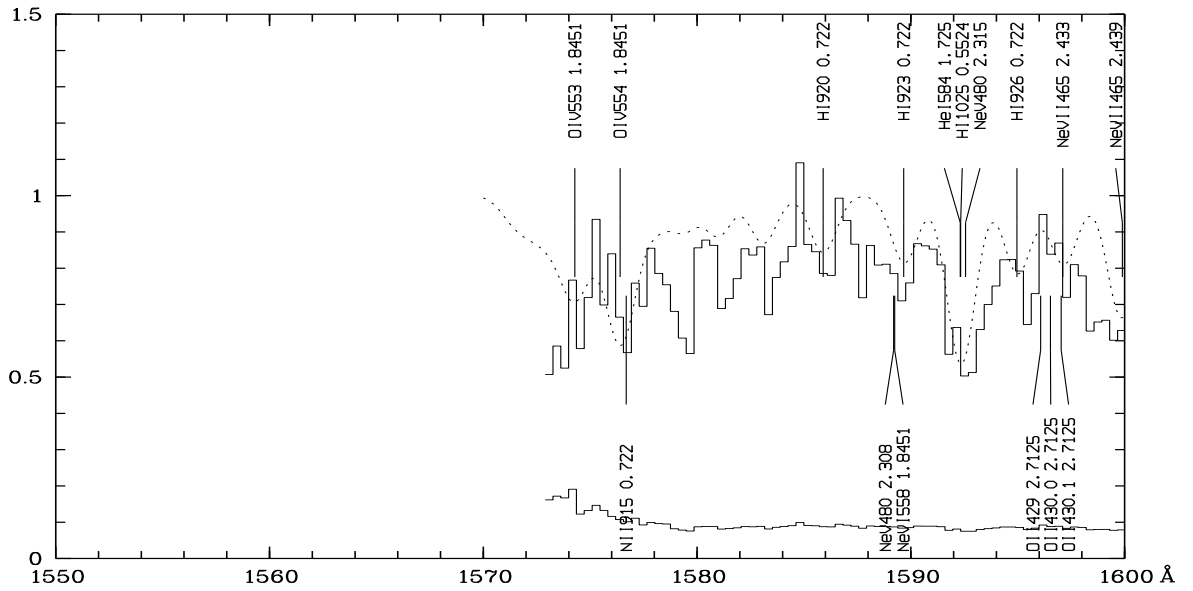


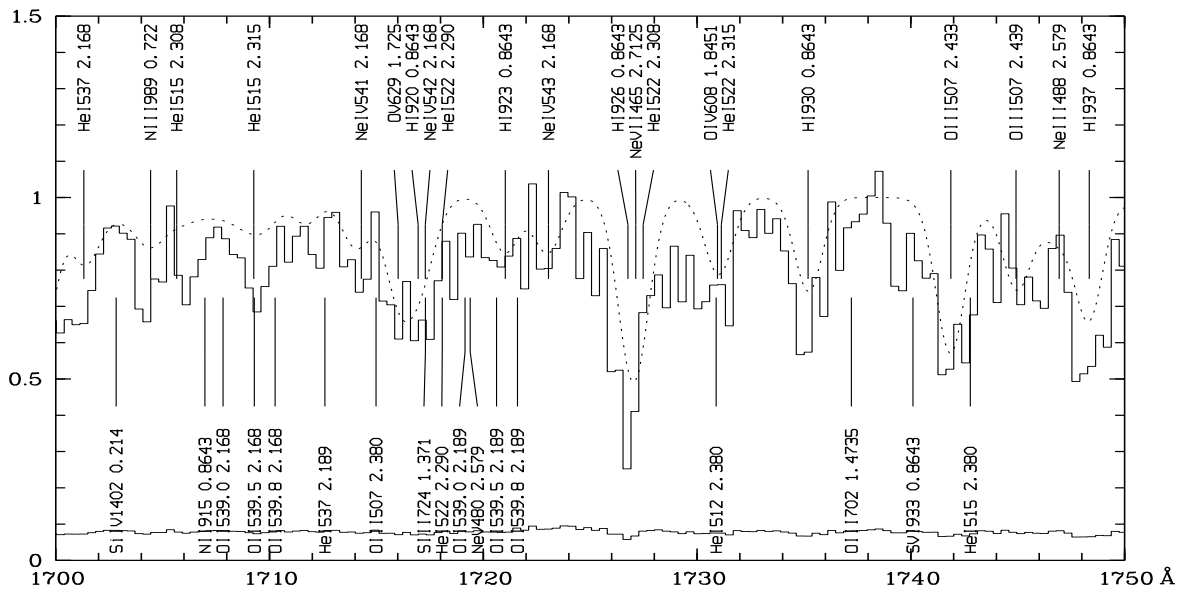
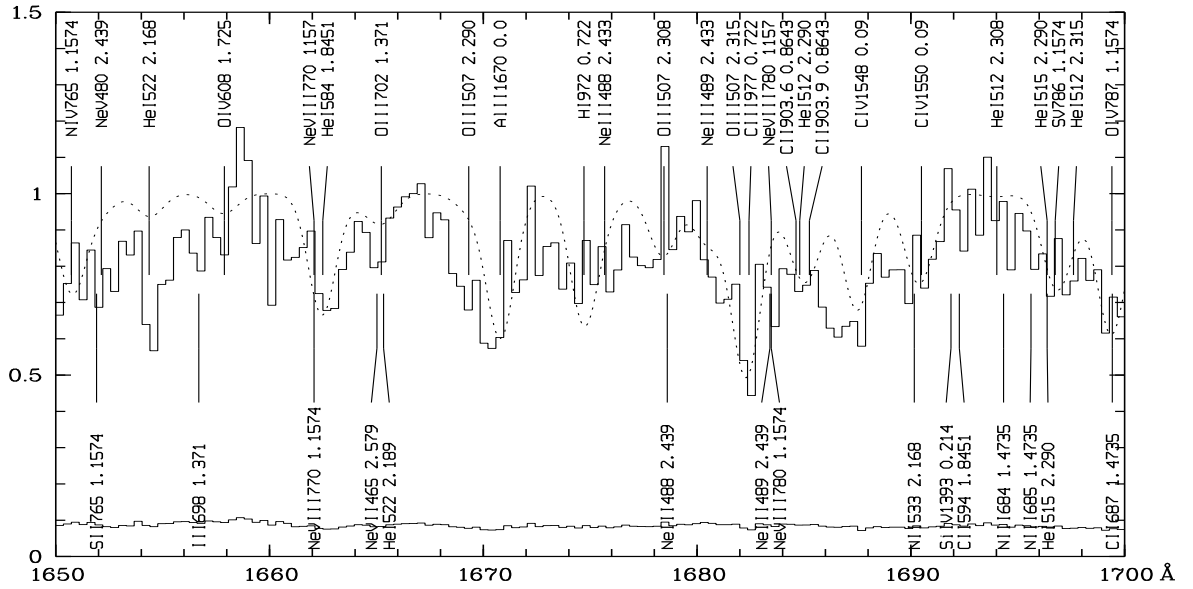


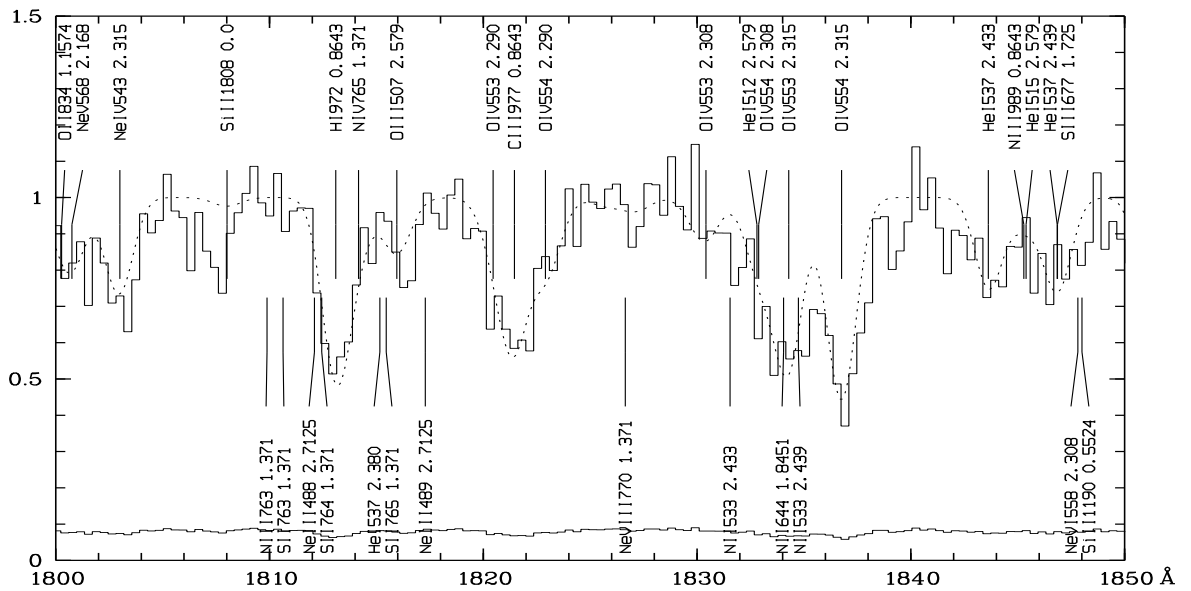
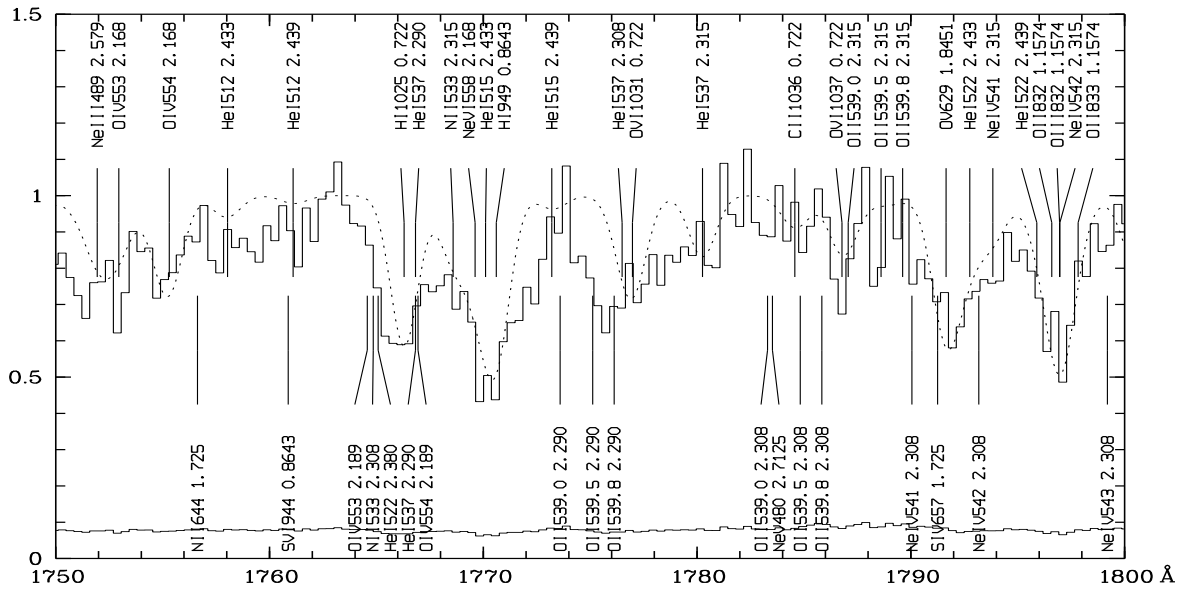


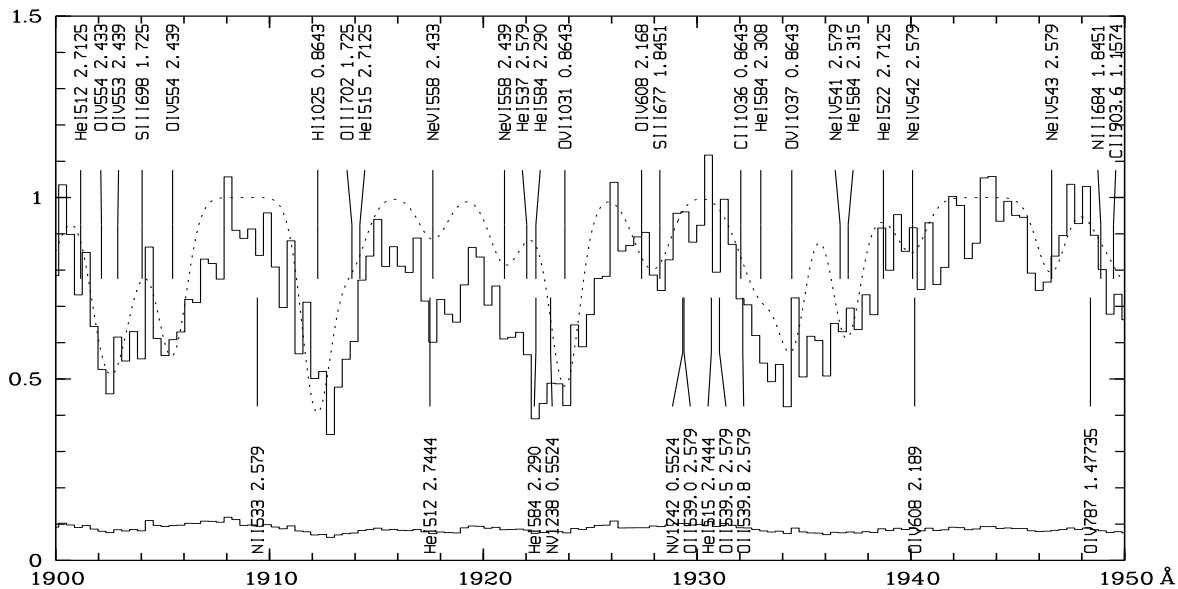
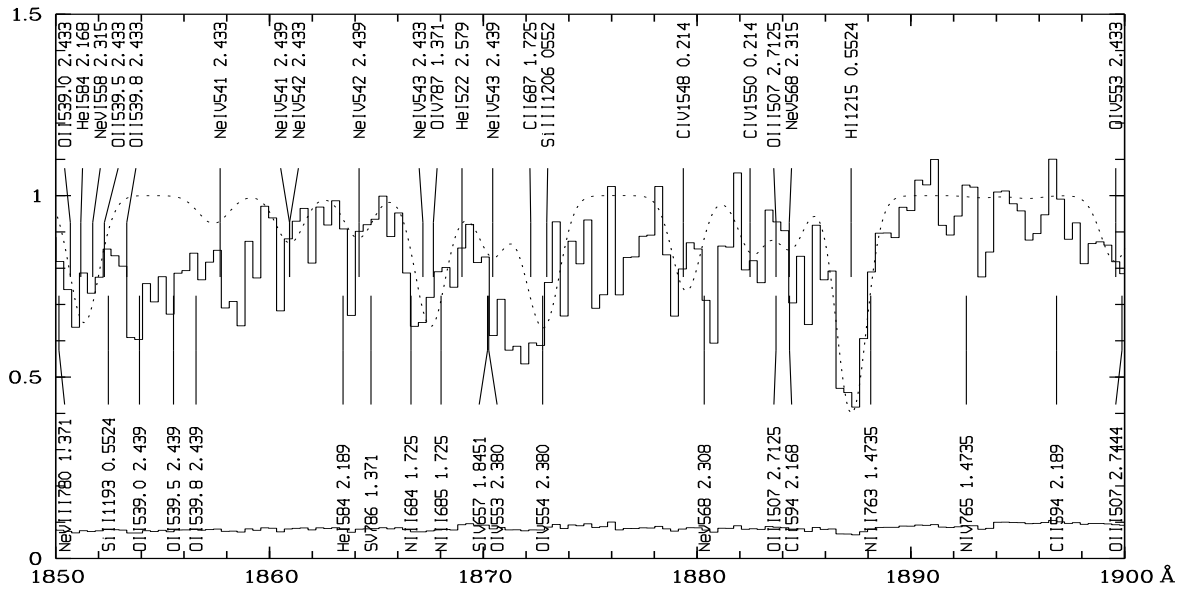


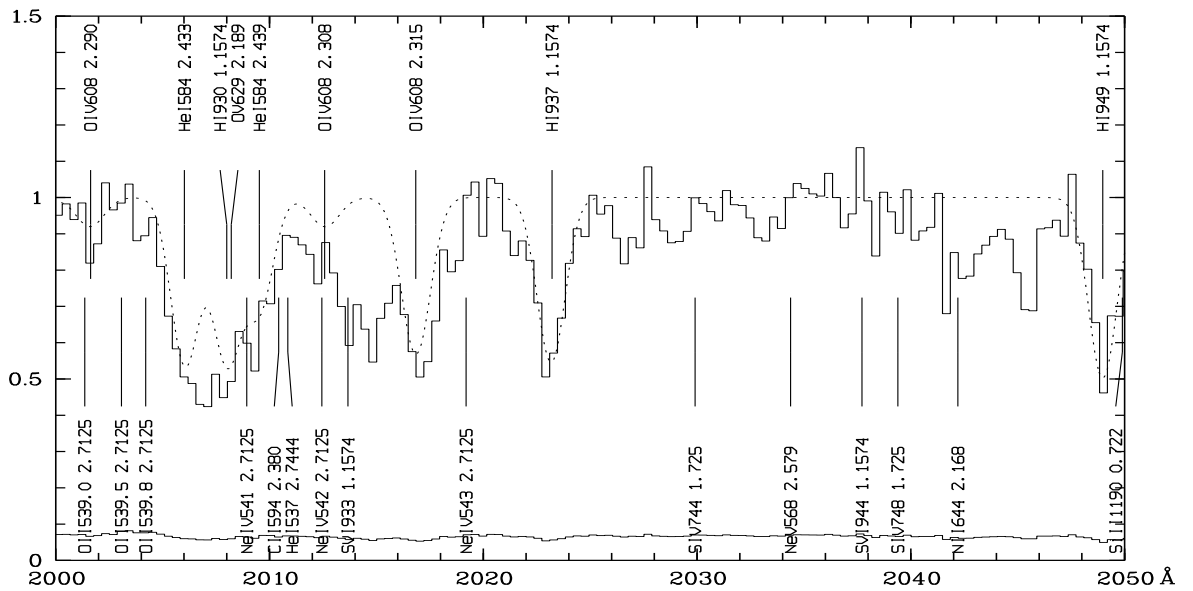
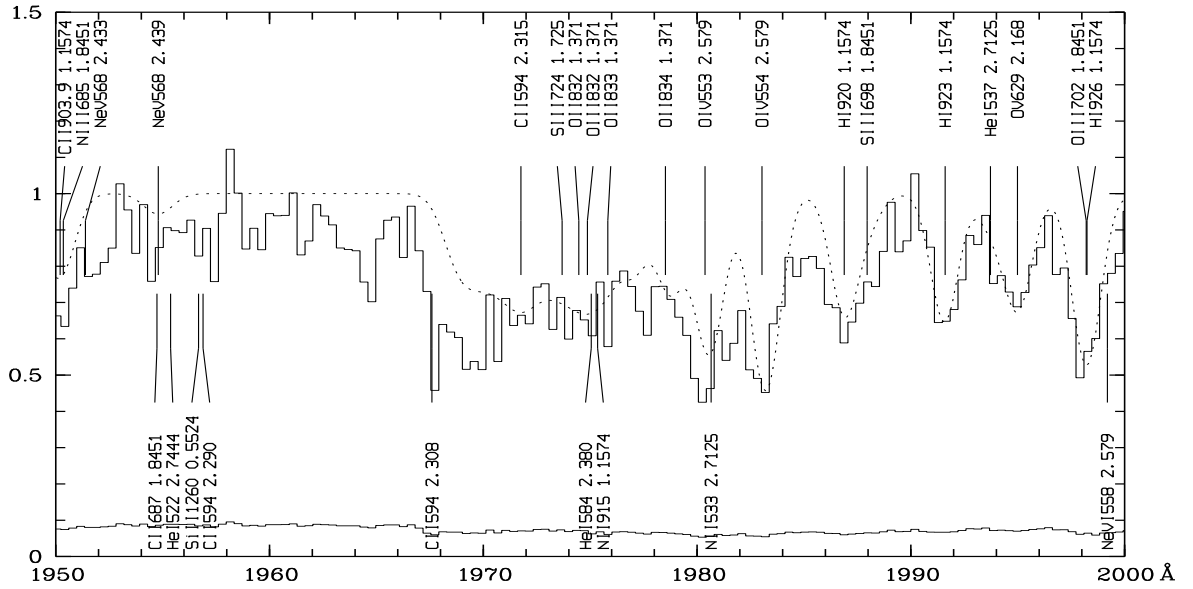


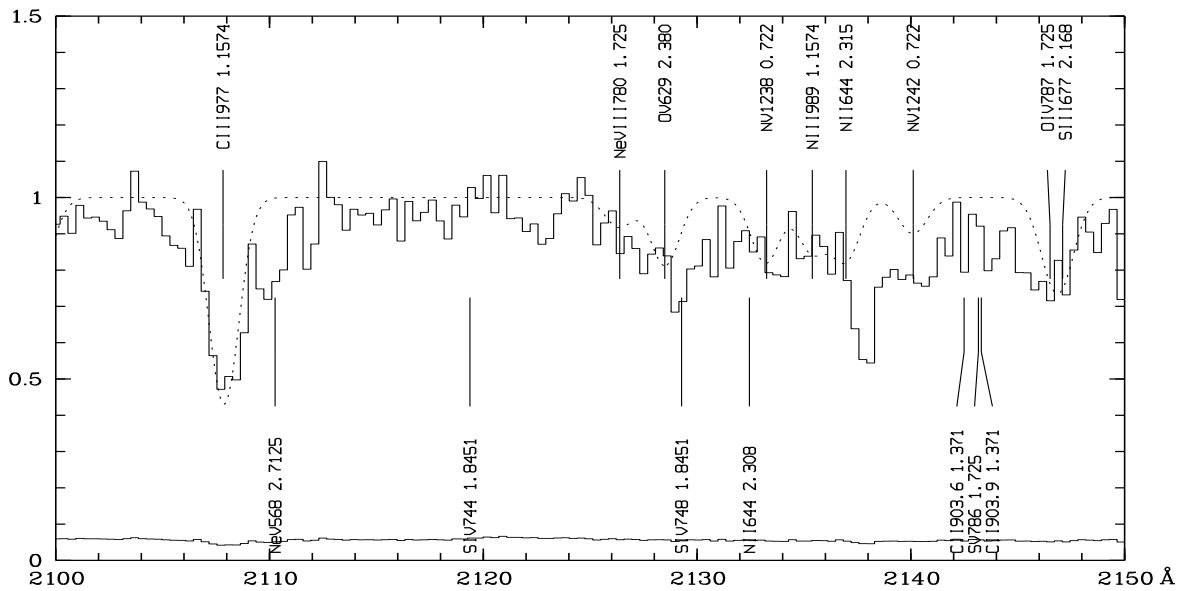
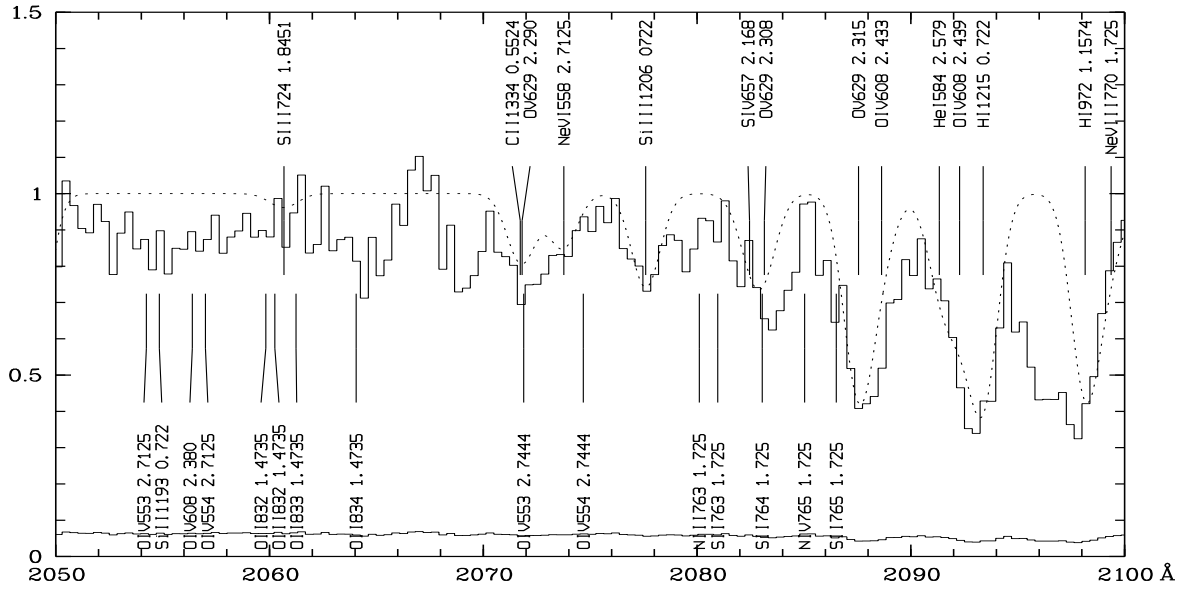


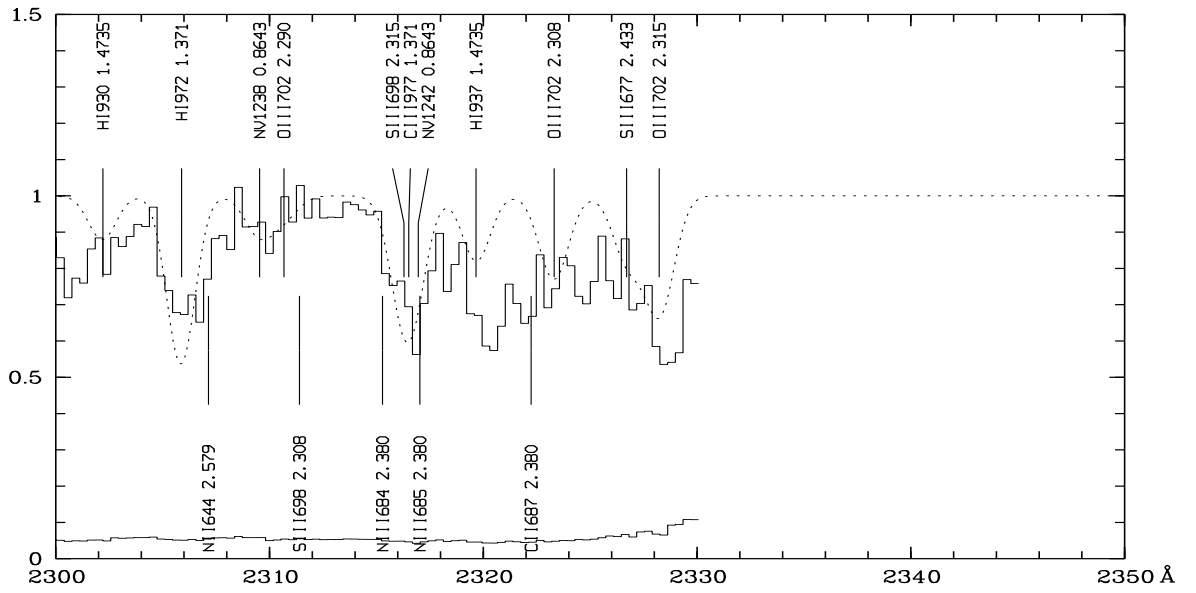
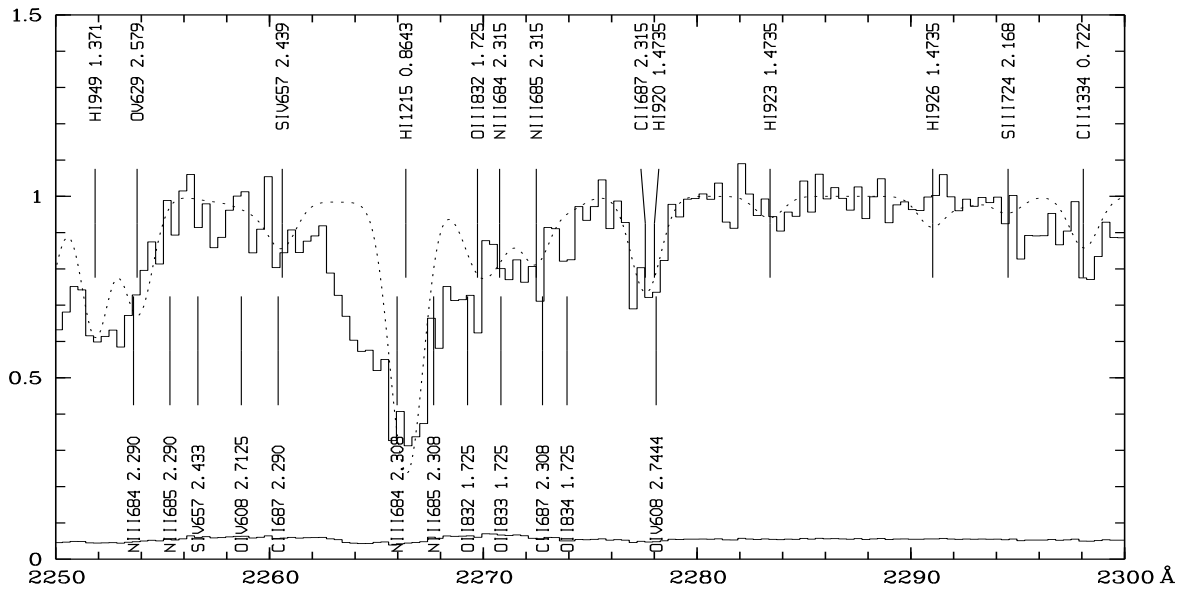












Acknowledgments

I want to express my gratitude to Prof. Dr. Reimers and all other members of the Sternwarte Hamburg Bergedorf for all support in the making of this work. Special thanks goes to the quasar absorption line crew, Susanne Köhler, Sebastian Lopez-Morales and Ana Varga-Villagra, for helpful advice, many fruitful discussions and mental encouragement and to Olaf Wucknitz for patient support concerning the mysteries of Latex.